University of New Mexico
UNM Digital Repository

Earth and Planetary Sciences ETDs

Electronic Theses and Dissertations

Fall 12-13-2018

Insights into Fluid-Rock Interactions on the CV3 Carbonaceous Chondrite Asteroid: The Complex Record in the Allende-like CV3 Chondrite, NWA 2364.

Jessica Marie Johnson
The University of New Mexico

Follow this and additional works at: https://digitalrepository.unm.edu/eps_etds

Part of the Geology Commons

Recommended Citation

Johnson, Jessica Marie. "Insights into Fluid-Rock Interactions on the CV3 Carbonaceous Chondrite Asteroid: The Complex Record in the Allende-like CV3 Chondrite, NWA 2364.." (2018). https://digitalrepository.unm.edu/eps_etds/254

This Thesis is brought to you for free and open access by the Electronic Theses and Dissertations at UNM Digital Repository. It has been accepted for inclusion in Earth and Planetary Sciences ETDs by an authorized administrator of UNM Digital Repository. For more information, please contact amywinter@unm.edu.

Jessica M Johnson

Candidate

Earth and Planetary Sciences

Department

This thesis is approved, and it is acceptable in quality and form for publication:

Approved by the Thesis Committee:

Adrian Brearley , Chairperson

Karen Ziegler

Charles Shearer

Insights into Fluid-Rock Interactions on the CV3 Carbonaceous Chondrite Asteroid: The Complex Record in the Allende-like CV3 Chondrite, NWA 2364.

BY

JESSICA M. JOHNSON

B.S., Geology, Central Connecticut State University, 2016

THESIS

Submitted in Partial Fulfillment of the
Requirements for the Degree of
Master of Science

Earth and Planetary Sciences

The University of New Mexico
Albuquerque, New Mexico

May, 2019

ACKNOWLEDGEMENTS

I am very grateful for the support and encouragement I have received while on this journey to further my education. I would like to thank all of my wonderful friends and family whom were always there to listen and provide humor when needed. I would also like to thank my undergraduate professors who always encouraged us to go to graduate school.

I would like to especially thank my undergraduate role model, aka my science mom, Dr. Kristine Larsen. Had I not met her in 2011, I probably would have never found Geology a place to call home. It is with the deepest gratitude that I thank her for all of her ongoing support and mentorship.

I would like to thank all of the research staff and lab technicians, especially Dr. Mike Spilde for all of his help with obtaining electron microprobe analyses. Thank you Elena Dobrica for answering my ridiculous questions in our office! I would also like to thank Cindy Jaramillo, Faith Mutchnik, Paula Pascetti, and Mabel Chavez in the EPS front office for all of their constant help!!

I would like to thank all of my committee members, Dr. Karen Ziegler and Dr. Charles Shearer, for all of their help, support, and encouragement!

I am immensely grateful for all of the support, guidance, patience, and constant encouragement I have received from my advisor, Dr. Adrian Brearley. I have learned so much in the past two and a half years with his mentorship. He has created such a positive and nurturing learning environment, I was never afraid to fail for I knew it would be met with the positive encouragement to push forward and grow. I have been incredibly fortunate to learn from someone who cares so deeply about the success of his students. For that I am forever grateful.

This study was supported by NASA Cosmochemistry Program through grant NNX15AD28G to Dr. Adrian Brearley (P.I.).

Insights into Fluid-Rock Interactions on the CV3 Carbonaceous Chondrite Asteroid: The Complex Record in the Allende-like CV3 Chondrite, NWA 2364.

By

Jessica M. Johnson

B.S., Geology, Central Connecticut State University, 2016
M.S., Earth and Planetary Sciences, University of New Mexico, 2019

ABSTRACT

The two subgroups of the CV3 chondrites, oxidized and reduced, contain primitive solar system materials that provide many insights into early solar system processes. Both subgroups record significant evidence of secondary alteration that has modified their primary characteristics. In this work, we have studied the petrography, mineralogy, and oxygen isotopic composition of the NWA 2364 $CV3_{OxA}$ chondrite and a large lithic inclusion using SEM, electron microprobe, FIB/TEM, and laser fluorination oxygen isotope analyses in order to characterize their alteration histories in detail. The NWA 2364 host and lithic inclusion consist of chondrules, Calcium-Aluminum-rich Inclusions (CAIs), and fine-grained matrix. In the host, primary minerals in the majority of chondrules have been altered by different types of ferroan olivine. Iron-nickel sulfides are nearly absent from matrix and chondrules. In multiple cases, Ca is absent from chondrule interiors and forms secondary Ca-rich pyroxene aggregates within the matrix. Secondary Na-bearing phases such as nepheline and sodalite are absent. The alteration features found in the lithic inclusion are similar in many ways to the host, but the degree of replacement is more extreme with a few notable differences. In the lithic inclusion, primary minerals have been altered to different types of ferroan olivine and, in some cases, chondrules have been completely pseudomorphed by ferroan olivines. Calcium has been leached from chondrules forming secondary Ca-rich pyroxene aggregates around the peripheries of fine-grained chondrule rims. The lithic inclusion is depleted in the fluid mobile elements, Na, K, and S compared to dark inclusions in Allende. Sodium- and K-bearing secondary phases such as nepheline and sodalite are absent from chondrules and matrix, as are sulfides. Many chondrule olivine phenocrysts contain secondary veins consisting of crystallographically-oriented, elongate, ferroan olivines (a few microns in size), similar in texture to those found in CM chondrites and terrestrial olivine that have undergone serpentinization. Along the exterior of the lithic inclusion there is an abundance of Ca-rich pyroxene aggregates forming a rim along the interface of the host and lithic inclusion. Bulk oxygen isotopic values for the host and lithic inclusion are displaced from the CCAM line, near the compositions of Leoville dark inclusions.

This work provides strong petrographic and geochemical evidence to indicate that the lithic inclusion and the NWA 2364 host were altered by fluid-rock interaction and experienced thermal metamorphism. Based on our observations, we propose the following history for the NWA 2364 chondrite and lithic inclusion. The lithic inclusion underwent aqueous alteration at low temperatures, converting a significant volume of the primary components (matrix, chondrules, etc.) into phyllosilicates and redistributing fluid-mobile elements. Progressive asteroidal heating leading to thermal metamorphism took place, dehydrating the hydrous phases and switching the alteration regime to one of fluid-assisted metamorphism in a lower fluid-rock ratio environment. The fluid released by dehydration was responsible for the fluid-assisted metamorphism, but was ultimately completely lost from the rock. The lithic inclusion was then emplaced in the NWA 2364 host via impact regolith processes. The host was likely still undergoing aqueous alteration at the time of emplacement, causing a geochemical disequilibrium between the two different lithologies. This disequilibrium caused the host and lithic inclusion to interact until the fluids were lost from the rock. Compared to other dark inclusions, the lithic inclusion is highly depleted in fluid mobile elements, suggesting that it has been highly metasomatized by the aqueous fluids. The NWA 2364 lithic inclusion is unique, as it is first lithic inclusion that has definitive evidence of low temperature hydration of primary phases prior to thermal metamorphism, demonstrating that at least some dark inclusions did go through an episode of hydration, not just high temperature interaction with aqueous fluids. This study provides further evidence for parent body alteration, but also adds to our understanding of the dynamic and complex nature of that processes that occurred on the CV3 parent asteroid.

Contents

1 Introduction:

Carbonaceous chondrites belong to an ancient group of primitive meteorites, formed by a variety of processes within the protoplanetary disk during the earliest history of the solar system, 4.567 by ago. These chondrites, unlike the achondrites, did not undergo complete melting of primary materials and thus maintain their primitive materials. In general, the chondrites are made up of several distinct types of components: Calcium- Aluminum-Inclusions (CAIs), chondrules, Fe-Ni metal, and a fine-grained matrix. There are eight main groups of carbonaceous chondrites; CO, CH, CI, CV, CM, CR, CK, and CB. Each of these groups are characterized by their distinct bulk chemical and oxygen isotope compositions (Krot et al., 2014). Because these meteorites contain such primitive material, studies of their unique characteristics can reveal valuable insights to geologic processes that occurred in the early solar system, as well as their potential asteroidal parent bodies.

Broadly, it has been the paradigm that these different carbonaceous chondrite groups represent samples of separate, distinct parent bodies within the asteroid belt (e.g. Anders & Goles, 1961; Anders, 1964; Ringwood, 1963) and this interpretation still persists today. An early, alternative model that has recently received renewed attention was proposed by Wood (1958) who suggested that some groupings of meteorites may have originated from one single, compositionally-zoned common parent body; the achondrites derived from the differentiated interior while an unmelted veneer of this parent body is represented by subgroups of the chondrites. This model was initially rejected, but more recent studies have provided evidence that this model may be viable (e.g. Elkins-Tanton et al., 2011; Weiss & Elkins-Tanton, 2013). New evidence from the

CV3 chondrite group, in particular, has been the main driver for this model in this recent, highly controversial debate, making further studies of these chondrites particularly more crucial.

CV3 chondrites, one of the eight types of carbonaceous chondrites, are a complex group of meteorites that record both nebular and asteroidal processes (Krot et al., 1995). These chondrites can be split into two distinct subgroups; oxidized (CV_{Ox}) and reduced (CV_R) (McSween, 1977). The reduced subgroup contains Fe, Ni metal, whereas in the oxidized subgroup metal has been extensively oxidized to form magnetite and Fe, Ni metal is rare. Both subgroups contain chondrules, calcium-aluminum-rich inclusions (CAIs), Amoeboid Olivine Aggregates (AOAs), a fine-grained matrix, and features called dark inclusions (DI). Within the CV_{Ox} subgroup, two further subdivisions have been recognized; the Allende-like (CV_{OxA}) and the Bali-like (CV_{OxB}), based on distinct alteration features (Brearley, 1997; Krot et al., 1998). Both the oxidized and reduced CV3 chondrites exhibit diverse evidence for aqueous alteration and/or thermal metamorphism giving them a fascinating, but complex history.

An important characteristic of both subgroups of the CV3 chondrites is that they contain distinct, lithic clasts that have been termed ‘dark inclusions’ (DI). They are typically finer-grained and more matrix rich than their host, and hence appear darker in appearance (Kurat et al., 1989; Johnson et al., 1990; Kojima and Tomeoka, 1994; Krot et al., 1995; Buchanan et al., 1997) These inclusions range in size from a few mm to a few cm and contain many of the same components that are typically found in chondrites such as; chondrules, mineral fragments, and CAIs, all set in a fine-grained matrix (Krot et al., 1995; Kojima and Tomeoka, 1996; Krot et al., 1999). While there is a diverse range of characteristics among the dark inclusions among the subgroups of CV3 chondrites, they can generally be divided into four different types that, include; type A, type B, type A/B, and type C (Johnson et al., 1990; Buchanan, 1991). Although each of these four types share similar textural and mineralogical similarities, they are not identical and each type has unique properties. These DIs, like their host chondrites, also show a range of degrees of secondary processing and replacement of primary phases. One notable difference is that the isotopic composition of dark inclusions in the reduced CV3 group lie off the Carbonaceous Chondrite Anhydrous Mineral (CCAM) line with higher $\delta^{18}O$ values in comparison to the oxidized CV chondrite dark inclusions. (Krot et al., 1995; Clayton and Mayeda, 1999; Brearley, 2014).

The degree and style of alteration in the CV3 chondrites is diverse, varying significantly between the reduced and oxidized subgroups. The reduced CV3 chondrites exhibit minimal evidence of alteration via fluid- rock interactions, but have primarily been affected by thermal metamorphism. In contrast, the oxidized CV3 chondrites exhibit more evidence of fluid-rock interactions, but variable degrees of thermal degrees of metamorphism. For example, members of the Bali group are essentially unmetamorphosed, whereas in the Allende group, evidence of variable degrees of metamorphism is apparent (e.g. Grossman, 1980; Brearley and Krot, 2013; Brearley, 2014). The main mineralogical difference between alteration in the reduced and oxidized subgroups is the presence of secondary phases such as ferroan olivine, grossular, wollastonite, andradite, nepheline, sodalite, phyllosilicates, etc. These phases occur commonly within altered CAIs and chondrules in the type oxidized CV3 chondrite, Allende, but are typically rare to absent within the reduced subgroup (Krot et al., 1995).

There is also a distinct difference between the style of alteration that has affected the Allende and Bali subgroups. In the Bali subgroup, the most prominent evidence for fluid-rock interaction is the widespread occurrence of phyllosilicates within the different components of the meteorites. In the Allende subgroup, phyllosilicates do occur, but are extremely rare (Krot et al., 1995). Instead, the secondary alteration phases are dominated by a wide range of anhydrous phases. Chondrules and isolated olivine grains have rim overgrowths consisting of ferroan olivine, chondrule glass has been mostly replaced by nepheline and sodalite, enstatite is replaced by ferroan olivine, and typically CAIs are replaced by phases such as wollastonite, andradite, grossular, and hedenbergite, as well as nepheline and sodalite (e.g. Krot et al., 1995; Brearley and Krot, 2013).

Similar alteration mineral assemblages and textures are also present in the dark inclusions, but the dark inclusions exhibit even more variability in terms of their degree of alteration (e.g. Kojima and Tomeoka, 1994; Krot et al., 1995; Krot et al., 2000; Brearley and Krot, 2013). The textures, mineralogy, and oxygen isotopic compositions of dark inclusions shows the complexity of alteration these chondrites have endured and points to alteration that involved fluid-rock interaction and/or thermal metamorphism that several authors have argued likely occurred post accretion, on the CV3 parent body (Kojima and Tomeoka, 1996; Krot et al., 1999; Krot et al., 2000; Brearley and Krot, 2013; Brearley, 2014).

The complex formation and alteration histories of dark inclusions and their host CV3 chondrites has led to an extensive and ongoing discussion in the literature about their origins and particularly the precise timing and location of this alteration. A number of questions regarding their alteration are still the subject of debate. In the case of dark inclusions, there are six different models for their origin and processing o that can be split into two broad groups; formation and processing in the solar nebula e.g. (Kurat et al., 1989; Palme et al., 1989; Johnson et al., 1990) and origin in the solar nebula with later, post-accretionary alteration on the CV3 asteroidal parent body e.g. (Bunch and Chang, 1983; Kracher et al., 1985; Kojima et al., 1993; Kojima and Tomeoka, 1994). In detail, in early studies such as Kurat et al. (1989), Allende dark inclusions were actually considered to be pristine solar nebular condensate materials that had never experienced any secondary alteration. This scenario was consistent with the view that Allende itself represented pristine materials, all formed directly from the solar nebula. Alternatively, a number of early studies recognized that Allende and its dark inclusions had experienced alteration, but argued that alteration occurred in the solar nebula prior to accretion of asteroidal parent bodies (Grossman, 1972; Allen et al., 1978; McPherson and Grossman, 1984; Palme and Wark, 1988). More recent studies have extensively re-evaluated the oxidized CV chondrites and presented evidence that many of their mineralogical and textural characteristics are the result of secondary alteration processes that occurred on the asteroidal parent body and involved interaction with aqueous fluids. Several studies have also argued that dark inclusions have also experienced similar processes within the CV3 parent body, albeit in a different location (Kojima and Tomeoka, 1993; Kojima and Tomeoka, 1994; Buchanan et al., 1997; Krot et al., 2000; Krot et al., 2004). As a consequence, models that invoke formation and/or alteration in the solar nebula (the “nebular hypotheses”) have become less popular as the “asteroidal parent body hypothesis” has become more widely accepted, e.g. (Housely and Cirlin, 1983; Krot et al., 1995; Kojima and Tomeoka, 1996; Buchanan et al., 1997; Krot et al., 1999; Brearley and Krot, 2013).

There is still much work to be done to better understand the complexities of the CV3 chondrites, their dark inclusions, and the interaction between them. Previous studies of dark inclusions in CV chondrites have demonstrated that there is significant diversity in their characteristics that must reflect considerable variability in the processes that have contributed to their formation. However, these studies have focused on a relatively few CV chondrite falls, principally, Allende, Vigarano, Leoville, and Efremovka. The recovery of numerous new CV3 chondrites from the hot deserts of Northwest Africa has provided additional new samples, which further broaden the spectrum of CV chondrites and their dark inclusions available for study.

Here we contribute to a further understanding of the origin of CV chondrites and their dark inclusions through a study of the mineralogy, petrology, stable isotopic composition, and the bulk elemental composition of the components of the Northwest Africa NWA 2364 $CV3_{OxA}$ chondrite and an unusually large lithic inclusion (LI) that has close affinities to dark inclusions in other CV3 chondrites. These continued studies of dark inclusions are inherently important as they provide new insights into that origin of dark inclusions and the alteration processes that have affected both the host CV chondrite and inclusions themselves. In particular, these observations contribute to further unraveling the role of fluids in the complex geologic history of the CV3 chondrite parent body.

2 Samples and Methods:

Several analytical methods were utilized to study NWA 2364. All mineralogic and petrologic studies were carried out on a sample of NWA 2364 purchased from Blue Sky meteorites that consisted of a significant part of the lithic inclusion (LI), as well as the host chondrite. Petrographic studies were carried out on a 1 inch round polished thin section designated NWA 2364–1 consisting of the host and part of the LI. In addition, a polished block of the LI (NWA 2364-2), mounted in epoxy was also prepared, specifically for Laser Ablation ICP-MS analyses. Both sections are in the sample collection of Dr. Adrian Brearley.

High resolution backscattered electron (BSE) images of the lithic inclusion and the host meteorite were obtained at the University of New Mexico using a FEI Quanta 3D Field Emission Gun SEM operating at 30kV in high vacuum mode with a beam current of 4nA. The SEM studies focused on analyzing the textures and mineralogy of the chondrules, CAIs, AOAs, and matrix material present within the host meteorite and LI. Full thin section BSE and X-ray map mosaics were collected for both NWA 2364-1 and 2. The individual BSE and X-ray maps were stitched together using FIJI imaging processing software. The X-ray maps were obtained at a beam current of 23nA utilizing energy dispersive X-ray spectroscopy (EDS), using an EDAX Genesis EDS system equipped with an Apollo 40 mm^2 silicon drift detector (SDD). Full spectral X-ray maps were collected in all cases. Full spectral, higher magnification EDS maps of individual regions within the LI, along the rim of the LI and NWA 2364 host were also obtained.

Electron microprobe analysis (EPMA) was used to obtain compositional data for minerals in the host NWA 2364 chondrite and the LI. Data were obtained from chondrules, CAIs, and AOAs, and matrix in the host NWA 2364 and the LI. Analyses were obtained using a JEOL 8200 Superprobe electron microprobe using WDS spectrometry at the University of New Mexico. Quantitative analyses were collected for 11 elements (Si, Ti, Al, Cr, Fe, Mn, Mg, Ca, Na, K, and Ni) at operating conditions of 15kV with a 20nA beam current. Elemental calibration was done using the following standards from the Taylor Company Microprobe Standards: #203-Olivine Taylor Std. 3, #204-Albite Taylor Std. 4, #209-Orthoclase Taylor Std. 9, #213-Sphene Taylor Std. 13, #215-Diopside Taylor Std. 15, #217-Chromite Taylor Std. 17, #218-Spessartine Taylor Std. 18, #221-Nickel Taylor Std. 21, #219-Hematite Taylor Std. 19, and #412-Almandine Oxygen Std. 2. Individual spot analyses of phases within larger chondrule phenocrysts and large grains were taken with a beam size of 1µm. Several linear traverses were also taken of similar regions to examine the range in compositional variation using a beam size of 1µm. Elemental calibration was done for the traverses using the same standards as previously, but with the addition of #214-Apatite-F and #230-Pyrite Taylor Std. 30, for P and S. Full ZAF corrections were applied to the data within the Probe for EMPA software.

Broad beam EPMA analyses were collected of mineral phases within the matrix, chondrule phenocrysts, and grains within the thick section that was prepared for LA-ICPMS to provide an internal calibration for the laser analyses. These analyses were taken utilizing a 50µm beam size at 15kV and a beam current of 20nA. To obtain bulk compositions of fine-grained matrix material (including fine-grained rims) a series of data points were collected using the Probe for EPMA software, “shot gun” selection, which provides a set of analytical points randomized location of set points. Quantitative analyses were collected for 13 individual elements; Si, Ti, Al, Cr, Fe, Mn, Mg, Ca, Na, K, Ni, S, and P. Elemental calibration was done using the same standards as previously.

Bulk oxygen isotope analyses were obtained from samples of the host meteorite and the lithic inclusion using the laser fluorination oxygen isotope analysis technique (Sharp, 1990) in the Center for Stable Isotopes at UNM. Nine fragments of material were removed carefully from 200-500 micron thick slices of the sample using stainless steel dental tools. This approach enabled identification of specific regions of the sample to be selected for analysis. These 9 samples consisted of two samples from the host meteorite, four samples from the boundary/rim material between host and LI, and three from the lithic inclusion (LI) itself. Due to the limited mass of some of the sample fragments, some of the fragments were combined and analyzed as four separate samples; the two host samples, one LI sample (2 fragments) and one (combination of 4 fragments) boundary/rim sample (see Table 20 for sample names, weights, and their $\delta^{17}O$ and $\delta^{18}O$ values). Prior to the analysis, each sample was cleaned with 6M HCL and set on a hot plate for approximately 10 minutes. The acid was drained, the samples were rinsed with distilled water and the process was repeated a second time to ensure the removal of any contamination. The samples were then dried in an oven for approximately 10 minutes. Once dried they were weighed individually and placed into the sample holder along with 10 individually weighed San Carlos olivine standards. The samples were laser flourinated and run through the laser fluorination system and then the purified gas was analyzed over a cycle of 20 standard-sample comparisons with a Finnegan MAT 253 Dual-Inlet Isotope Ratio Mass Spectrometer. The results were linearized and converted to per mil V-SMOW.

Transmission electron microscope (TEM) data were collected to characterize the chemical composition, microstructures, morphologies, and relationships to other phases from a Ca-pyroxene bearing aggregate in the matrix of the lithic inclusion. A FIB section was extracted from one representative Ca-pyroxene-bearing aggregate using a FEI Quanta 3D Dualbeam® FEGSEM/FIB instrument at UNM. Prior to extraction of the FIB section a protective layer of platinum 2 µm wide and 2 µm thick was deposited onto the region of interest in order to prevent ion beam damage during preparation. The FIB section was removed from the thin section using an Omniprobe 200 micromanipulator and mounted onto a copper TEM half grid. The sample was then thinned down to electron transparency using an ion gun accelerating voltage of 30 kV and beam currents of 1 nA decreasing to 50 pA for the final stage of ion thinning. The FIB section was then analyzed using a JEOL 2010F FASTEM Field Emission Gun Scanning Transmission Electron Microscope (FEG/STEM) operating at 200kV. Bright-field TEM and high-angle Annular dark field (HAADF) images were taken of the section as well as high resolution bright field images. Full spectral energy dispersive X-ray spectroscopy (EDS) maps of the sample were obtained in STEM mode on the JEOL 2010F using an Oxford Instruments AZtec EDS system equipped with an Oxford X-MaxN 80T SDD EDS detector (80 mm^2 sensor). Quantitative analyses of individual phases were obtain by processing regions of interest from the X-ray maps using the Cliff-Lorimer thin film approximation using theoretical k-factors.

3 Results

3.1. Petrographic Observations

3.1.1. Hand Sample of NWA 2364: General Characteristics

NWA 2364 is a CV3 chondrite that was recovered in an unidentified region of Northwest Africa in 2004 (Russell et al., 2005). As reported in the Meteoritical Bulletin, there was a large mass of material recovered in eighteen individual fragments. The shock stage was classified as S2 and weathering as W4. NWA 2364 is an Allende-like CV3 oxidized chondrite (Russell et al., 2005). Figure 1 shows a slab of NWA 2364 in hand sample. It is approximately (1.8cm) and light tan in color with reddish-brown staining around some of the chondrules and the edges. In the figure, the larger features such as chondrules, CAIs, AOAs, are all set in a fine-grained matrix that is the tan, reddish-brown matrix material. The more notable feature is the large lithic inclusion (LI), approximately 1.8cm long and 1cm wide, as indicated from the largest piece seen in Figure 1. The LI has a few larger chondrules that can easily be seen macroscopically along with many smaller chondrules and fragmented pieces of larger grains. These materials are set in a very fine-grained matrix material that is not dark in color unlike typical dark inclusions found, in for example, the oxidized CV3 chondrite, Allende. Overall, compared to the host meteorite, the LI is finer-grained and also appears to have less reddish-brown staining. As indicated in Figure 1, a very fine-grained, darker rim surrounds the LI and host and has a variable thickness (0.1-0.5cm). Macroscopically, there are no observable veins of Fe-oxy-hydroxide or Ca carbonate veins present within the meteorite despite the reddish brown color typical of desert meteorites.

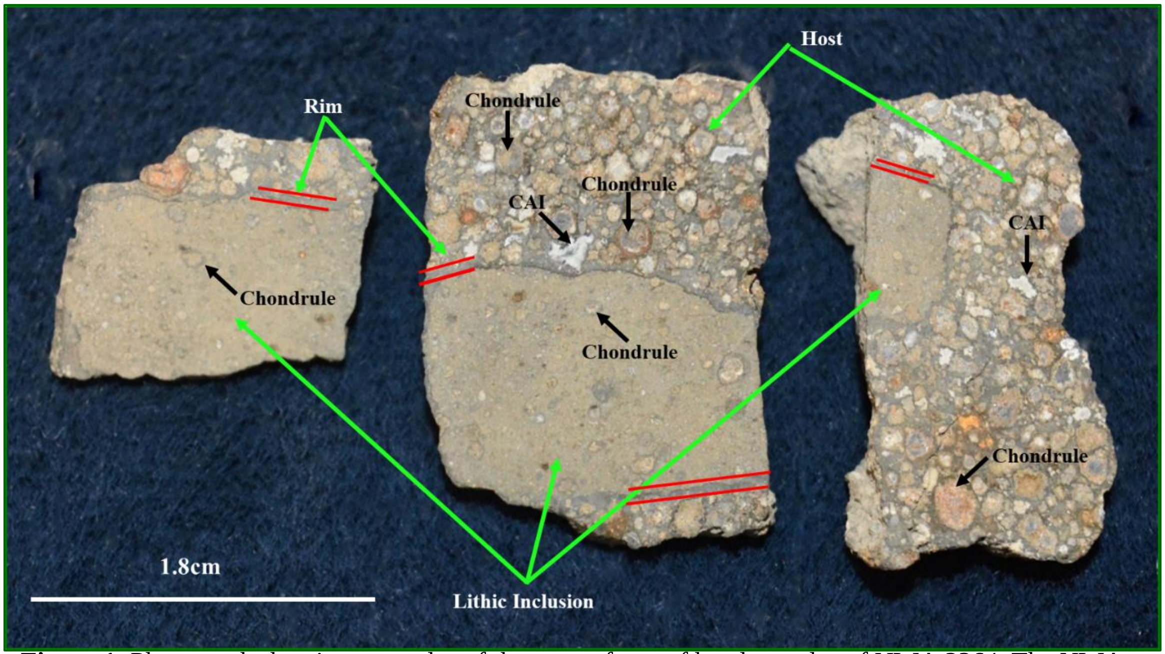

Figure 1: Photograph showing examples of the cut surfaces of hand samples of NWA 2364. The NWA 2364 host, the lithic inclusion and its fine-grained rim are indicated with green arrows. Small sections of the rim are outlined with red lines to indicate more prominently where it occurs on each of three samples. The rim is not present along the entire periphery of all three pieces of the lithic inclusion. There are small amounts of reddish-brown staining, indicative of desert weathering, around a few chondrules and the edges of the hand sample. This staining much less evident within the lithic inclusion (LI). Chondrules and CAIs are indicated with black arrows. No observable Fe-oxyhydroxide or Ca carbonate veins are apparent in any of the three samples.

3.1.2. *Host*

In general, NWA 2364 has the typical characteristics of a CV3 oxidized chondrite. Figure 2 shows a BSE composite image of a thin section of NWA 2364 and the LI. The NWA 2364 host chondrite consists of mm-sized chondrules, AOAs, and CAIs set within a fine-grained matrix. Figure 3 shows a full thin section X-ray map (Mg(R)Fe(G)Ca(B)) that shows the distribution of Mg-rich olivine and pyroxene-bearing chondrules (red) and Ca-rich CAIs very clearly. The distinct texture of the LI in the upper left central part of the section is apparent with much fewer chondrules and finer grained. As in the macroscopic view, no Fe-oxyhydroxide or Ca carbonate veins due to weathering are present within the section. The Ca-rich rim around the LI is due to the presence of Ca-rich pyroxene layer, discussed in detail later. Both type IA and IIA chondrules are present, however the type IIA chondrules are in lesser abundance; of the 46 chondrules counted in the host meteorite, only 2 are type IIA. The BSE and X-ray maps show that the abundance of metallic Fe, Ni is extremely low. Nickel X-ray maps

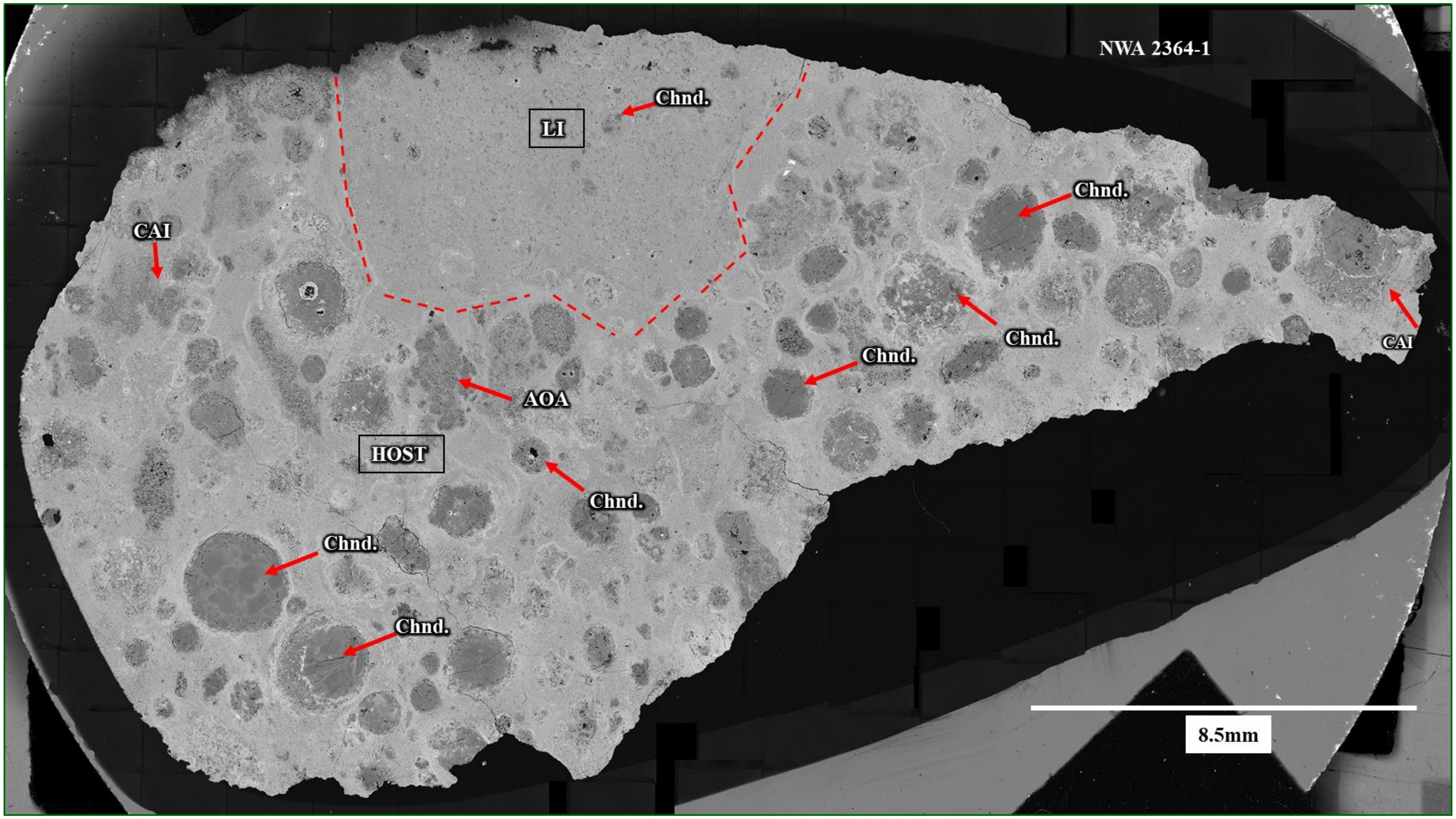

Figure 2: Backscattered electron mosaic image of the entire thin section of NWA 2364-1 and its lithic inclusion (LI). The LI and host regions of the NWA 2364 chondrite are indicated on the figure. The LI is outlined by a dashed red lines. Chondrules, CAIs, and AOAs are present in the section and indicated by red arrows. These coarser-grained components are embedded within a Fe-rich, fine-grained matrix material that constitutes the most abundant material in the sample.

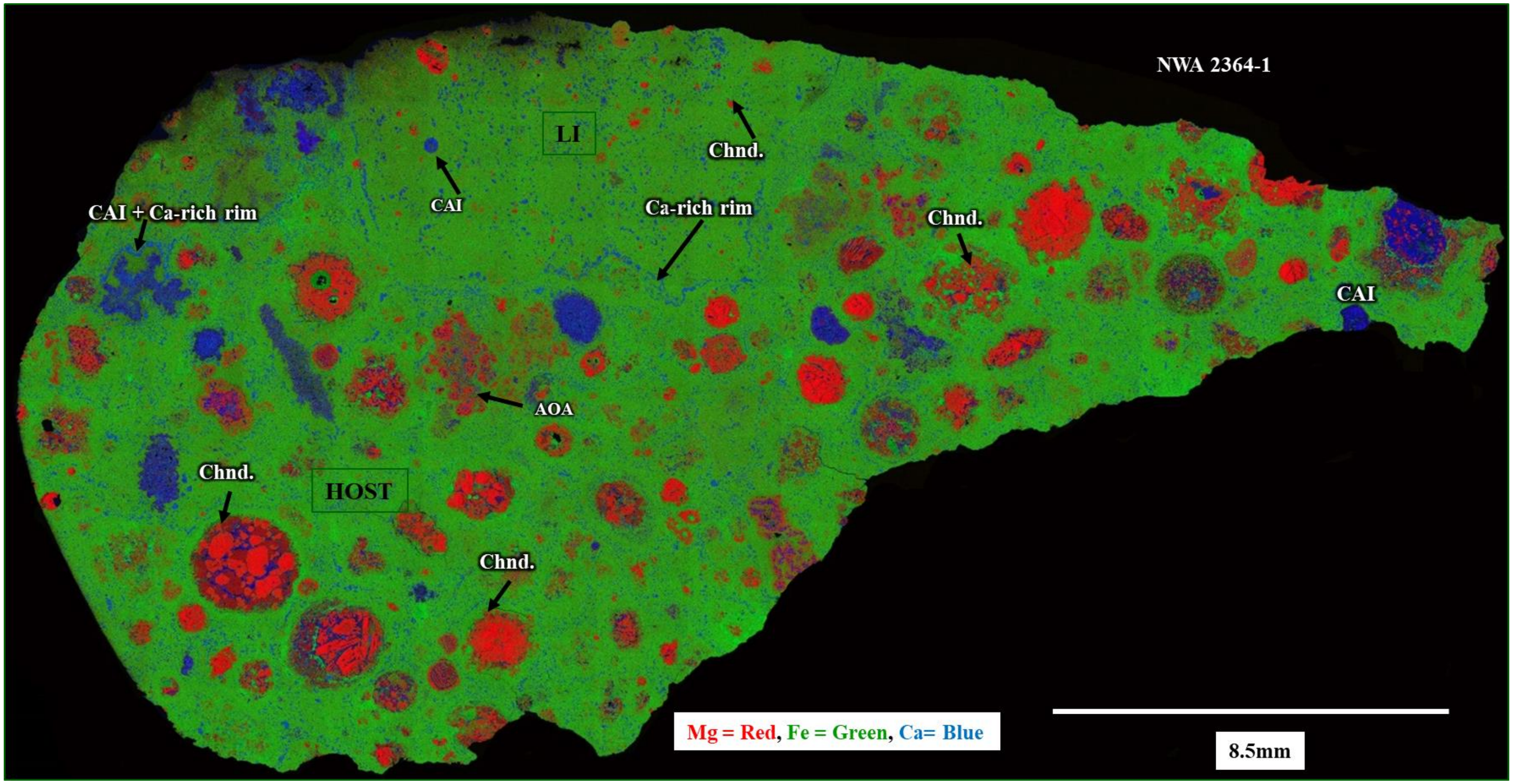

Figure 3: Full thin section composite Mg(R)Fe(G)Ca(B) X-ray map of the entire thin section of NWA 2364-1 showing the distinct textural and compositional differences between the host and the LI. The LI is finer grained than the host meteorite and has a high abundance of matrix material. Chondrules are rare and much smaller than in the host. Around the perimeter of the LI there is a thin discontinuous layer Ca phases abundant in Ca-rich pyroxene (indicated by the black arrow).

show that <0.1 volume % of Ni-bearing metal is present in the host compared with an average 1.9 vol% in CV chondrites (McSween, 1977). A sulfur X-ray map shows that the sulfide abundance is also low, approximately 0.2 vol% within the host meteorite compared with an average 2.2 vol% in CV chondrites (McSween, 1977). The sulfides are primarily in the chondrules, with only trace amounts in the matrix. As documented, below, chondrules, CAIs, and matrix in the host chondrite all show numerous features that are indicative of alteration and metamorphism.

3.1.2.i. Host CAIs

In the host there at least 9 CAIs were identified, some examples indicated in Figure 3. The CAIs vary in size from ~150 µm up to ~1mm in their maximum dimension. Two examples of fluffy, spinel-rich CAIs, the smallest CAIs identified within the host, are shown in Figure 4. A composite RGB Al-Ca-Ti X-ray map shown in Figure 4b and demonstrates that the CAI has a layered structure consisting of a spinel-rich core containing fine-grained inclusions of perovskite, surrounded by a rim of diopside. Aside from the CAI there is a large percentage of Ca-rich pyroxene aggregates surrounding the CAI as seen with the chondrules. This is also observed in Figure 3 for some of the other CAIs that can be seen in the upper left region of Figure 3. Limited data has been obtained for these CAIs and their alteration thus more work needs to be completed in the future in order to characterize these features in more detail.

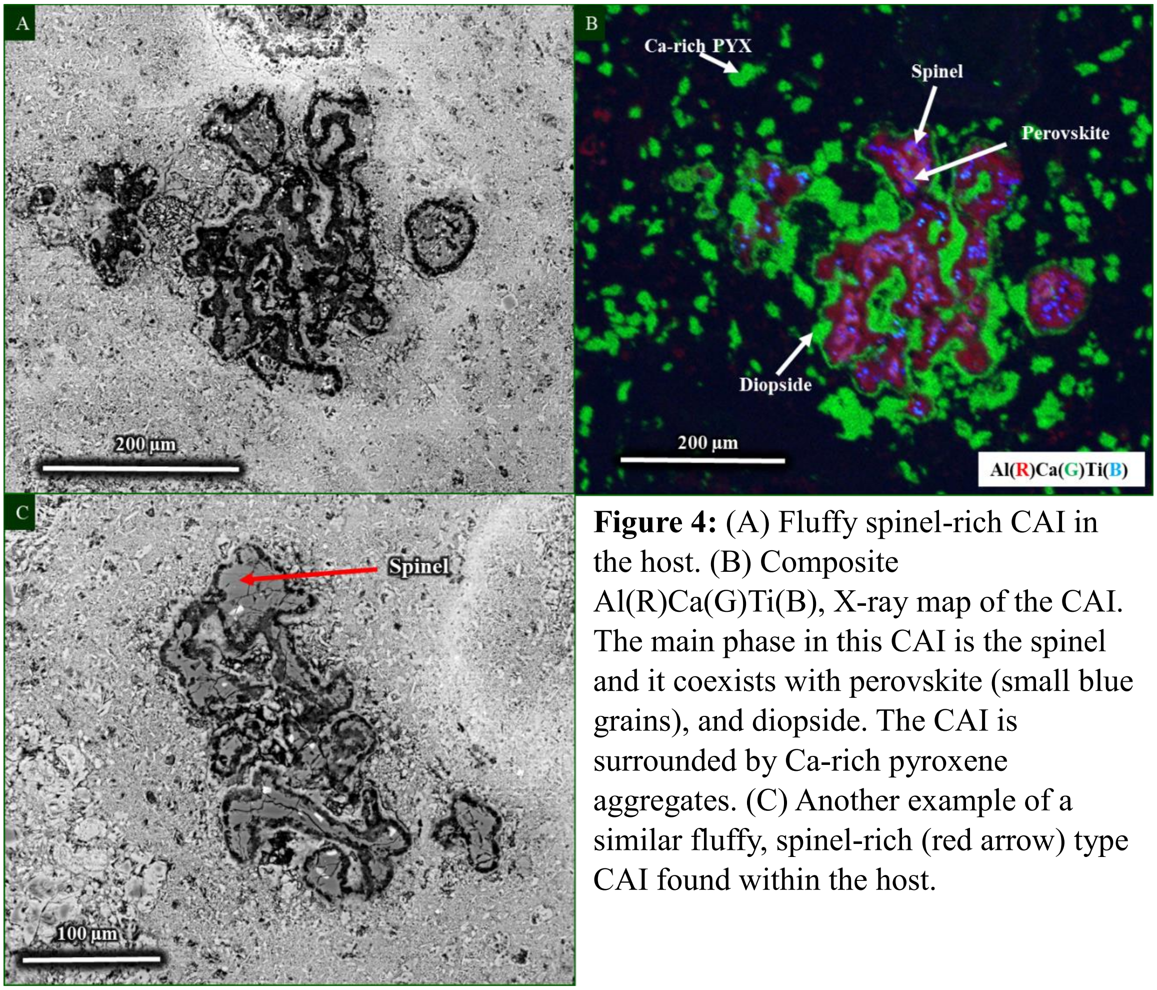

Figure 4: (A) Fluffy spinel-rich CAI in the host. (B) Composite Al(R)Ca(G)Ti(B), X-ray map of the CAI. The main phase in this CAI is the spinel and it coexists with perovskite (small blue grains), and diopside. The CAI is surrounded by Ca-rich pyroxene aggregates. (C) Another example of a similar fluffy, spinel-rich (red arrow) type CAI found within the host.

3.1.2.ii. Host Chondrules

The chondrules in the host meteorite are on average a few hundred microns in diameter, some are as large as 1 mm. Within the host meteorite several different textural types of chondrules were identified; macroporphyritic type IA, porphyritic type IA, porphyritic type IAB, barred type IA, and porphyritic type IIA. Figure 5 shows representative BSE images of the different textural types of chondrules. The chondrules within the host meteorite exhibit a number of different features indicative of alteration (Figs. 5 and 6). Enstatite phenocrysts have been replaced to varying degrees by platy, ferroan olivines, as well as more massive, anhedral grains of ferroan olivine. This alteration, as seen in Figure 5c & 6, is more extreme around the outer regions of the chondrule and diminishes into the chondrule interior. Chondrule glass in the majority of the chondrules has been replaced by secondary phases, mainly ferroan olivine (Figure 5d), but there are a few examples of chondrules, of different textural types, that retain primary, unaltered chondrule glass (Figure 5b-c & 7). Forsteritic olivine phenocrysts in type IA, type IAB, and barred type IA chondrules have ferroan overgrowths around the edges of the phenocrysts (Figures 5a, b, c, d). These ferroan overgrowths are heterogeneous in width and occurrence from chondrule to chondrule, as well as within the same chondrule. They range in width from a few microns up to around 20 microns. They are typically porous and in some cases have micron-sized chromite grains within them.

In type IA Mg-rich chondrules, forsteritic olivine phenocrysts show an enrichment in Fe along their edges and along fractures, a characteristic typical of Fe-Mg diffusion along grain boundaries (Figures 5d & 6). Most metal nodules present in the chondrules have mostly or entirely been replaced ferroan olivine, but in some cases a rare Fe-Ni sulfide. The limited number (<1 vol%) of metal nodules that do remain are located closer to the interior of the chondrule olivine phenocrysts where they were protected from alteration. In some chondrules, the metal nodules have been extensively altered and pseudomorphed by platy, ferroan olivines. These pseudomorphs are recognizable because of their rounded to subrounded shapes that are typical of metal grains in unaltered chondrules in ordinary and carbonaceous chondrites (Figure 5c & 5d). Some chondrules are surrounded by fine-grained rims ranging in thickness from tens of microns to about 100μm. The fine-grained rims are composed of fine-grained platy olivines that are densely packed and only a few microns in size (Figure 5b).

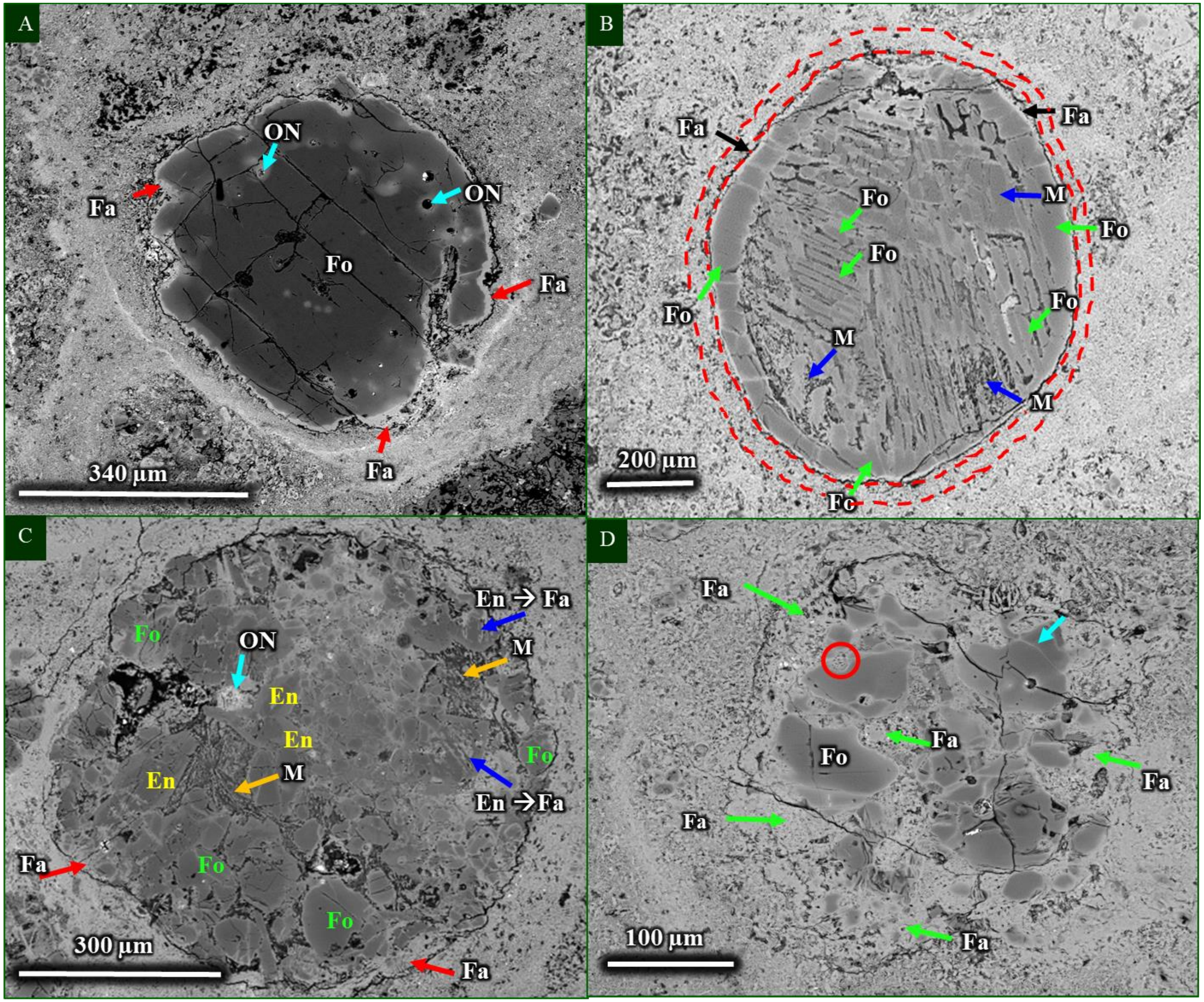
A
ON
ON
Fa
Fo
Fa
Fa
340 µm
B
Fa
Fa
M
Fo
Fo
Fo
Fo
Fo
M
M
200 µm
Fo
C
En → Fa
Fo
ON
M
En
En
Fo
En
M
En → Fa
Fa
Fo
Fo
300 µm
Fa
D
Fa
Fa
Fo
Fa
Fa
100 µm
Fa

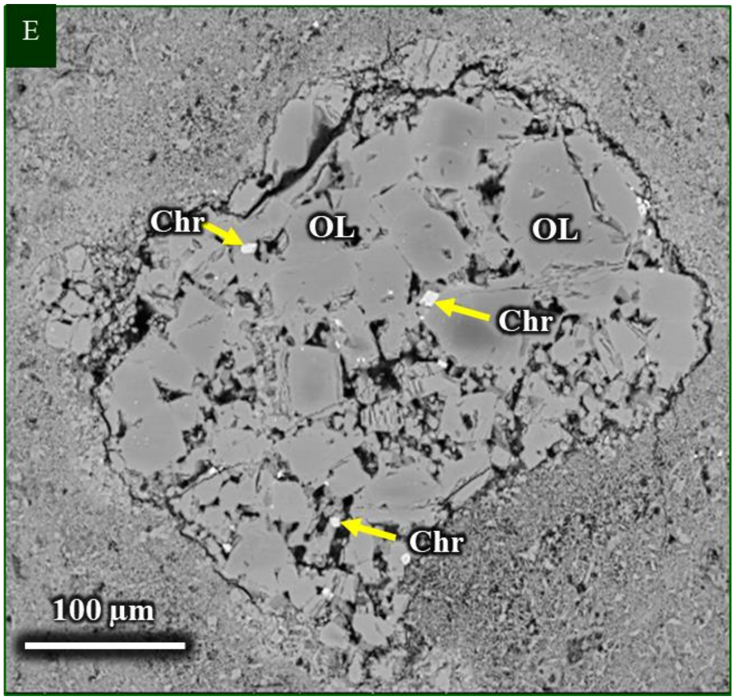

Figure 5a-e: Backscattered electron images showing representative examples of chondrules in the NWA 2364 host CV3 chondrites. (A) BSE image of macroporphyritic type IA chondrule in the host. This host chondrule exhibits several alteration features. Around the edges of the chondrule ferroan olivine overgrowths (Fa, indicated by red arrows) are observed. Iron-rich haloes are present within forsterite grains around the location where metal nodules where present (labeled "ON" and indicated by the blue arrows. (B) BSE image of a barred type IA chondrule in the host. The barred olivine phenocrysts and the olivine around the outside of the chondrule are labeled "Fo" and indicated by the green arrows. This chondrule has some regions of mesostasis material (labeled "M"; indicated by blue arrows) that are partially altered. A fine-grained chondrule rim is indicated by red dashed lines. Larger olivine phenocrysts have ferroan olivine (Fa) overgrowths indicated by the black arrows. (C) BSE image of a porphyritic type IAB chondrule in the host containing olivine (Fo) and low-Ca pyroxene phenocrysts (En). Regions of unaltered mesostasis (M) are also present (orange arrows). The low-Ca pyroxene is being altered to ferroan olivine (blue arrows and labeled "En→ Fa"). Ferroan olivine has replaced most of the mesostasis material, ferroan overgrowths (Fa, red arrows) have formed along the edges of the chondrule and the metal nodule (ON, light blue arrow) has been replaced by ferroan olivine. (D) BSE image of a smaller porphyritic type IA chondrule in the host, containing primary forsteritic olivine phenocrysts (Fo) that have developed extensive ferroan olivine overgrowths (Fa, indicated by the green arrows). These extend well into the interior of the chondrule as well as around the edges of the phenocrysts. Any metal nodules have been replaced by ferroan olivine (circled in red), and there is Fe-enrichment along the cracks within the chondrule olivine phenocrysts (indicated by the light blue arrow). (E) BSE image of porphyritic type IIA chondrule in the host. Some chondrule olivine (OL) phenocrysts show Mg-Fe zoning typical of olivine in type IIA chondrules. These chondrules typically have many micron-sized chromite (Chr) grains indicated by yellow arrows) either within phenocrysts or along the edges of phenocrysts "Chr". Chr = chromite; OL = olivine.

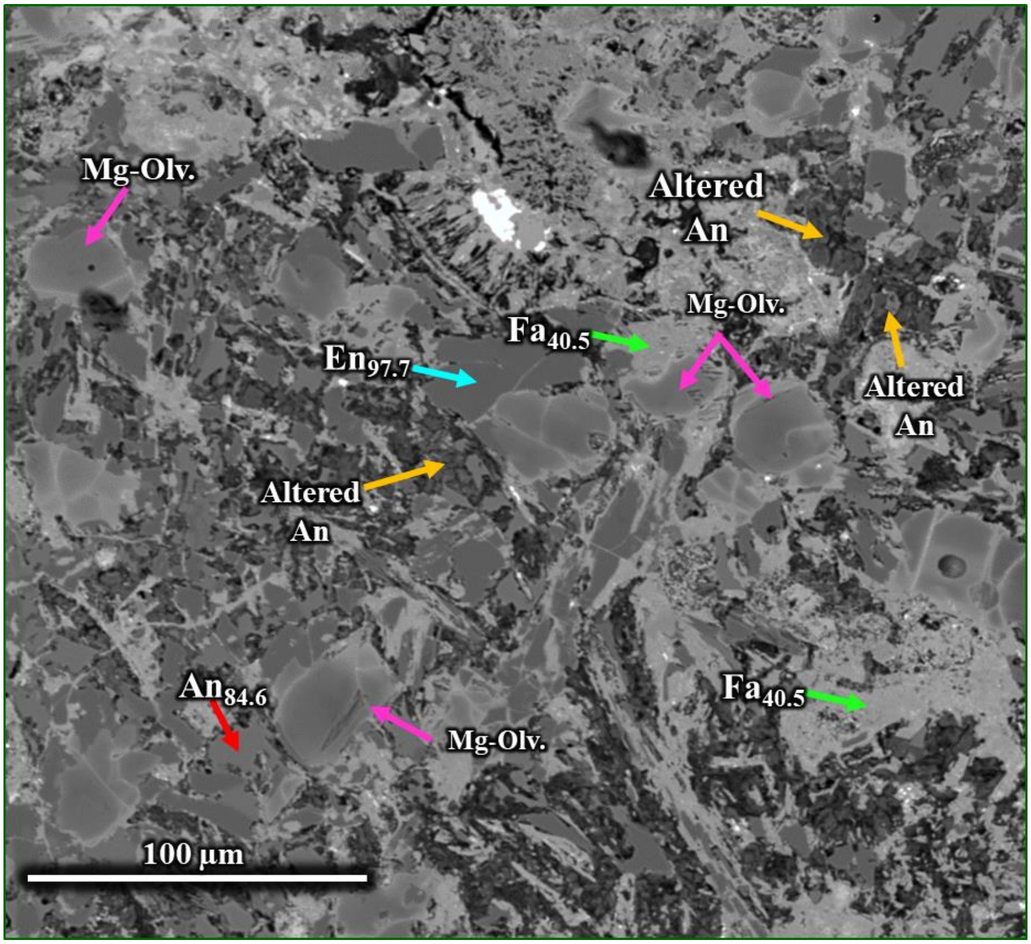

Figure 6: High magnification BSE image showing the locations of individual electron microprobe analyses (1 µm beam size) taken from a host type IAB chondrule. At least three different minerals were identified; original anorthite ($An_{84.6}$), enstatite ($En_{97.7}$), and ferroan olivine ($Fa_{40.5}$). The fourth is a high Al-bearing alteration phase of the anorthite (labeled "Altered An") that has not been identified. The ferroan olivine is replacing phases within the chondrule. The forsteritic olivine (Fo) grains show signs of Fe enrichment along cracks and grain boundaries. Enstatite grains (En) show variable degrees of replacement by ferroan olivine (Fa).

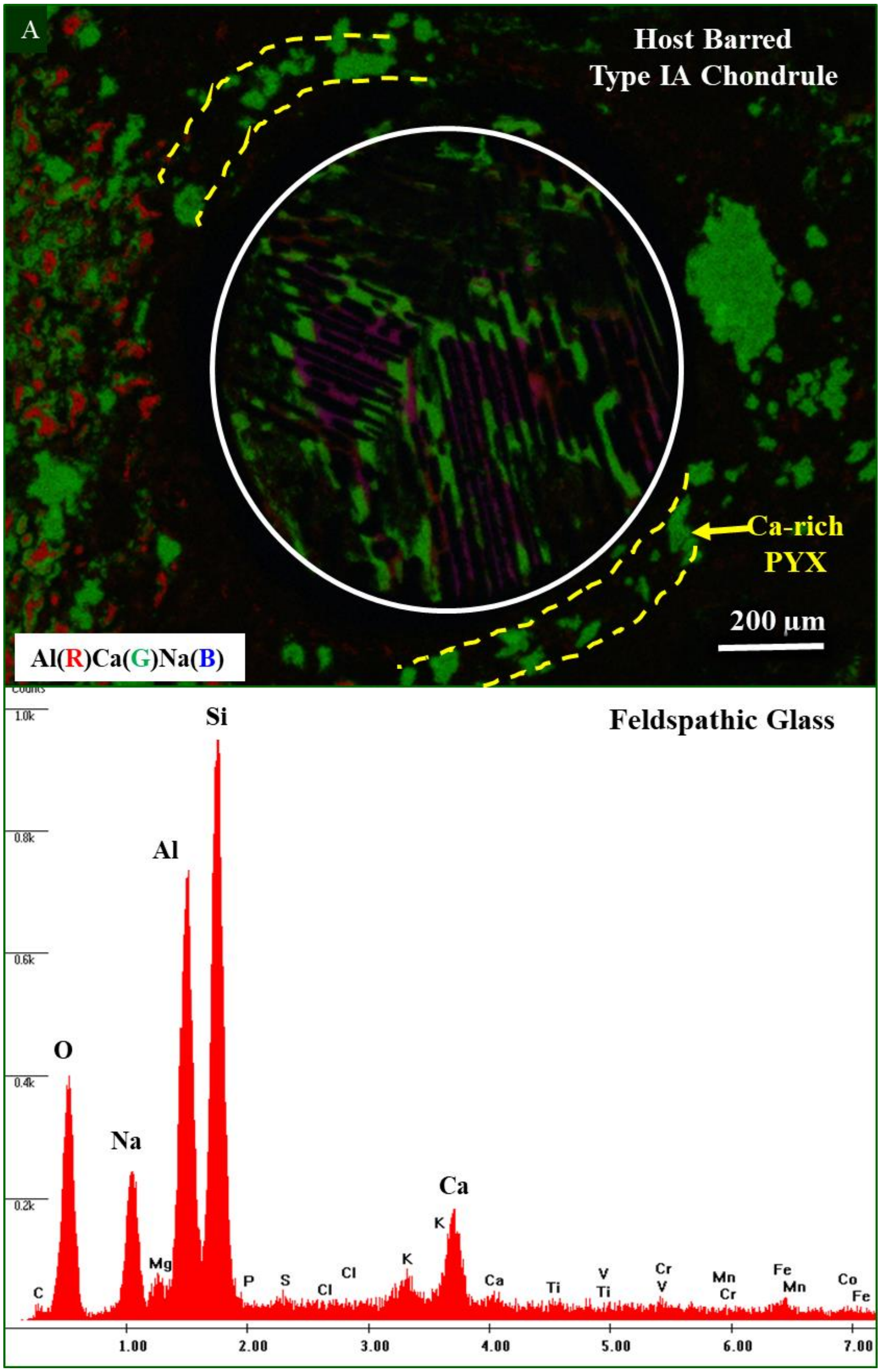

Figure 7: (A) Composite RGB Al-Ca-Na X-ray map of the barred type IA chondrule shown in Figure (5) showing unaltered chondrule mesostasis remaining in the interior of chondrule between the olivine bars that appear black in the image. Chondrule glass has generally been altered in the exterior of the inclusion, indicated by the lack of Ca and Na. Abundant Ca-rich pyroxene (PYX) is also present within the chondrule and as irregular aggregates in the matrix outside the chondrule (B) EDS spectrum showing the mesostasis consists of a feldspathic glass.

3.1.2.iii. Host Matrix

Figure 8a shows a BSE image of a representative region of the matrix material within the host. The matrix is relatively porous and consists primarily of platy, ferroan olivines that range in size from few microns to a few tens of microns. In addition to ferroan olivine, X-ray maps show that the matrix also contains approximately 8.5 vol% Ca-rich phases that mainly occur in porous, irregularly-shaped aggregates, a few microns to a few tens of microns in size that consist dominantly of Ca-Fe-rich pyroxene (hedenbergite) (Figure 8b). These aggregates are heterogeneously distributed within the matrix, but in some cases appear to be concentrated in zones around the exterior of chondrules (e.g., Figure 7a). Minor amounts of fine-grained Al-bearing phases (sub-micron to a few microns in size) also occur in the matrix that qualitative EDS analysis suggests are most likely hercynitic spinels (Figure 9a & 9b). Based on Al X-ray maps, the modal abundance of hercynite is approximately 4 vol% distributed throughout the matrix.

Backscattered imaging shows that distinct, curved features are present within the matrix that sometimes completely surround chondrules, AOAs, and CAIs (Figure 10a-d). These features are apparent in the BSE images as higher Z zones, notably on their outer edges, suggesting an enrichment in Fe and are distinct features from the fine-grained rims that surround many chondrules. We term these features ‘haloes’, because they resemble the features described by Hanowski and Brearley (2000) surrounding altered metal grains in CM chondrites. Like the aureoles described by Hanowski and Brearley (2000), their outer edges are defined by distinct zones ranging from a few microns to around 20 microns wide, which show the highest BSE contrast. The characteristics of these zones is variable. Some are very narrow and well defined, as seen in Figure 10a, whereas others are wider and may be up to 100 microns in width (Figure 10c). A typical feature is that they have an outer edge with the matrix which is quite sharp, rather than diffuse as seen in Figure 10a, c, whereas the inner side of the zone is more typically diffuse and extends into the matrix on the concave side of the curved Fe-rich halo, with a progressive decrease in BSE contrast. Some of the haloes contain small, rounded, low Z, inclusions that are only a few microns in size (Figure 10d). These inclusions could not be identified, but may be either pores or alternatively might be inclusions of C-rich material.

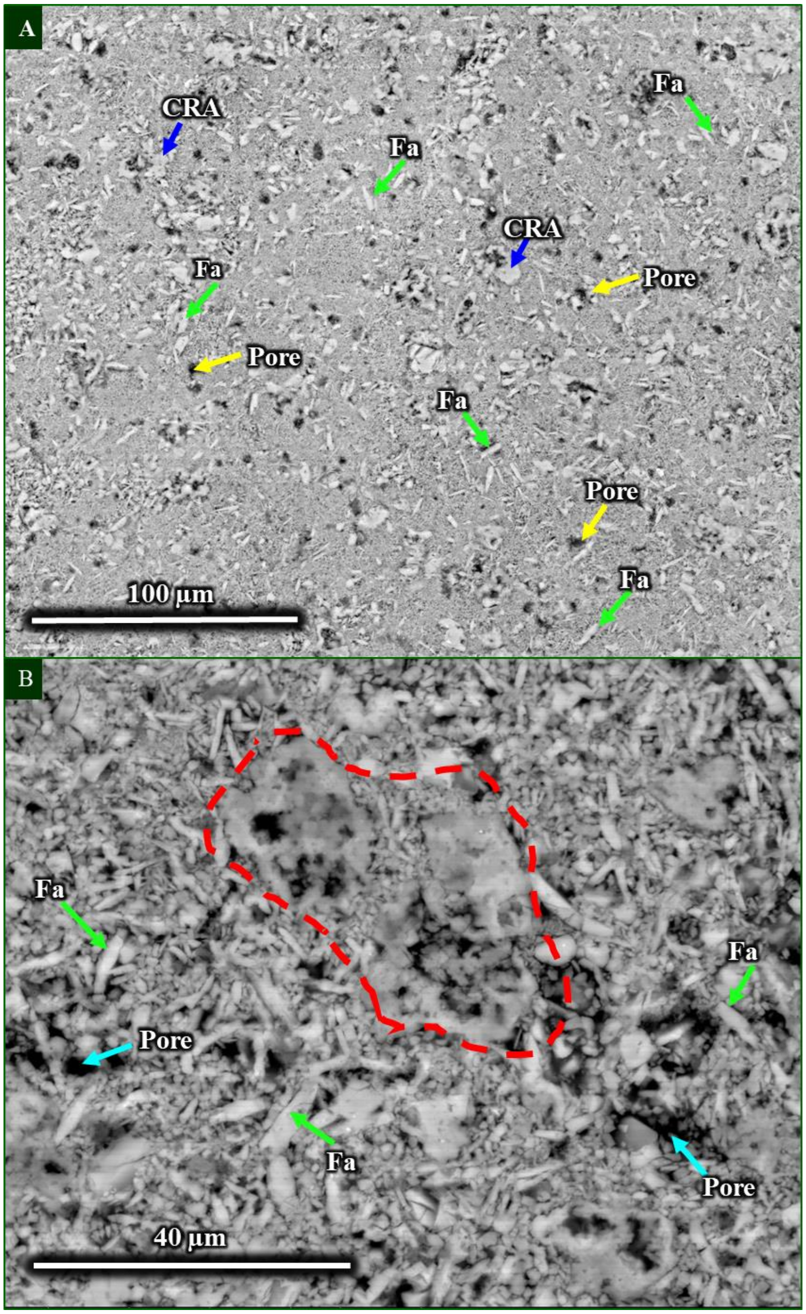

Figure 8: (A) BSE image of a representative region of the host NWA 2364 matrix. The matrix is very fine-grained and has a high porosity. Examples of pore spaces are indicated yellow arrows. The matrix is composed primarily of elongate, ferroan olivine grains (Fa – green arrows), a few microns to a few tens of microns, but the majority are micron sized or smaller. Calcium-rich aggregates (CRA – blue arrows) a few microns to a few tens of microns in size are also present within the host matrix.(B) high magnification BSE image of an example of a Ca-rich aggregate (outlined by red dashed line) and the adjacent matrix material.

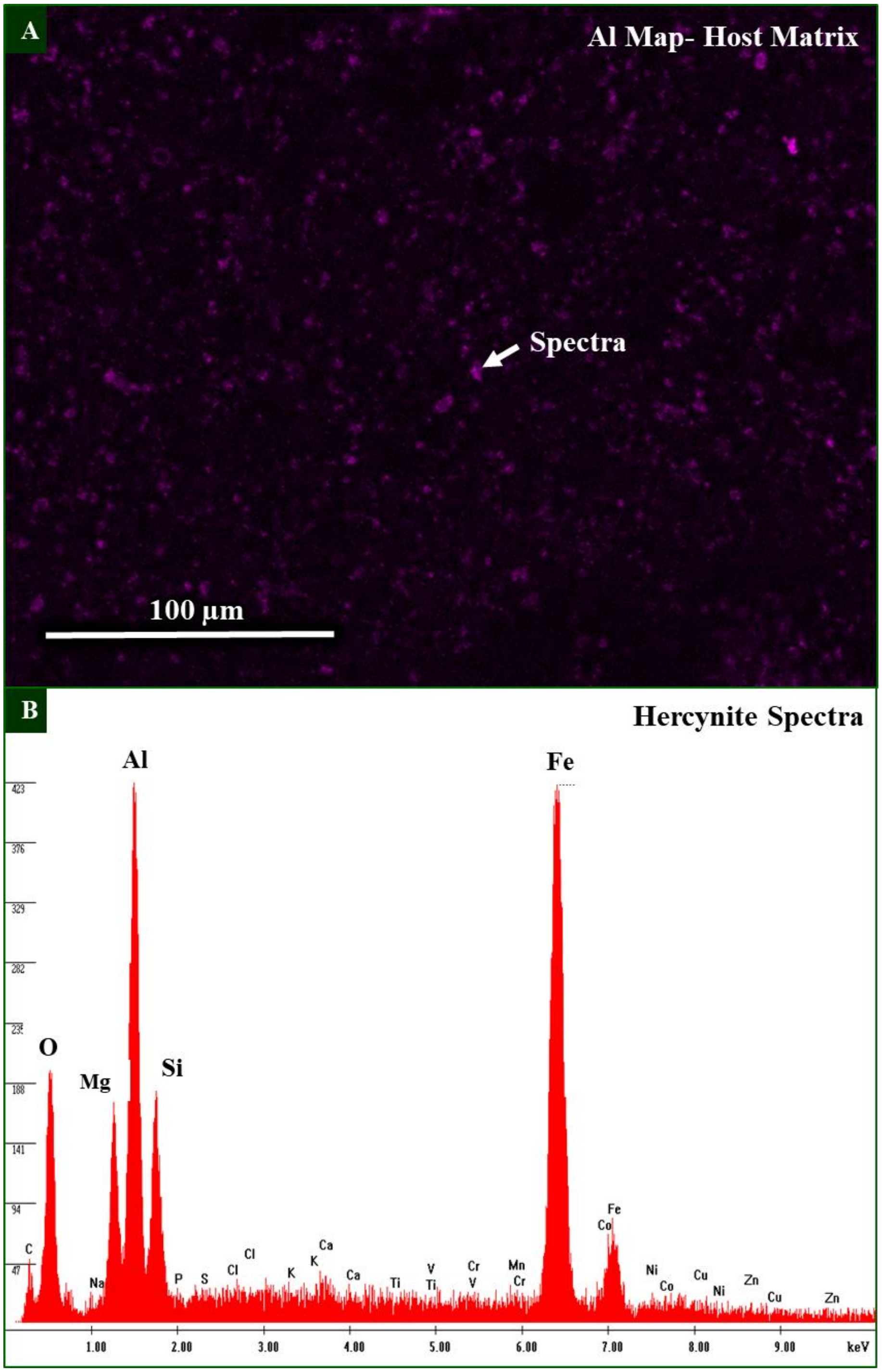

Figure 9: (A) Aluminum X-ray map of a representative region within the matrix showing that fine-grained Al-rich phases are present distributed throughout the matrix at a fine scale. The EDS spectrum shown in (B) was taken from the spot indicated with the white arrow. (B) EDS spectrum showing the composition of the Al-rich grain from the matrix. EDS indicates these Al-rich phases are hercynitic spinel. The Si peak in the spectrum is due to beam overlap with adjacent silicate phases, due to the small size of the grain.

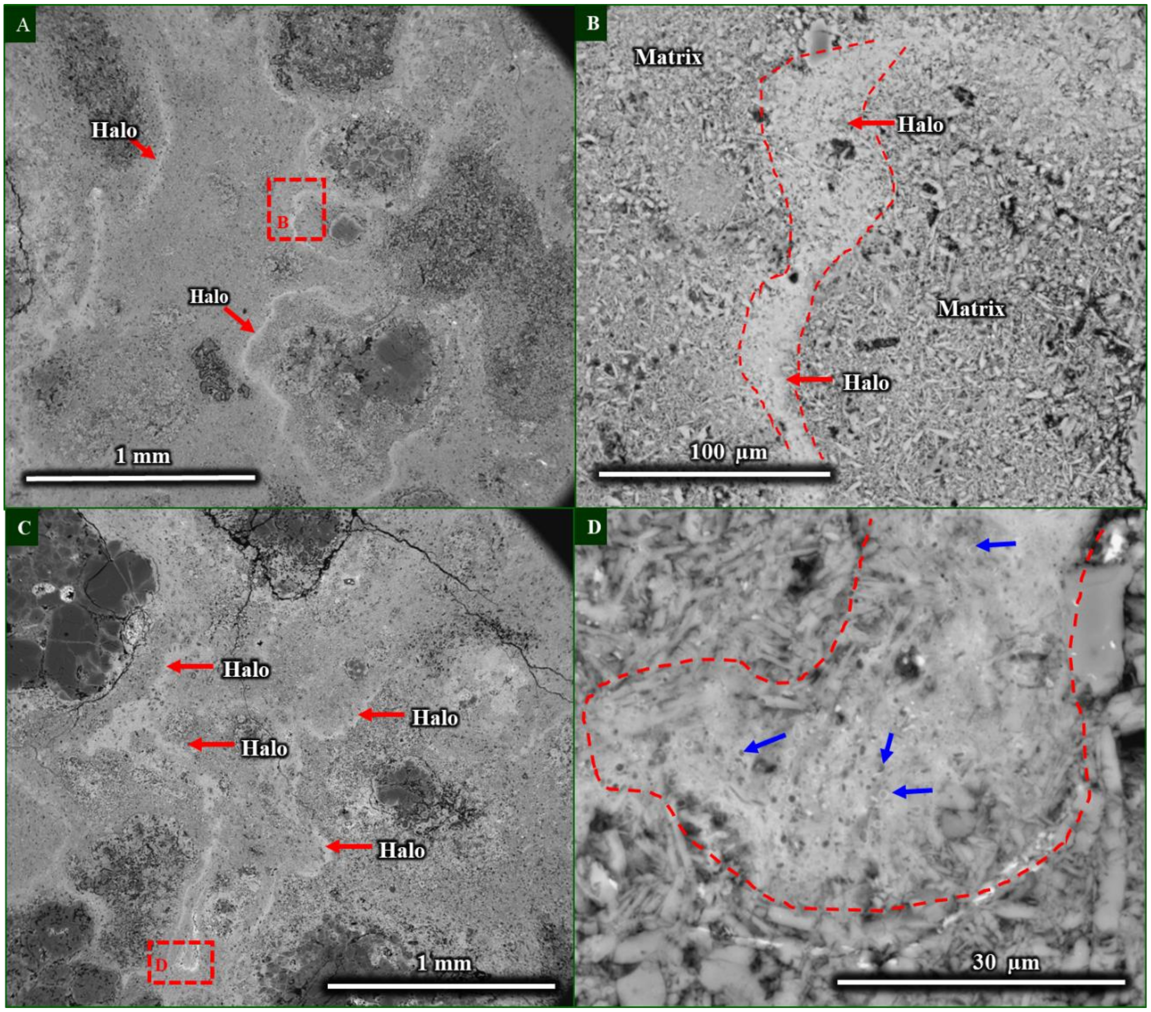

Figure 10: (A) BSE image of a region within the host NWA 2364 chondrite showing the relationship between the high Z halos found within the matrix and other objects within the host meteorite. (B) Higher magnification BSE image of the region of a halo from the area outlined in red in (A). The high Z zone is the prominent part of the halo with a lower porosity than the matrix material on either side of it. (C) Another region within the host showing the widespread distribution and heterogeneity of the halo features. (D) BSE image of boxed region (outline in red) showing the halo feature within the matrix at higher magnification. The halo region is much finer grained than the surrounding matrix, has a lower porosity, and contains sub-micron to micron high-Z and low-Z inclusions (indicated by blue arrows). The low Z may be very small pores, or may be inclusions of carbon-rich material.

3.1.3. Lithic Inclusion (LI)

The LI in NWA 2364 is very large, approximately 1-1.5 cm in size and consists of different features to that of the host meteorite. In the hand sample, shown in Figure 1, the LI is a lighter tan color than the host and resembles the shape of a deformed rectangle. Macroscopically, the LI is finer grained, and contains a much higher percentage of fine-grained material that the host. The matrix of the LI is finer grained than the host and has fewer chondrules that range from a few tens of microns to approximately 500 microns in diameter (Figures 1 & 2). There are also many isolated olivine grains embedded in the matrix that are either Mg-rich or Fe-rich, which the host lacks. Two CAIs, each about 200 microns in size and an isolated AOA were identified in the LI. The CAIs, chondrules, AOA, and matrix material identified in the LI all contain features indicative of secondary alteration. The abundances of Ni, Fe metal and sulfides in the clast are very low (<1%). Like the host section, there are no visible veins of Fe-oxyhydroxide or Ca carbonate cutting through the section, and the LI shows minimal reddish-brown staining compared with the host.

3.1.3.i. Lithic Inclusion CAIs

Both CAIs in the LI are the fluffy textural type of CAI. These CAIs are similar in size to the smallest CAIs reported for the host. They are approximately 200 microns in diameter and a representative example of ones of these CAIs is seen in Figure 11a-b. Based on X-ray maps and electron microprobe analyses (see Table 18), the CAI shown in Figure 11 is spinel-rich consisting of nodules of spinel that is are hercynitic spinel in composition. Smaller amounts of perovskite in are also present. Detailed studies of these CAIs were beyond the scope of this study. Future work will fully characterize these CAIs and their alteration phases.

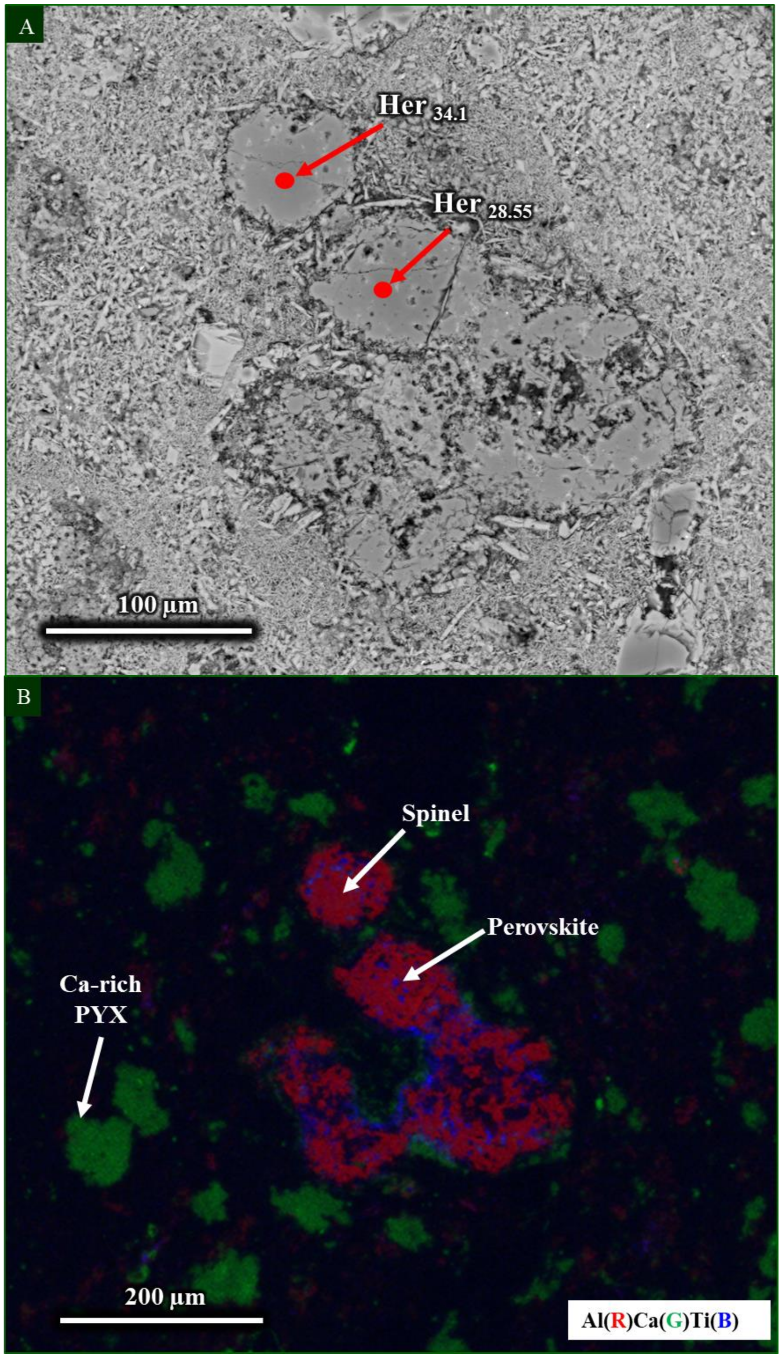

Figure 11: (A) BSE image of a fluffy, spinel-rich CAI in the LI. The compositions of hercynitic spinel measured at two points by EPMA are shown. The upper composition is Her$_{34.1}$ and the lower one is Her$_{28.55.}$ (B) Al-Ca-Ti RGB composite X-ray map of the same CAI, showing the CAI is rich in spinel (red phase) with some minor perovskite (blue phase). Numerous Ca-rich pyroxene aggregates (green) occur in the matrix surrounding the CAI.

3.1.3.ii. Lithic Inclusion Chondrules and Isolated Grains

In total, the LI contains 15 chondrules; 6 type IIA and 9 type IA, so the abundance of type IIA chondrules present is higher in the LI than in the host. All of the chondrules identified within the LI are porphyritic olivine chondrules. Representative examples of these chondrules are shown in Figures 12a-c. Surrounding many of the chondrules are fine-gained rims consisting of micron-sized elongate, ferroan olivine grains. The LI contains numerous isolated grains of Mg and Fe-rich olivine that range in size from a few tens of microns to ~200 microns (Figures 13a &13b). These isolated grains occur in a higher abundance than chondrules. The isolated grains are usually anhedral, with either jagged or rounded morphologies. The abundance of Mg-rich to Fe-rich isolated grains mimics that of the relative abundance of the type IA and type IIA chondrules.

In both types of chondrules and isolated grains, the olivine phenocrysts are decorated with chromite grains, a few a few microns to ~20 microns in size. These chromite grains are found along the periphery of the chondrule phenocrysts, within the chondrule phenocrysts, within the Fe-enriched fractures in the interior of the phenocrysts, and within the altered chondrule mesostasis (Figure 12c). The larger chromites found are often subhedral and, in many cases, have fractures running through them. The smaller ones that occur with phenocrysts are euhedral and often occur near the edges of the phenocrysts and along the Fe-enriched fractures in chondrule phenocrysts and isolated olivine grains (Figure 18b).

Both types of chondrules are surrounded by distinct fine-grained rims consisting of elongate ferroan olivines that are heterogeneous in size; ranging from a few microns up to 100 microns (Figures 12b & 14a). These rims are significantly more fine-grained than the matrix between the chondrules. Fine-grained rims are only rarely present on isolated olivine grains.

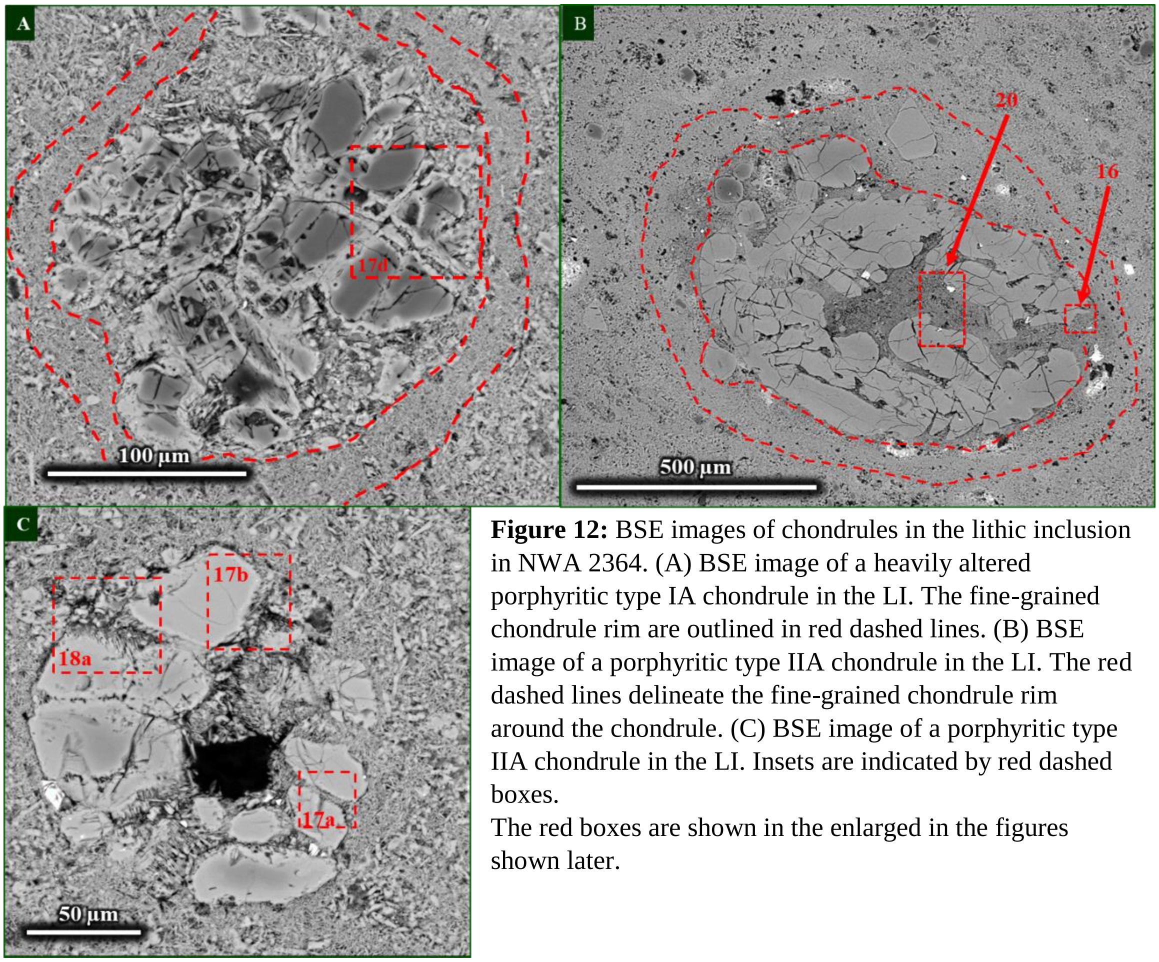

Figure 12: BSE images of chondrules in the lithic inclusion in NWA 2364. (A) BSE image of a heavily altered porphyritic type IA chondrule in the LI. The fine-grained chondrule rim are outlined in red dashed lines. (B) BSE image of a porphyritic type IIA chondrule in the LI. The red dashed lines delineate the fine-grained chondrule rim around the chondrule. (C) BSE image of a porphyritic type IIA chondrule in the LI. Insets are indicated by red dashed boxes.
The red boxes are shown in the enlarged in the figures shown later.

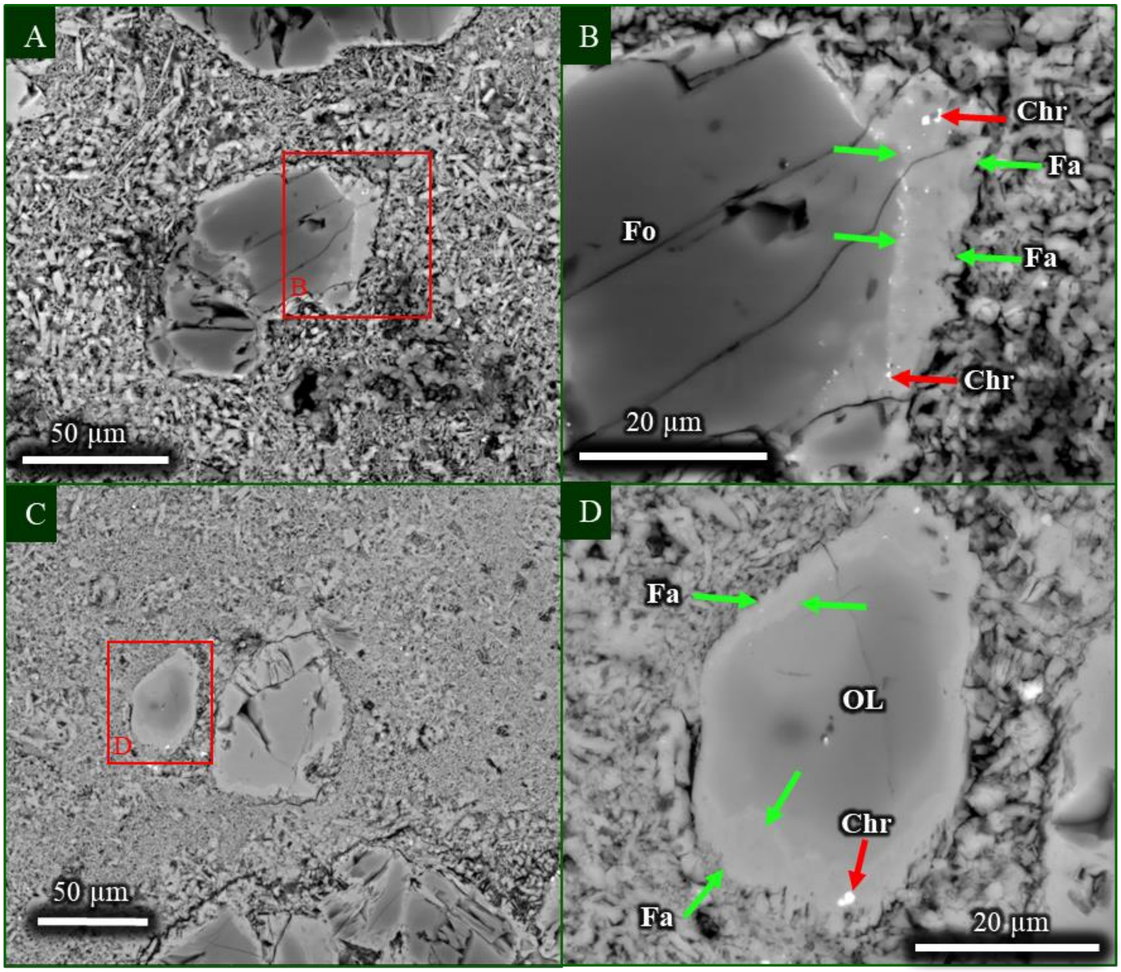

Figure 13: BSE images of isolated grains in the NWA 2364 lithic inclusion. (A) Example of an Mg-rich isolated olivine grain in the LI. (B) High magnification view of the boxed region in (A) of the ferroan overgrowth (indicated by green arrows and labeled Fa) around the edge of the grain. Within the ferroan overgrowth, there are submicron- to micron-sized chromite grains (Chr indicated with red arrows). (C) Fe-rich isolated olivine grains in the LI. (D) high magnification view of the ferroan overgrowth (Fa, indicated by green arrows). The micron-sized chromite (Chr) grains within the ferroan overgrowth are indicated by red arrows.

The chondrule types and isolated grains exhibit a range of textural and compositional features that are indicative of secondary alteration. These features include; Fe-enrichments along fractures and cracks within olivine phenocrysts, overgrowths of ferroan olivine along the edges of chondrule olivine phenocrysts, complete replacement of chondrule mesostasis, replacement of low-Ca pyroxene in chondrules by ferroan olivine, replacement of opaque nodules in chondrules, the development of cross-cutting veins within chondrule phenocrysts, and complete pseudomorphic replacement of chondrules by ferroan olivine. Although all chondrules in the LI have been modified, these secondary features are variably developed depending on the primary mineralogy, and grain size of the original chondrules, as well as the size of the chondrule themselves.

Figure 12c is a representative example of a chondrule that has experienced the least amount of alteration. The largest porphyritic chondrule olivine phenocrysts remain and have not been as extensively replaced as olivine in the chondrule shown in Figure 14b. Figure 14a shows a chondrule with an intermediate degree of alteration. Some of the original olivine phenocrysts remain, but the mesostasis material has been replaced by ferroan olivines. Complete pseudomorphic replacement has occurred in a number of chondrules in the lithic inclusion (Figure 14a, b). Figure 14b is a representative example of one of these chondrules where the outline of the chondrule remains, but all the primary minerals have been completely pseudomorphed by elongate, ferroan olivines. Interstial to the larger, elongated ferroan olivines are very fine-grained olivines (a few microns in size) that likely replaced original chondrule mesostasis glass and possibly other phases.

The chondrules present within the LI are lacking low-Ca pyroxenes are notably rare or absent in chondrules in the LI. Figure 14c is an example of a chondrule that has a few relict low-Ca pyroxene grains still remaining, but the chondrule has been highly altered and replaced by ferroan olivines.

Along the fractures and cracks within the chondrule olivine phenocrysts and isolated grains there are narrow zones that are higher in Fe (Figure 12a). These zones vary in width between individual chondrule phenocrysts and isolated grains. In addition to the zoning along fractures, type IA chondrule olivine phenocrysts and forsteritic isolated grains exhibit ferroan olivine overgrowths around the edges of the original phenocrysts (Figures 13a, b, 14a, 15b, 16a). The width and occurrence of these ferroan overgrowths is heterogeneous between individual olivine phenocrysts within the same chondrule, not just from chondrule to chondrule. The forsteritic isolated grains also have variations in the occurrence and width of the ferroan overgrowths. One edge of an isolated grain may have a wide ferroan overgrowth while another edge of the same crystal may exhibit a very narrow one (Figure 13a & 13b). In general, the widths of these ferroan overgrowths range from a few microns to ~50 microns. In most cases, the ferroan overgrowths are wider closer to the edge of the olivine phenocrysts than along their interior edges. The interface between the forsteritic chondrule olivines and the ferroan overgrowths show distinct zoning in Fe over a few microns into the interior of the forsterite grains. Many of the ferroan overgrowths on chondrule phenocrysts and isolated grains contain submicron- to micron-sized chromite inclusions. Distinct voids or pore spaces are also present within the overgrowths (Figure 13a, b, & 40a). Sometimes, platy, oriented, ferroan olivines a few microns in size are present that radiate from the edge of the ferroan overgrowths. These olivines are typically not well developed and occur in rare instances with the more extensive ferroan overgrowths.

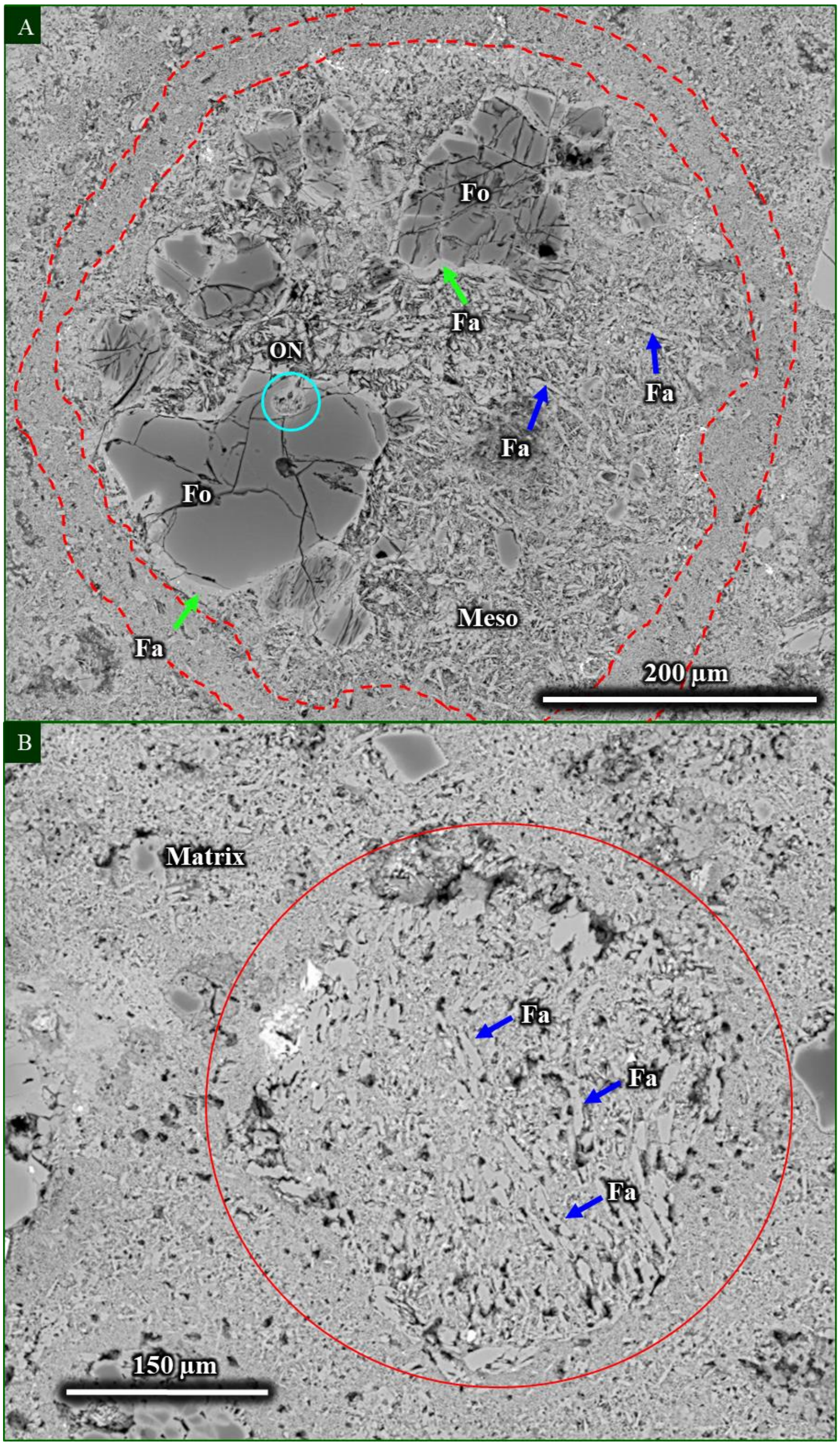
A
Fo
Fa
ON
Fa
Fa
Fa
Fo
Fa
Meso
200 µm
B
Matrix
Fa
Fa
Fa
150 µm

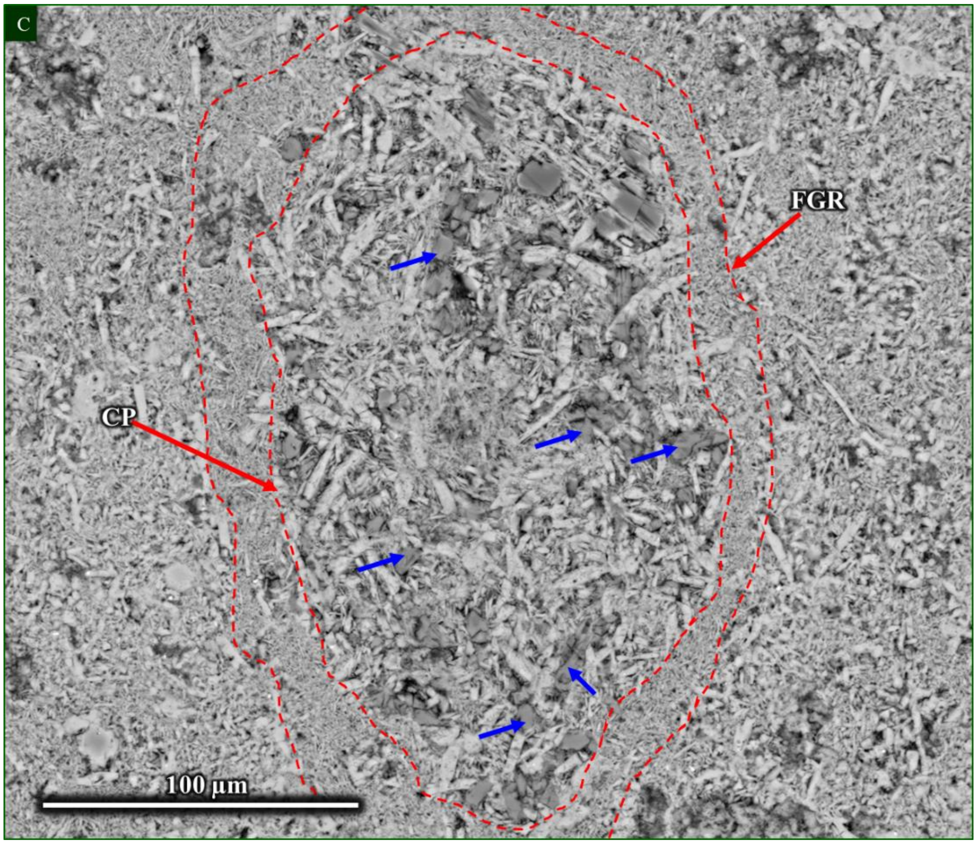

Figure 14: BSE images showing a range of degrees of replacement of chondrules in the NWA 2364 lithic inclusion. (A) BSE image a partially replaced type IA chondrule in the LI. Original chondrule olivine phenocrysts are labeled "Fo" and the altered chondrule mesostasis is labeled "Meso" The mesostasis material and other original phases were replaced by elongate, ferroan olivine grains (Fa -dark blue arrows) of varying sizes in random orientations. The chondrule olivine phenocrysts have ferroan olivine overgrowths around their peripheries (Fa - indicated by green arrows). Iron enrichment is also present along cracks and fractures in the forsteritic olivine phenocrysts. This chondrule also contains a metal nodule that has been replaced by ferroan olivine (ON - circled in light blue). A fine-grained chondrule rim is present around the chondrule (red dashed line). (B) BSE image of a chondrule that has been completely pseudomorphed by ferroan olivines (Fa). The outline of the original chondrule is shown in red. Very fine-grained ferroan olivines and larger, elongate ferroan olivine grains are present. (C) BSE image of a chondrule pseudomorph that has a few grains of original low Ca-pyroxene (indicated with the blue arrows) still remaining within the mesostasis material. The chondrule pseudomorph (CP) is outlined in red and is surrounded by a fine-grained rim (FGR).

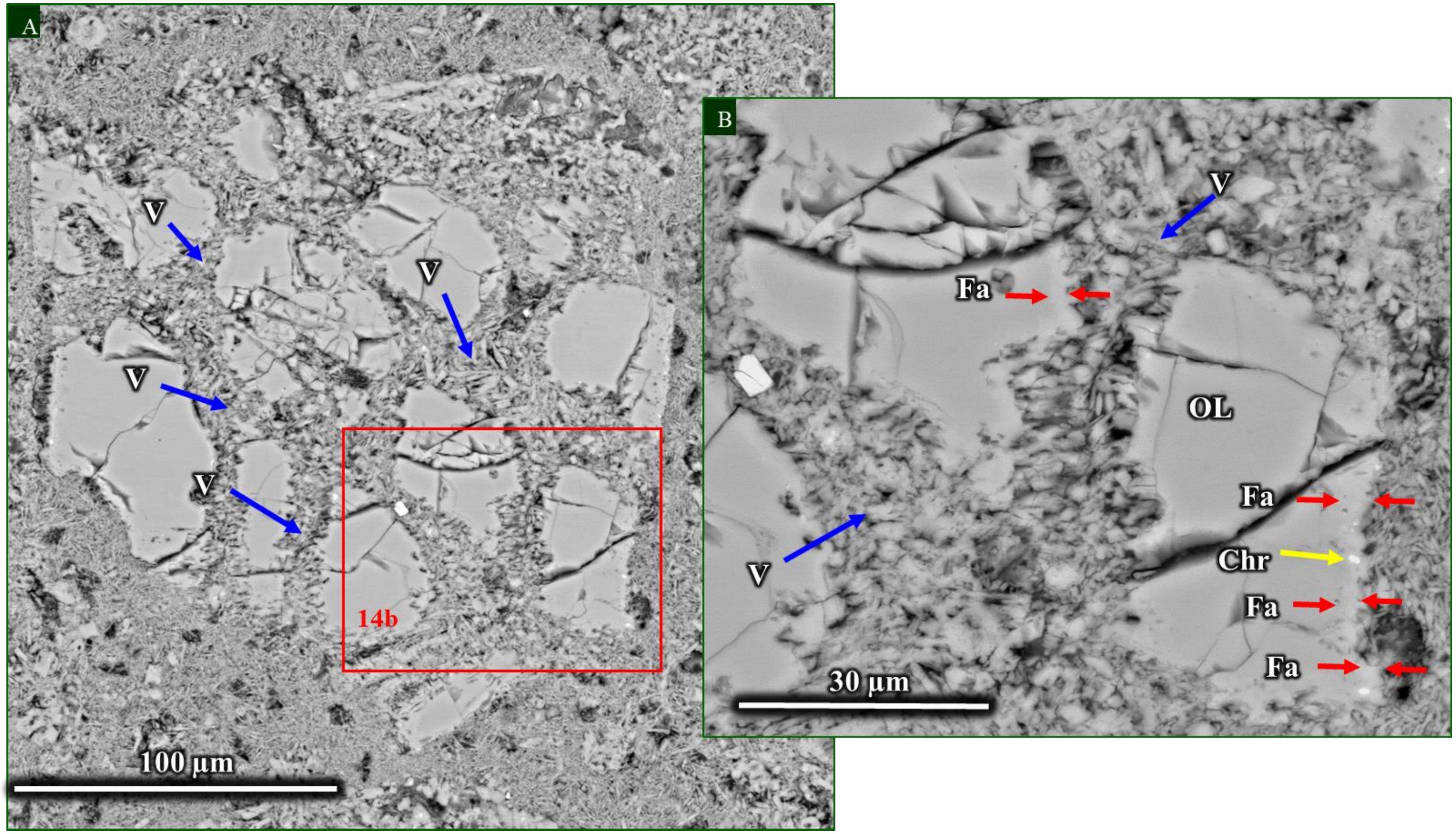

Figure 15: (A) BSE image of a type IIA chondrule in the LI that exhibits ferroan overgrowths around the edges of the olivine phenocrysts. In between the chondrule olivine phenocrysts are randomly oriented ferroan olivine grains that grew in veins (V – blue arrows) within fractures in the phenocrysts. (B) Enlargement of boxed are in 14a showing ferroan overgrowths indicated by the red arrows (labeled "Fa"). These overgrowths are very similar to those seen in the type IA chondrules and the Mg-rich isolated grains. These ferroan overgrowths are porous and contain submicron- to micron-sized chromite grains (Chr – yellow arrow).

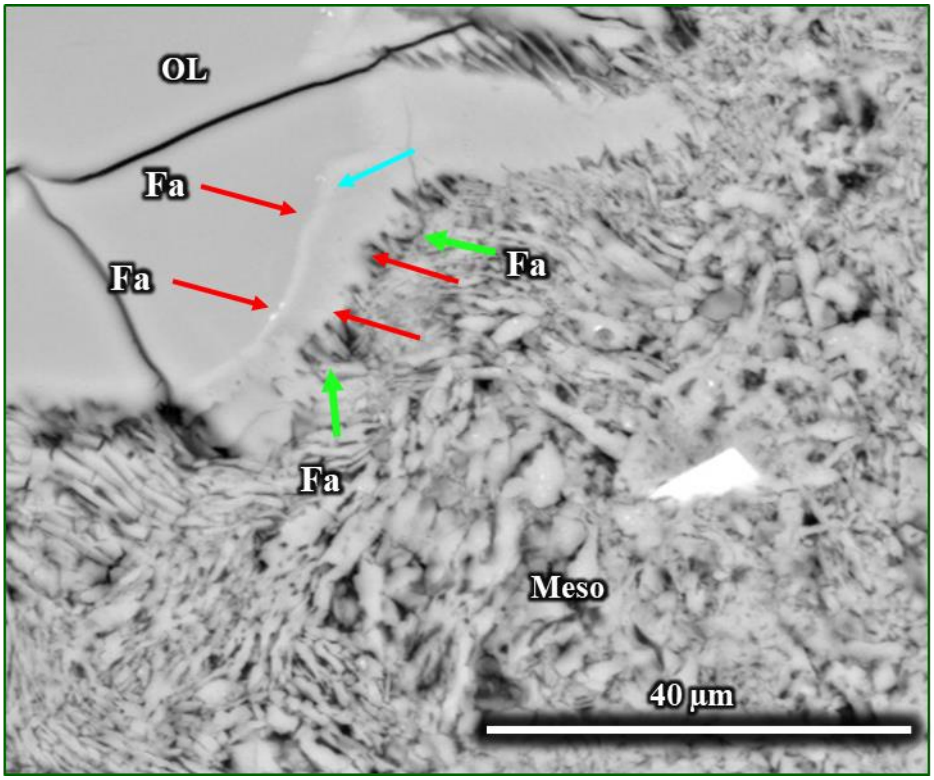

Figure 16: High magnification BSE image of the inset from the barred type IIA chondrule from Figure 11b. The chondrule olivine phenocryst (OL) exhibits a prominent ferroan overgrowth (Fa -red arrows), a very narrow Fe-enrichment where the phenocryst meets the ferroan overgrowth (indicated by the light blue arrow). At the serrated edge of the ferroan overgrowth is another example of the growth of the elongated, ferroan olivine grains (Fa-green arrows). Just as in (A) the chondrule mesostasis (Meso) has been replaced by elongate, ferroan olivines.

The type IIA chondrules and Fe-rich isolated olivine grains also exhibit ferroan overgrowths, which have not been described before in type IIA chondrules in CV3 chondrites or dark inclusions. These ferroan overgrowths also vary in width and occurrence within the same chondrule and isolated grain (Figure 13c, 13d, 15a, & 15b). In general, the widths of these ferroan overgrowths vary from a few microns to approximately 20 microns. The characteristics of the ferroan overgrowths are identical to those on the type IA chondrule olivine and show all of the same features (Figure 13c, 13d, 15, 17a, & 17c). While this narrow zonation of Fe-enrichment is more common in the type IA chondrule olivine phenocrysts it is observed in some cases, around the edge of the chondrule olivine phenocrysts and Fe-rich isolated grains (Figure 16), where the ferroan overgrowth meets the edge of the phenocryst.

One distinct characteristic of the ferroan overgrowths in type IIA chondrules that is rarely seen on forsteritic olivines is the presence of overgrowths of platy, oriented, ferroan olivines that radiate from the edges of the ferroan overgrowths (Figure 16). In the type IIA olivine phenocrysts, these are common and more distinct than the overgrowths on forsteritic olivines in type IA chondrules. Iron-rich isolated grains with wider ferroan overgrowths sometimes also exhibit similar textures, but they are rarer and less well developed. These oriented, ferroan olivines are variable in occurrence and width (a few microns in size) and are not always present along the entire ferroan overgrowth. In their more prominent occurrences, they follow the shapes of the chondrule phenocrysts (Figure 16).

Many of the inclusions of Fe-Ni metal in chondrule olivine phenocrysts have been completely replaced by magnetite, Fe-Ni sulfides, and even further by ferroan olivines (Figure 14a). However, some very small, micron-sized grains, in some of the type IIA chondrules remain unaltered. Figure 41 shows a representative example surviving metal grains the center of a phenocryst, protected from alteration by the olivine. In most cases in the type IA chondrules and other type IIA chondrules they.

In addition, chondrule phenocrysts in both type I and II chondrules exhibit cross cutting veins. These veins range in width from 5 to ~30 microns. These veins are very distinct in texture from the ferroan olivine overgrowths described above. The veins occur crosscutting individual chondrule phenocrysts, but very similar features are also present along the grain boundaries between individual chondrule phenocrysts. Representative examples of these features from different chondrules are shown in Figures 17a-j. The characteristics of the veins show some differences between type I and type II chondrules, but there are also some textural differences within individual chondrule types.

The veins that cross cut individual chondrule phenocrysts appear to have developed along fractures in the olivine and often have a zonal structure. The central part of the vein is highly porous and contains platy or anhedral ferroan olivines, with pore space between them (Figure 17d, e). Commonly, the platy olivines are parallel or subparallel and their long axes are oriented normal to the edge of the vein. However, there are other examples where the platy olivines in the vein are randomly oriented (Figure 15a, b). On the edge of the veins, more massive ferroan olivine is present in zones on either side of the vein, which are typically ~ 5 microns in width. However, this zonal structure is not always symmetric and can be thinner or absent on one side of the vein. In type I chondrule olivine phenocrysts, the interface between this zone of ferroan olivine and the phenocryst chondrule olivine can be very sharp and is sometimes defined by a crack or fracture (Figure 17c), but in other cases is not well defined and shows evidence of a compositional gradation. These same zones of massive ferroan olivine are also present in type II chondrule olivines, but sometimes show a well-developed serrated texture at their edges with the porous center of the vein that contains platy olivines (Figure 12c & 17a). The interface of the ferroan olivine zone with the unaltered phenocryst olivine is sometimes defined by the presence of submicron pores and possibly chromite crystals (Figure 17b). In some type II chondrules, the layer of ferroan olivine is much narrower or locally missing, but the edge of the olivine still displays the complex serrated texture (Figure 17f, g).

The serrated texture occurs along grain boundaries between the individual chondrule olivine phenocrysts (Figures 17a, b, i, j, & 18a-c) and along the edges of some isolated grains (Figure 18c). While this texture exists in both chondrule types, it is better defined in type IIA chondrule phenocrysts.

In comparison with the host, chondrule mesostasis and many original phases (i.e. low Ca-pyroxene) in the LI have been completely replaced by elongate, ferroan olivines in both types of chondrules. X-ray mapping of altered chondrules shows that Ca, Na, or Al-bearing phases are completely absent (Figure 19a, b). These elements are typically concentrated in the chondrule glass and/or in Ca-rich pyroxene, suggesting that complete alteration of both of these phases has occurred. Figures 14a & 17h are representative examples mesostasis material altered to ferroan olivines in chondrules.

The ferroan olivines occur in two different styles. The majority of the olivines that have replaced the mesostasis are randomly oriented and range in size from a few microns to a few tens of microns (Figure 14a &14c). Not all olivines are elongate; sometimes they are anhedral or truncated. In between the olivine grains are submicron to a few micron sized pore spaces. This porosity varies within chondrules, as well as from chondrule to chondrule and occurs in both the type IA and type IIA chondrule types.

The second style consists of elongate olivine grains that have grown topotaxially from the edge of olivine phenocrysts (Figure 12b with inset-Figure 20). These olivines resemble the oriented olivines described above in the vein textures. These topotaxial olivines can be found within the chondrule and between chondrule grain boundaries and are most commonly found with type IIA chondrules and Fe-rich isolated olivine grains. These oriented olivines are typically fine-grained only a few microns wide and a microns to a few tens of microns long, although a few larger grains do occur. Interstitial submicron to micron-sized pore space is present between the olivine grains. In some chondrules, olivine grains (Fig. 20) are very densely packed with minimal porosity, while in other chondrules large pore spaces are present between them. Oriented olivines around the edges of some of the Fe-rich isolated olivine grains appear similar to those observed in chondrules, but are typically smaller and are more anhedral (Figure 18c).

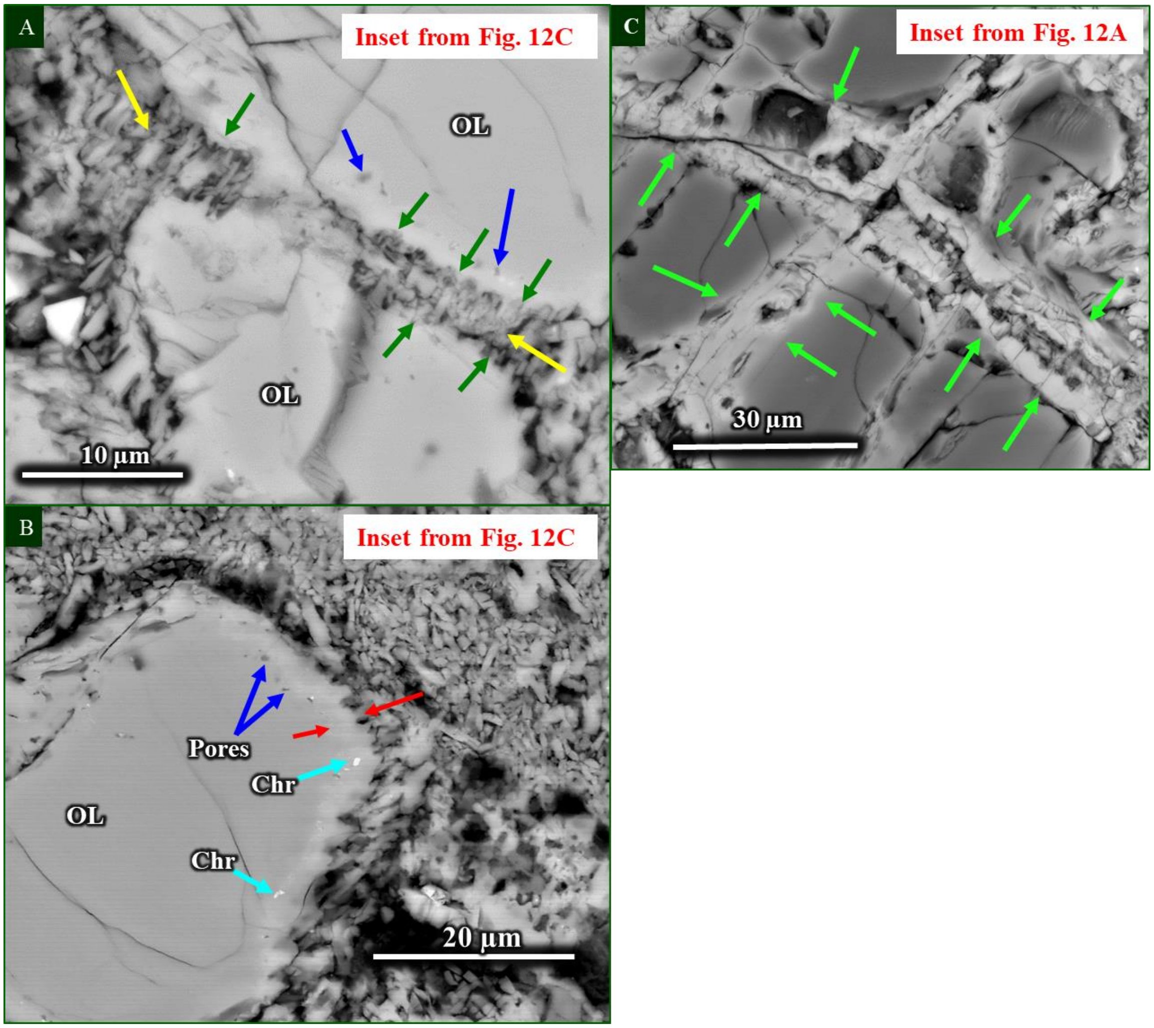

Figure 17a-c: (A) High magnification BSE inset image from Figure 12C, showing alteration features in olivine. A serrated texture (indicated by the green arrows) is present along the edge of the olivine phenocryst (OL). Along this margin there are submicron pore spaces indicated by the dark blue arrows. Crystallographically-oriented elongate, ferroan olivine grains filling a vein (yellow arrows). (B) High magnification BSE inset image from Figure 12C. Chondrule olivine phenocryst (labeled “OL”) along the edge of the main chondrule showing similar textures to those within the phenocryst in image 17A. Submicron pores are indicated by blue arrows and submicron chromite grains Chr – light blue arrows) Red arrows indicate the width of the altered zone with the serrated texture along the edge of the phenocryst. (C) High magnification BSE image of the inset from Figure 12A. This image shows the sharp contrast in the Fe-rich veins that have formed (green arrows) and the original Mg-rich chondrule phenocrysts.

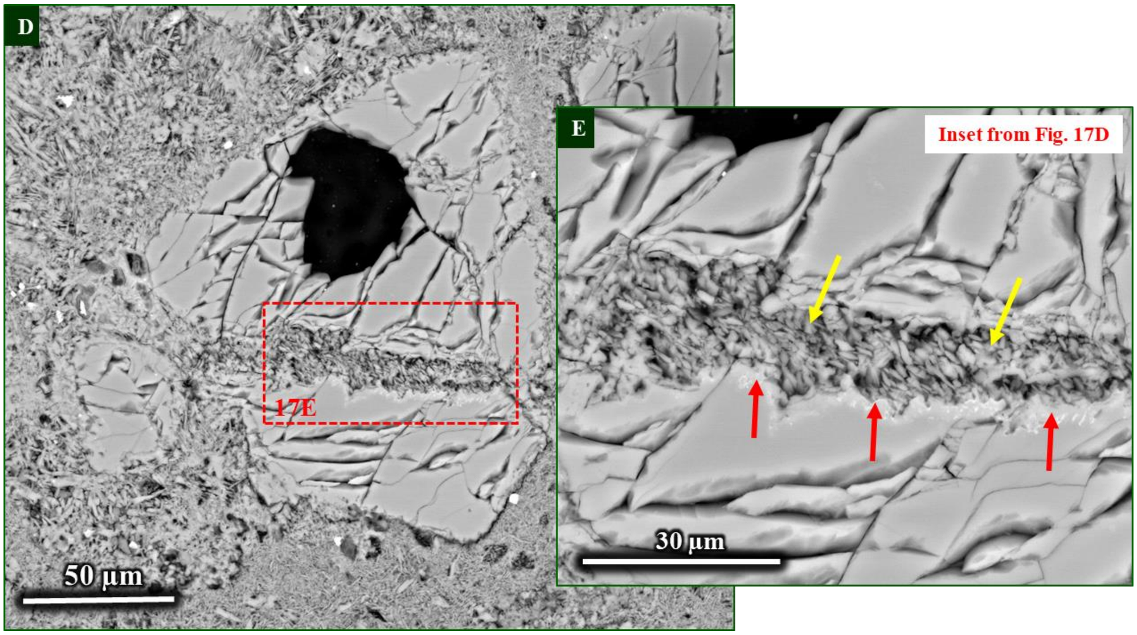

Figure 17 d-e: (D) BSE image of a type IIA chondrule in the LI. A large vein runs through the grain from left to right (boxed region). (E) High magnification BSE image of the inset from Figure 16D showing the anhedral, unoriented olivines filling the vein (yellow arrows) and the Fe-enriched, serrated edge of the phenocryst indicated by the red arrows. Significant porosity is present between the olivines within the vein.

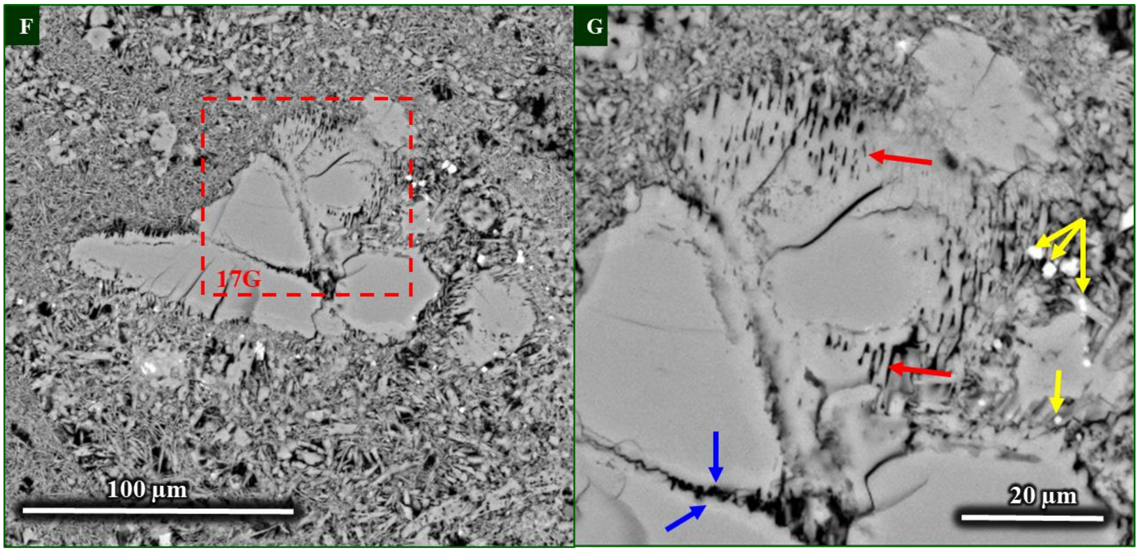

Figure 17 f-g: (F) BSE image of a type IIA chondrule in the LI. Only a small portion of the chondrule remains. The main focus of this image is the inset. (G) High magnification BSE image of inset from Figure 16F. Submicron to micron-sized chromite grains are present between the chondrule phenocrysts (yellow arrows). The red arrows show the locations where the elongate ferroan olivines have begun to grow. The blue arrows indicate the region where there ferroan olivine is absent, but the edges of these phenocrysts still have the Fe-enriched, serrated texture seen in the veins filled with the ferroan olivines (e.g. Figure 16a).

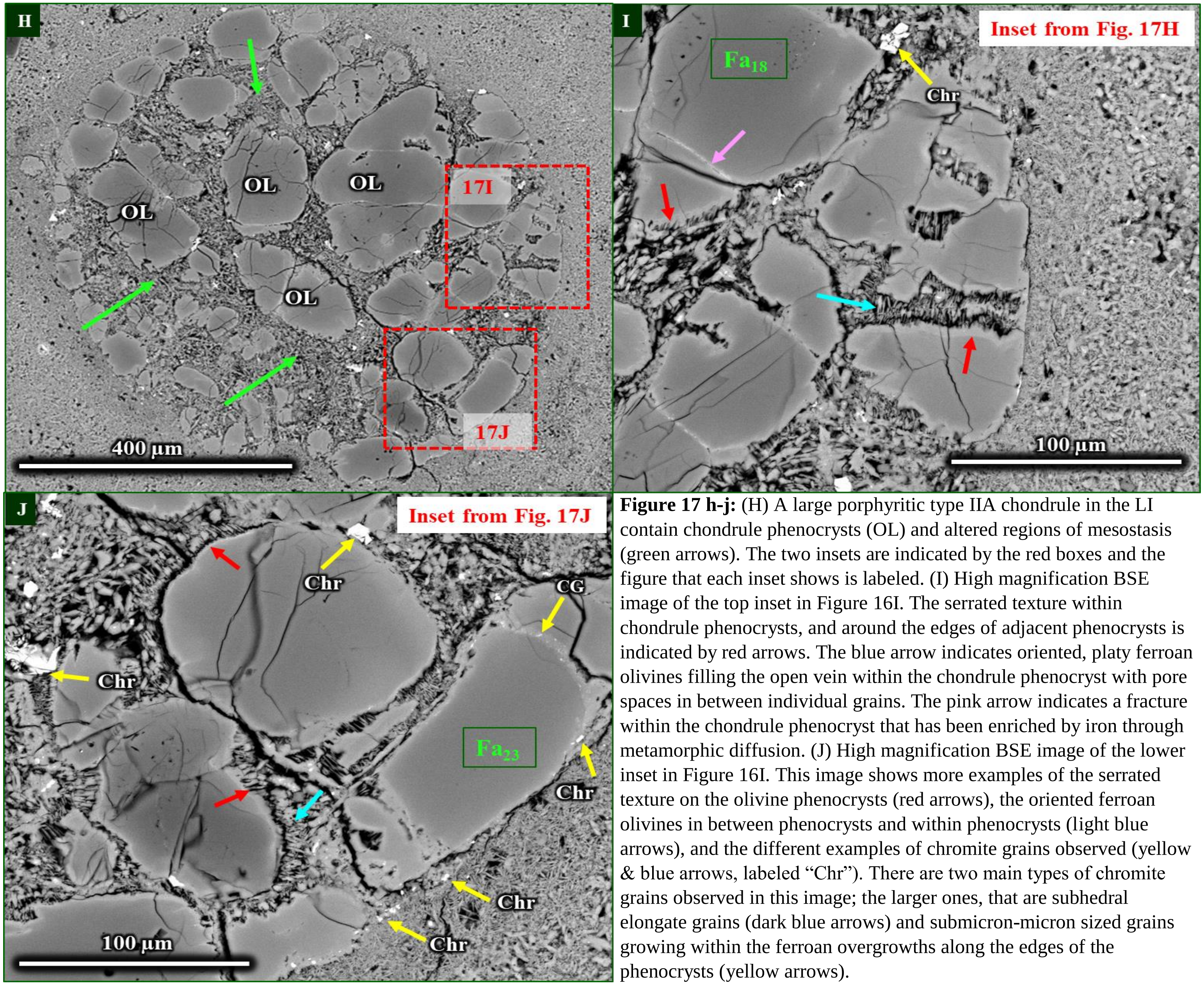

Figure 17 h-j: (H) A large porphyritic type IIA chondrule in the LI contain chondrule phenocrysts (OL) and altered regions of mesostasis (green arrows). The two insets are indicated by the red boxes and the figure that each inset shows is labeled. (I) High magnification BSE image of the top inset in Figure 16I. The serrated texture within chondrule phenocrysts, and around the edges of adjacent phenocrysts is indicated by red arrows. The blue arrow indicates oriented, platy ferroan olivines filling the open vein within the chondrule phenocryst with pore spaces in between individual grains. The pink arrow indicates a fracture within the chondrule phenocryst that has been enriched by iron through metamorphic diffusion. (J) High magnification BSE image of the lower inset in Figure 16I. This image shows more examples of the serrated texture on the olivine phenocrysts (red arrows), the oriented ferroan olivines in between phenocrysts and within phenocrysts (light blue arrows), and the different examples of chromite grains observed (yellow & blue arrows, labeled "Chr"). There are two main types of chromite grains observed in this image; the larger ones, that are subhedral elongate grains (dark blue arrows) and submicron-micron sized grains growing within the ferroan overgrowths along the edges of the phenocrysts (yellow arrows).

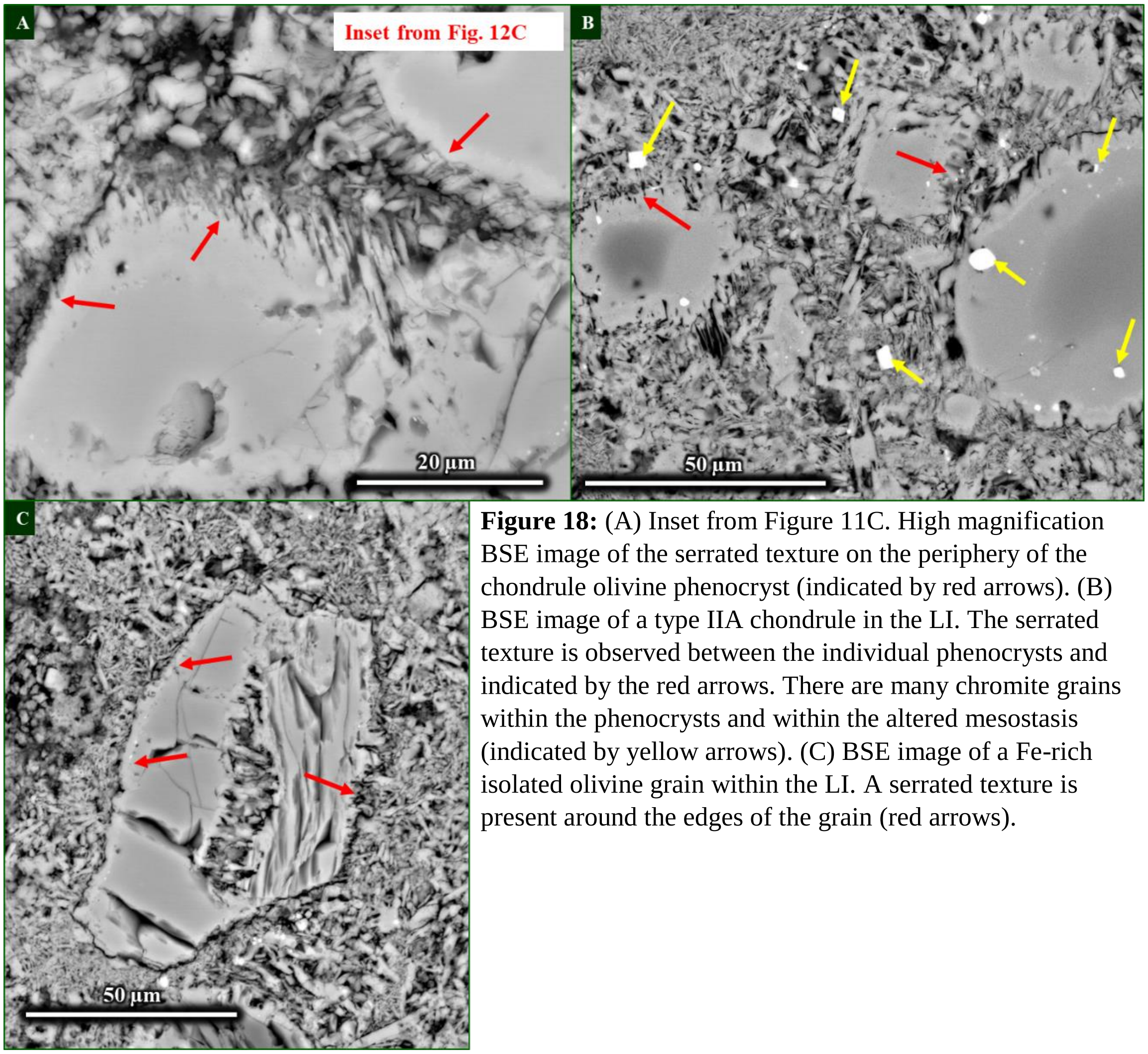

Figure 18: (A) Inset from Figure 11C. High magnification BSE image of the serrated texture on the periphery of the chondrule olivine phenocryst (indicated by red arrows). (B) BSE image of a type IIA chondrule in the LI. The serrated texture is observed between the individual phenocrysts and indicated by the red arrows. There are many chromite grains within the phenocrysts and within the altered mesostasis (indicated by yellow arrows). (C) BSE image of a Fe-rich isolated olivine grain within the LI. A serrated texture is present around the edges of the grain (red arrows).

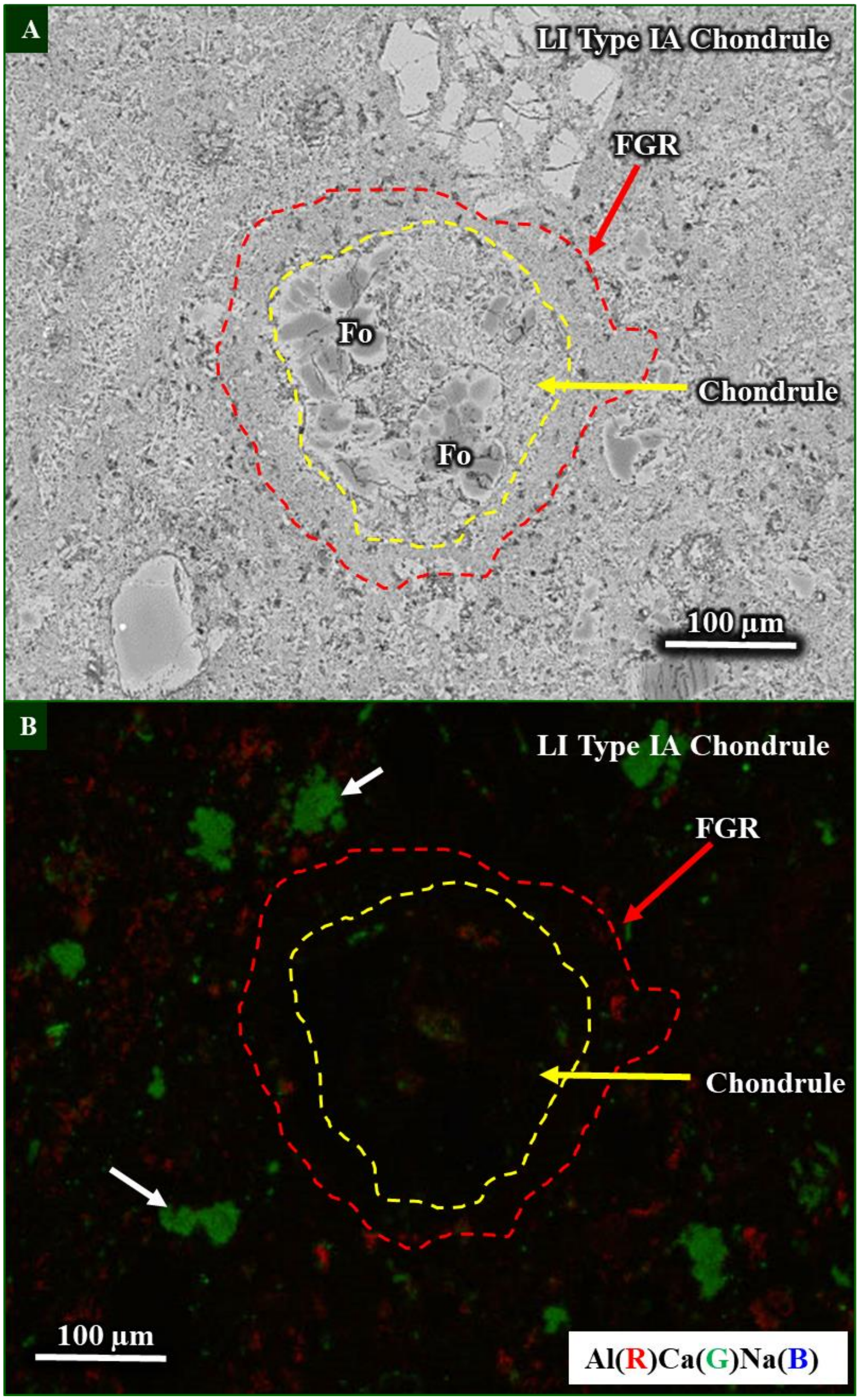

Figure 19: (A) BSE image of a porphyritic type IA chondrule (outlined in yellow) and its fine-grained rim (FGR-outlined). Some forsteritic phenocrysts remain (labeled "Fo"), but they have been extensively altered as has chondrule mesostasis. (B) X-ray map of the same chondrule (Al in red, Ca in green, and Na in blue). Ca-Fe-rich pyroxenes (white arrows) are present within the matrix. Original Na-bearing phases, such as mesostasis glass are completely absent within the chondrule. Small amounts of Ca and Al remain, however these phases most likely represent secondary phases.

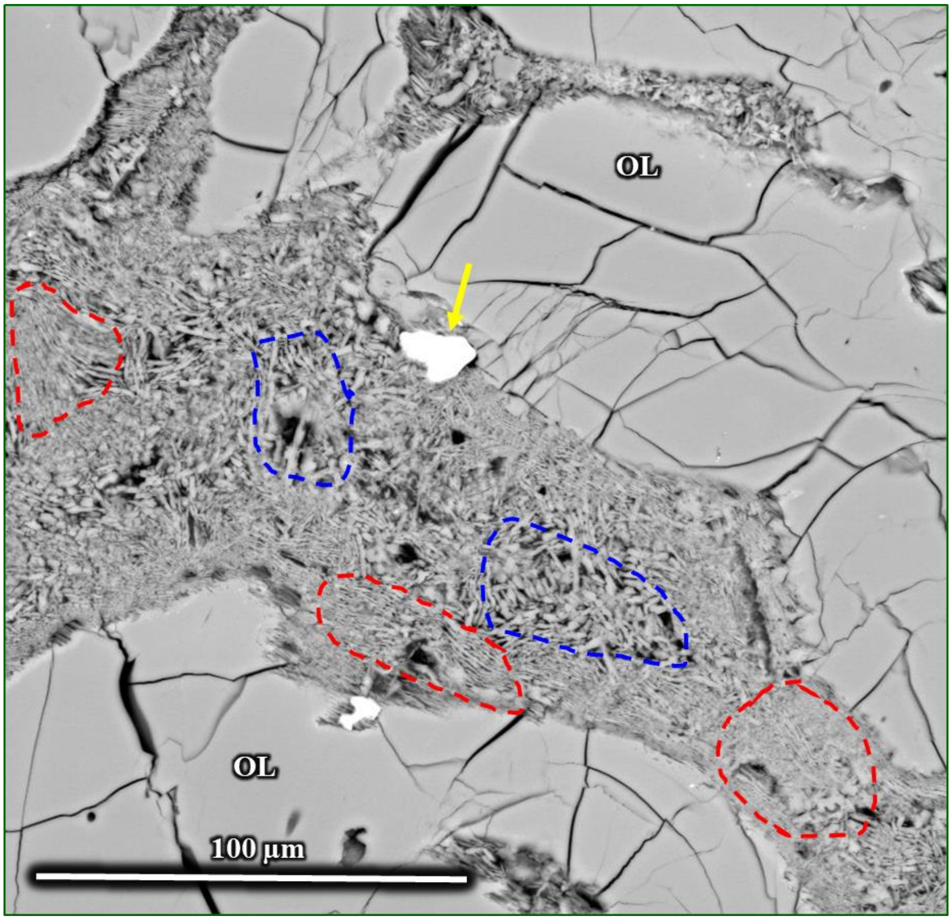

Figure 20: High magnification BSE image of the 11b inset showing an interior portion of the chondrule where the chondrule mesostasis has been very altered. This image contains both types of textural olivines that have replaced primary mesostasis material. The red outlined regions are examples of the elongate, ferroan olivines that are crystallographically oriented and tightly packed with submicron pore spaces between them. The blue outlined regions consist of texturally distinct anhedral or elongate ferroan olivine grains. These are varying in size, with much larger pore spaces in between them.

3.1.3.iii. Lithic Inclusion Matrix

The matrix of the LI is primarily composed of elongated, ferroan olivines, a few microns in length, similar to those in the matrix of the host chondrite. They are randomly oriented and there are tiny submicron to micron sized pores between the olivine grains. Compared to the host chondrite matrix, the LI matrix is finer-grained and more densely packed (Figure 21a-d). Aside from the abundance of elongate, ferroan olivines the matrix contains a higher abundance of Ca-rich phases as seen within the host.

X-ray elemental maps of the LI matrix shows that S, K, and Na bearing phases are either extremely rare or undetectable absent. The modal abundance of sulfides is approximately 0.01% and K and Na are completely absent. The LI matrix does have a slightly higher Al, Ca, and P abundance than the host matrix. The Al-bearing phases are heterogeneously distributed throughout the matrix and have a modal abundance of 9%. These Al-bearing phases are typically only a few microns to a few tens of microns in size. EBSD spectral analyses of these Al-bearing phases from an elemental X-ray map shows them to likely be hercynitic spinels, as observed for the host matrix (Figures 21b &22a-b). An EBSD spectral analyses indicates these small P-bearing phases are Ca phosphate grains, a few microns in size, with a modal abundance of 0.5% in the matrix.

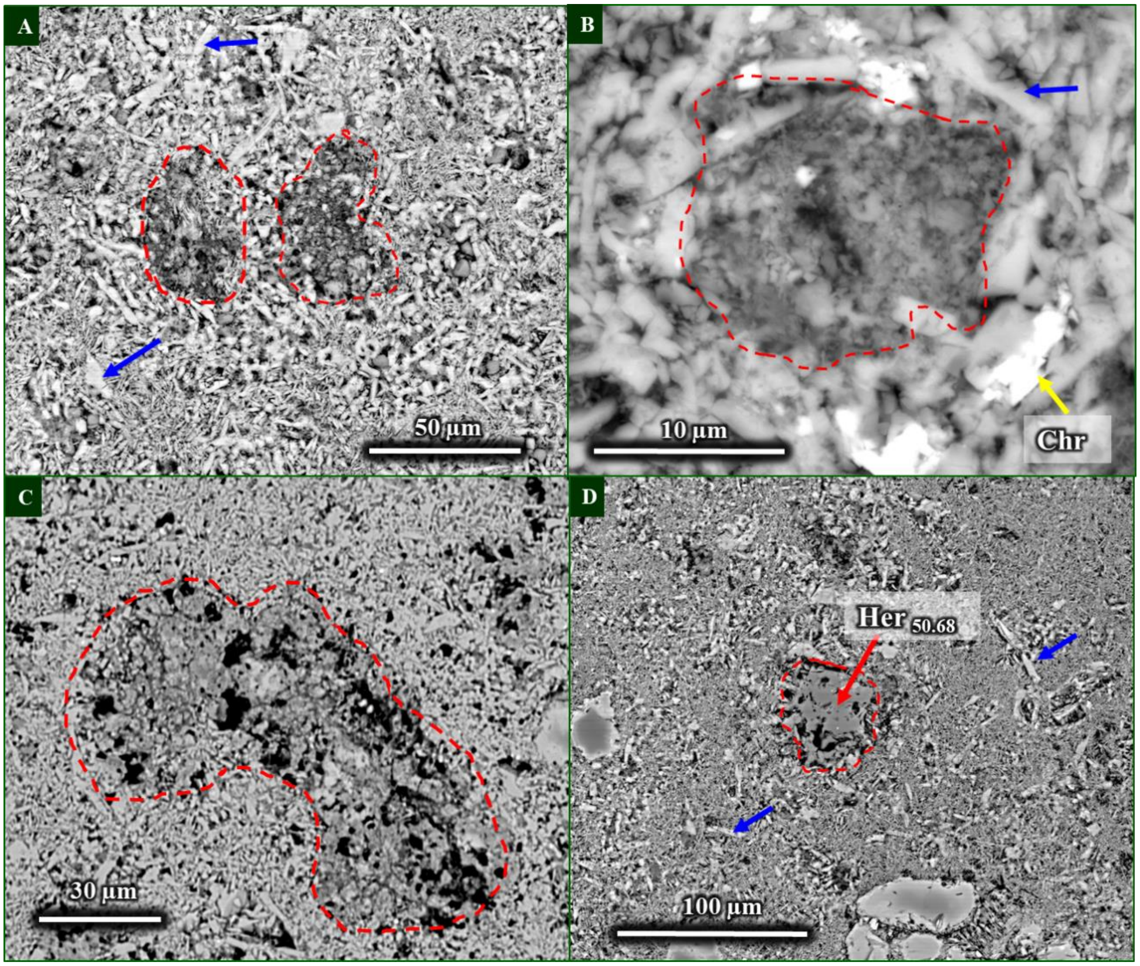

Figure 21: (A) BSE image of two porous Ca-rich pyroxene aggregates (outlined in red) embedded in the fine-grained matrix of the LI. The blue arrows indicate representative examples of elongate, ferroan olivine grains (Fa). (B) High magnification BSE image of a Ca-rich pyroxene aggregate (outlined in red). The yellow arrow indicates a chromite (Chr) grain in the matrix and the blue arrow indicates another example of an elongate, ferroan olivine grain. (C) BSE image of a larger Ca-rich pyroxene aggregate outline in red. (D) BSE image of a representative example of hercynite found in the matrix of the LI. Its composition was taken with a 1 µm beam size and is $Her_{50.68.}$ The blue arrows indicate examples of the ferroan, elongate olivine grains in the matrix.

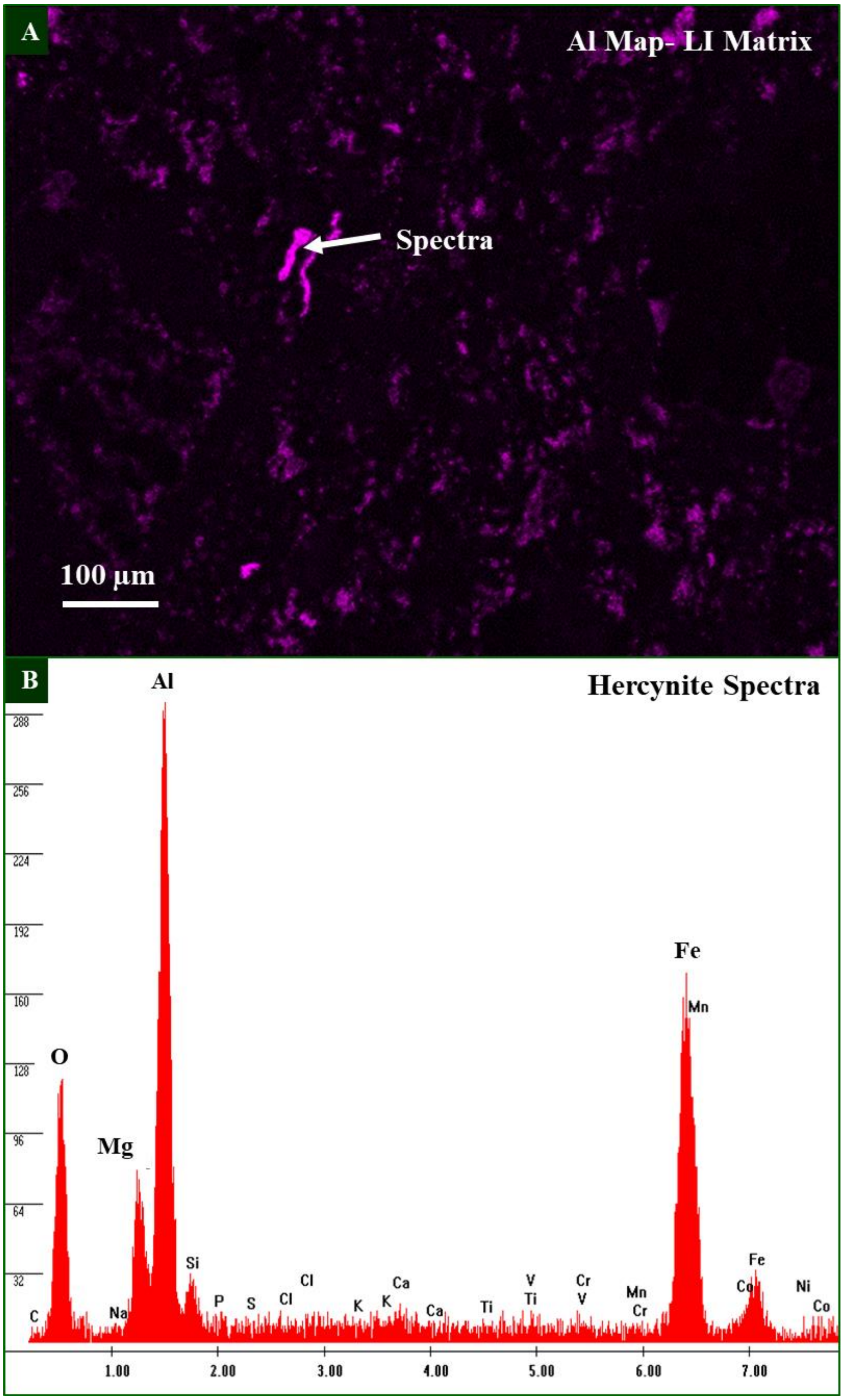

Figure 22: (A) Aluminum X ray map of a representative region within the matrix of the LI. The bright grain labeled "Spectrum" is where the EDS spectra was acquired from. (B) EDS spectrum of the Al-rich phase, hercynitic spinel.

Ca-rich aggregates

Elemental mapping and BSE imaging shows that Ca-rich phases are distributed throughout the matrix. High resolution SEM imaging of these Ca-rich phases showed that they form in aggregates of irregularly and rounded shapes that are highly porous (Figure 21a-c). The aggregates typically range in size from a few microns to around 50 microns. Qualitative EDS spectra show that the aggregates are dominated by Ca-Fe-rich pyroxenes. X-ray elemental mapping shows the modal abundance of these Ca-rich aggregates is ~13%; higher than the abundance in the host matrix. The Ca-rich pyroxene aggregates are very dominant within the central region of the LI and are less abundant or absent in a zone on the outer edge of the LI where it meets the host. Within the central region of the LI these Ca-rich pyroxenes surround chondrule fine-grained rims and chondrule pseudomorphs (Figs. 3 & 23a-b), but Ca-rich pyroxenes are absent within the chondrules themselves. A similar distribution has been observed in Allende dark inclusions (Krot et al., 2000).

Because of the fine-grained, porous nature of the aggregates, a FIB sample was prepared for TEM analysis from one aggregate to determine their textural relationships and compositions on a finer scale (Figure 24a). STEM EDS X-ray mapping shows that the only phase present is Ca-rich pyroxene. The Ca-rich pyroxene grains (less than a micron in size) occur in two distinct morphologies; fibrous, elongated grains and anhedral grains (Figure 24c & 25b). Texturally, both grain types have interlocking, irregular grain boundaries (Figure 25b). The TEM observations confirm that the aggregates are porous, but also reveal that both inter-granular and intra-granular porosity are present. The pore sizes for both types of porosity range in size from less than a micron to a few microns (Figure 24b & 25b). The edges of some of the Ca-rich pyroxene grains that are adjacent to pore spaces exhibit a distinct, saw tooth texture (Figure 24d & 25b). In general the “teeth” are approximately 0.1 μm or less in length and typically have an average periodicity of 0.1 μm.

STEM EDS X-ray mapping of a region of the Ca-rich pyroxene within the aggregate shows that there is considerable compositional heterogeneity over very small scales (Fig.25a, b). The compositional zoning is patchy on a submicron scale, even within the same grains. In some regions, the zoning is gradual, showing a progressive change from Mg-rich to Fe-rich compositions. In other regions however, there is a sharp discontinuity between the Mg-rich and Fe-rich compositions. As seen in composite, STEM EDS X-ray elemental map, the sharp grain boundaries that clearly define different grains correspond with the sharp discontinuities between the two compositions (Figure 25a, b). Quantitative EDS analyses of regions of the pyroxene, using EDS spectra extracted from the STEM-EDS map, show that the pyroxene varies from Fs_5 -Fs_{41} over distances of less than a micron in some cases.

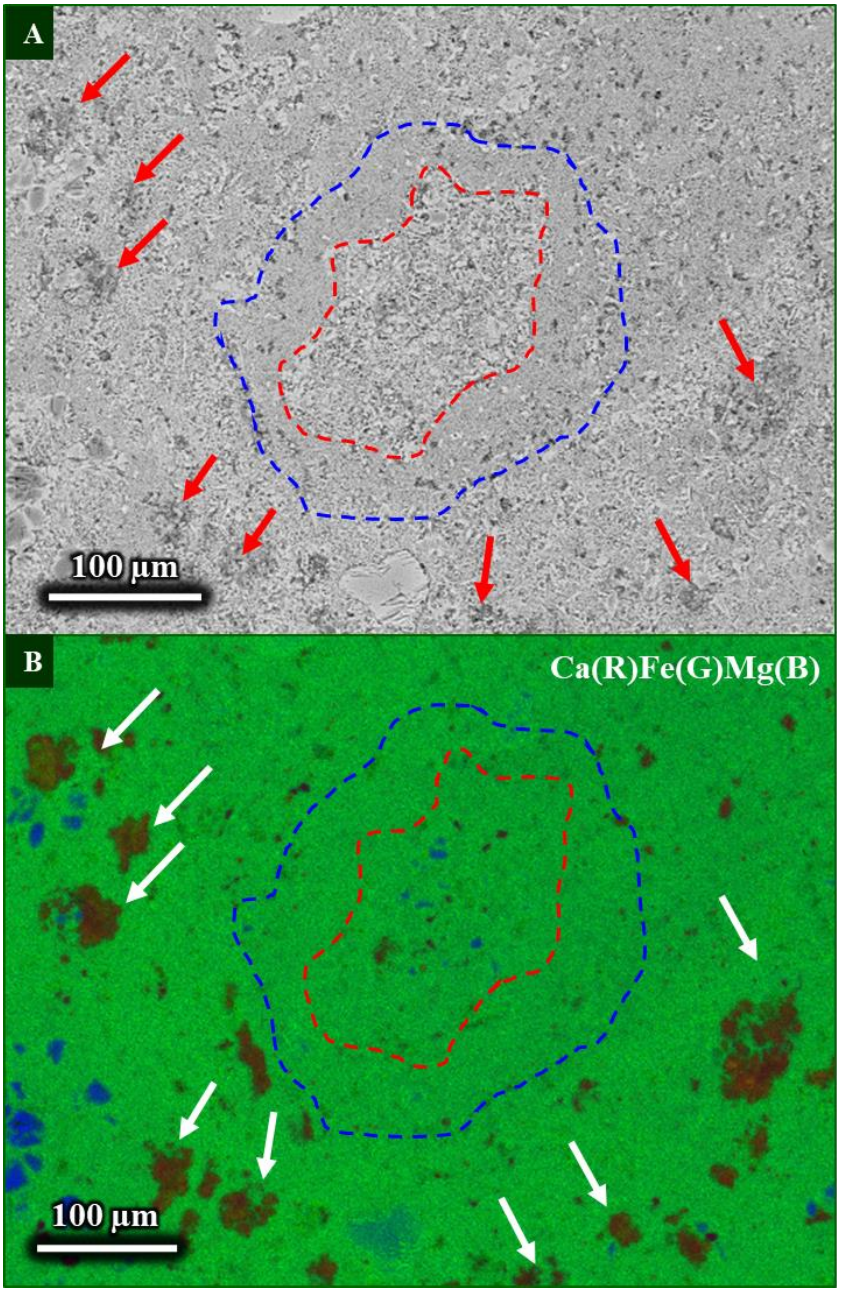

Figure 23: (A) BSE image of a chondrule pseudomorph in the LI outlined in red. The chondrule has been completely replaced by a porous aggregate of elongate, ferroan olivine. The fine-grained chondrule rim outlined in blue. The red arrows indicate the Ca-rich pyroxene aggregates that are distributed in the matrix. (B) Composite Ca(R)Fe(G)Mg(B) X-ray map of the same chondrule pseudomorph. The Ca-rich pyroxenes are indicated by the white arrows are partially surrounding the fine-grained chondrule rim, but are for the most part outside of the rim. There are also very few Mg- and Ca-rich phases remaining in the chondrule pseudomorph itself.

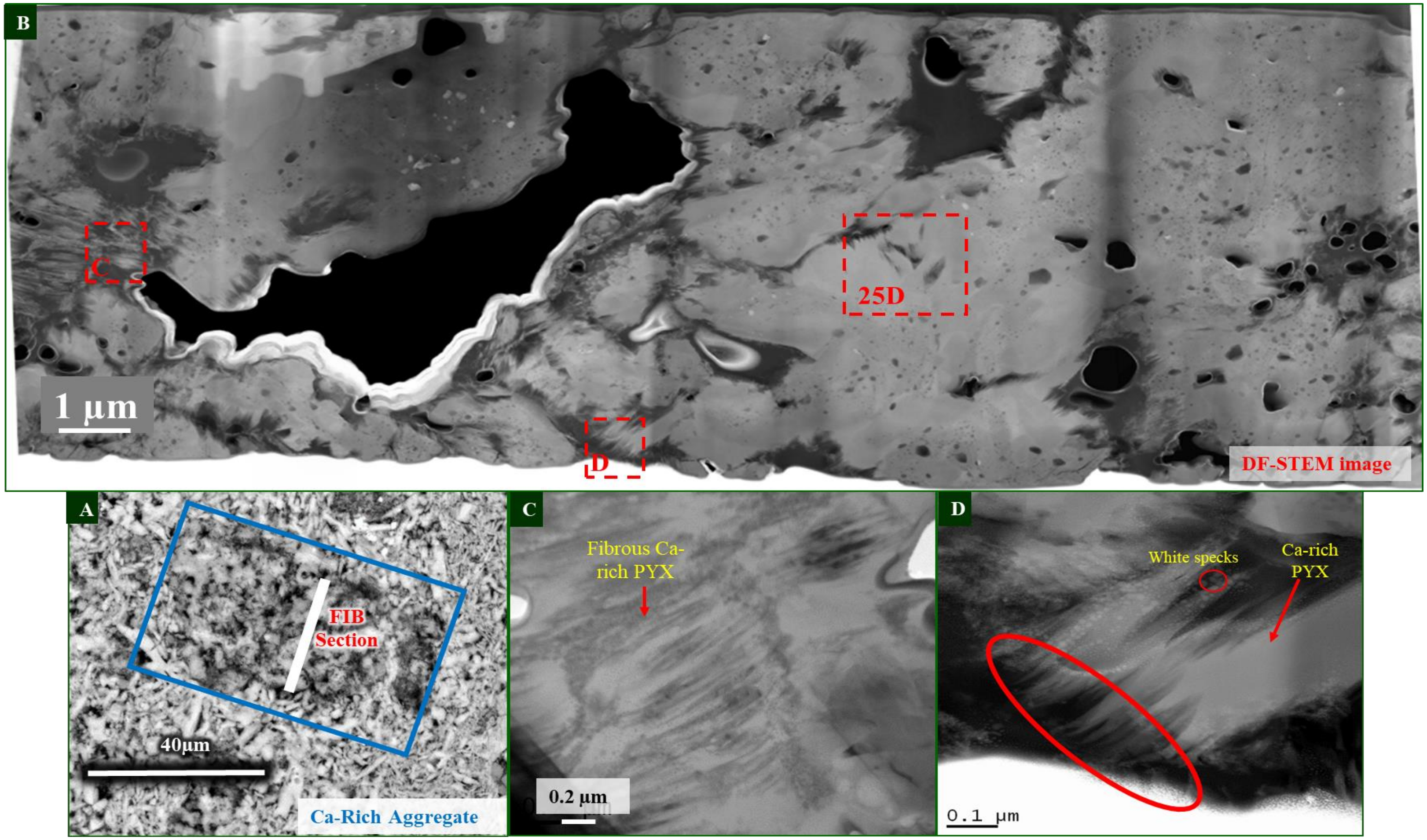

Figure 24: (A) Lower left -BSE image of the Ca-rich aggregate studied by TEM (e.g. white line shows where FIB section was cut). (B) High-angle Annular Dark-Field (HAADF) STEM image of the FIB section of the Ca-rich aggregates in the LI. (C) Bright-Field TEM image that shows one region of the fibrous, elongate Ca-rich pyroxenes consisting of subparallel fibers with porosity between the fibrous grains that is filled in with epoxy. (D) HAADF STEM image of the saw-tooth texture found throughout the FIB section at the edges of Ca-rich pyroxene grains (Ca-rich PYX). This texture occurs along the edge of the grain adjacent to void spaces. *The small, bright nanoparticles are likely redeposited material from ion sputtering during the FIB section cutting process (labeled White specks).

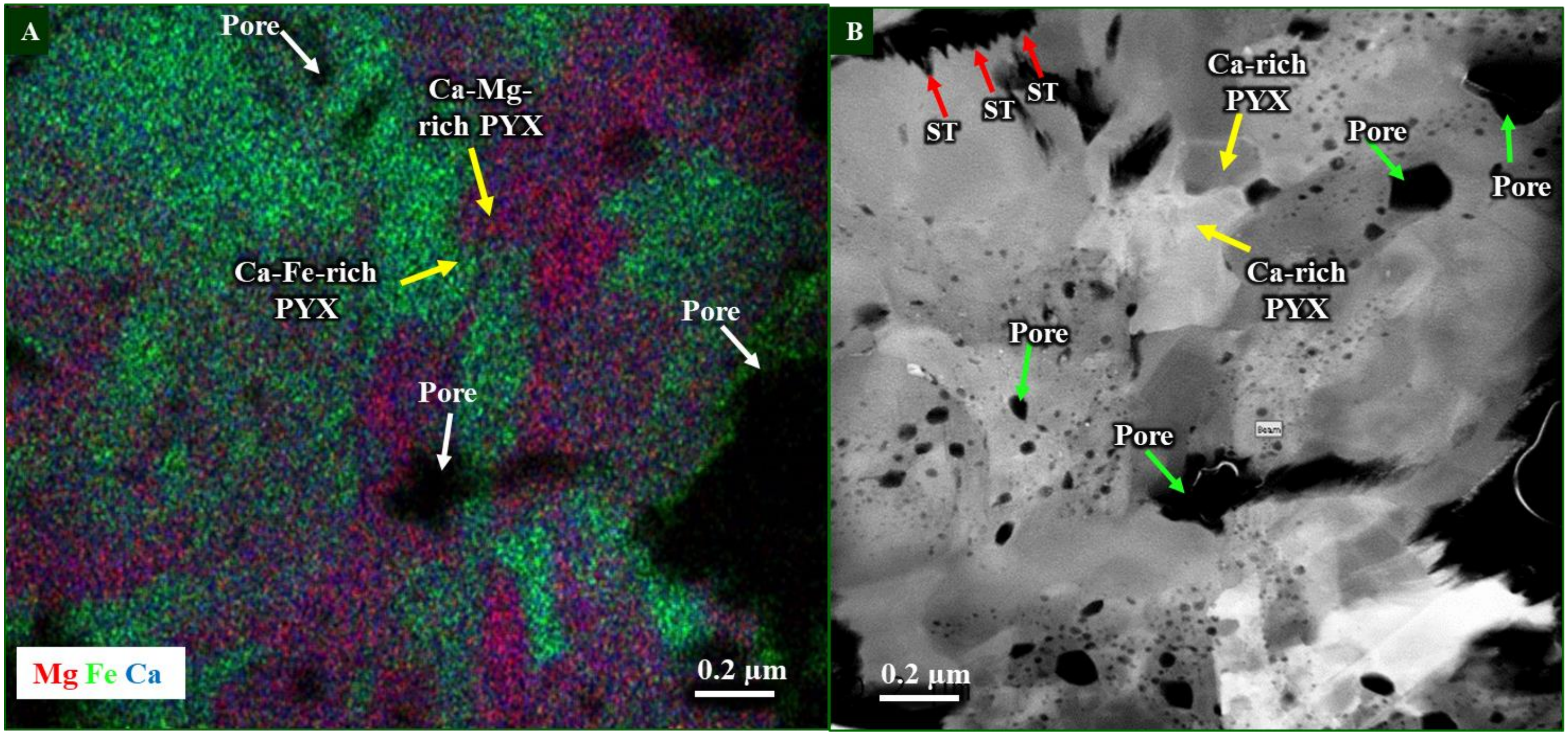

Figure 25: (A) Composite Mg(R)Fe(G)Ca(B) STEM EDS X-ray elemental map of the region seen in (B) The green regions are Ca-Fe-rich pyroxenes and the purple regions adjacent are the Ca-Mg-rich pyroxenes. (B) HAADF STEM image that shows heterogeneous porosity distributed within different grains (Pore – green arrows) in the sample, another example of the sawtooth texture observed (ST - red arrows), and Ca-rich pyroxene grains that are intergrown and anhedral. Compositional zoning in Fe content in the Ca-pyroxene (yellow arrows) is apparent and reflected by the varying brightness in the image at the submicron scale. Some of the anhedral pyroxene grains have very few pores, whereas other grains are highly porous. In some cases, the porosity is variable even within the same grain.

3.1.4. LI-Host interface

Between the host and the LI, there is a distinct, fine-grained rim around the periphery of the lithic inclusion that is heterogeneous in thickness, varying from a few tens of microns up to a few hundred microns. The rim is not sharp, but is gradational in character, but varies in the extent of that gradation in different regions of the rim (Figures 2, 3, and 26a). The LI has the shape of a deformed rectangle, the lower boundary is wavy in appearance (Figure 26a). Texturally, this rim is very fine-grained, compact, and has a low porosity. It and consists primarily of elongated, ferroan olivines and some isolated, irregularly-shaped olivine mineral fragments. These olivine grains are finer grained than those found within the LI, typically only a few microns in size.

X-ray maps of the rim show an enrichment in Ca-rich pyroxene aggregates defining the LI-Host interface, however from Figure 26a it is clear that the Ca-rich pyroxene aggregates are not continuous along the entire boundary and are missing in some sections, including the upper right of the LI and a small section on the lower left section. The behavior of the Ca-rich pyroxene aggregates from the interior of the inclusion towards the exterior region changes. There are zones of depletions of these Ca-rich pyroxene aggregates along the inside of the inclusion. This observation is similar to the behavior of Ca-rich rim seen in Allende dark inclusion, IV-I in the Krot et al. (2000) study, however in the dark inclusion, IV-I there were other Ca-rich minerals present within the rims, not just the Ca-rich pyroxenes as we observe here (Figure 26b).

This rim that defines the host and LI interface is rather complex. The Ca-rich pyroxenes are concentrated along the inner edge of the rim adjacent to the LI and form a densely packed, linear array. Within the rim itself, the distribution of Ca-rich phases is complex and is variable from one region to another. An example of a small region of the rim which exemplifies this complex behavior is shown in Figure 27. A zone, up to 300 microns in width, adjacent to the Ca-rich layer on the edge of the LI, is depleted in Ca-rich pyroxenes. However, the rim also contains linear arrays of Ca-rich phases and regions where the Ca-rich pyroxenes are more dispersed (Fig. 27).

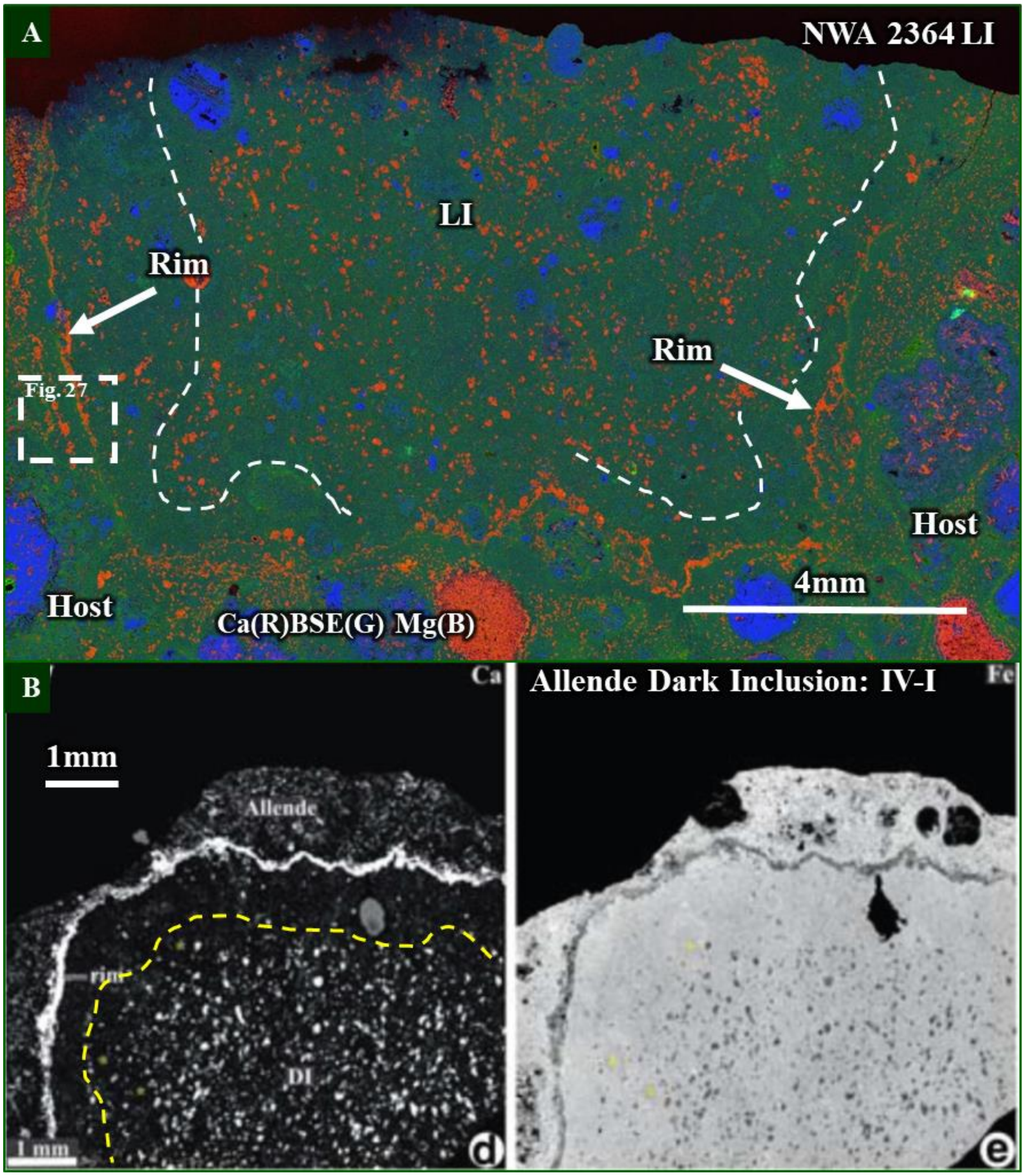

Figure 26: (A) A composite Ca(R)BSE(G)Mg(B) X-ray map of the lithic inclusion showing the Ca-rich pyroxene rim along the lithic inclusion and host interface. The rim is indicated by the white arrows (labeled Rim), the zone of depletion from the interior of the lithic inclusion to the rim is indicated by white-dashed lines. (B) X-ray elemental maps of Ca (left) and Fe (right) of the Allende dark inclusion, IV-I, from the Krot et al. (2000) study. The rim and Allende are labeled on the image. The zone of Ca depletion within the inclusion is indicated by the yellow dashed line.

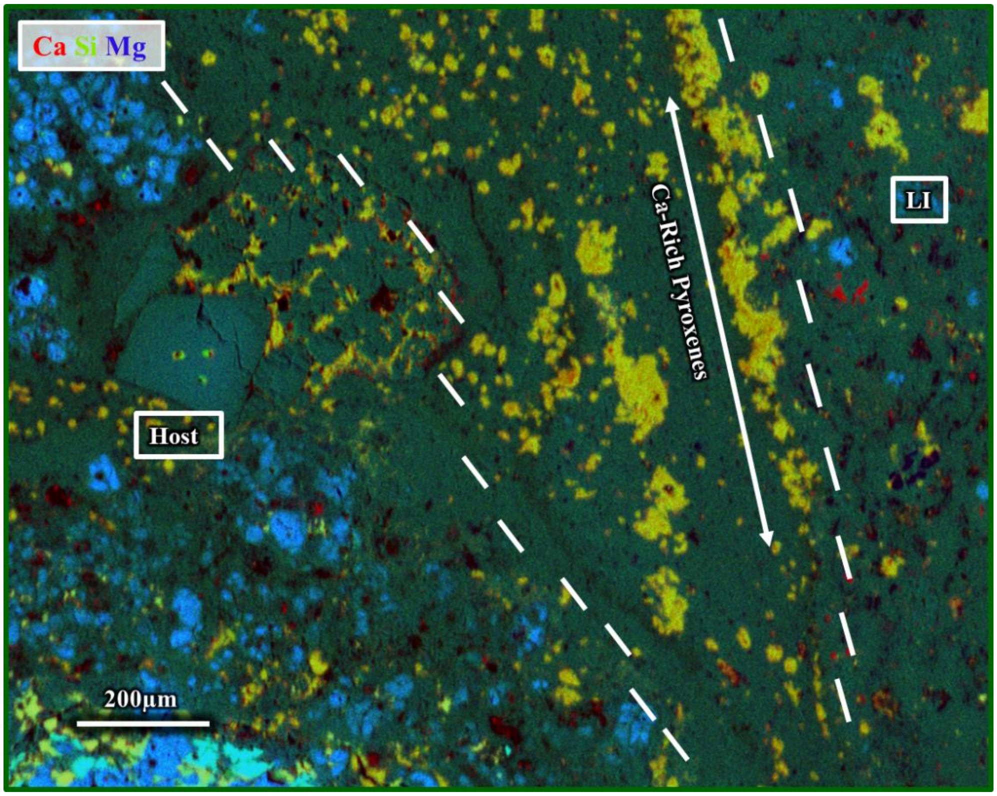

Figure 27: A composite Ca(R)Si(G)Mg(B) X-ray map of a section of the rim around the LI. There is concentration of Ca-Fe-rich pyroxenes that forms a linear array, highlighting the boundary between the host from the LI (e.g. white arrow for Ca-Fe-rich pyroxenes. Dashed lines for Host-LI distinction).

3.2. Mineral Chemistry

3.2.1. Host

3.2.1.i. Mineral chemistry of type I and type II chondrules: Olivine

As documented earlier, the host meteorite contains both type IA and type IIA chondrules. Within the host, the chondrules are predominately type IA and the olivine phenocrysts excluding the ferroan overgrowths range in composition from $Fa_{0.15}$-$Fa_{32.9}$ (representative analyses are reported in Table 2). The ferroan overgrowths of the type IA chondrule phenocrysts range in composition from $Fa_{33.93}$-$Fa_{45.46}$ (Table 3). Olivine phenocrysts in the rarer type IIA chondrules in the host meteorite range in composition from $Fa_{12.6}$-$Fa_{43.7}$ (Table 4). Unlike the type IIA chondrules in the LI, there are no observable ferroan overgrowths along the olivine phenocryst edges in the NWA 2364 host. Figures 28a-b show histograms of these different chondrule olivine phenocrysts with their respective ferroan overgrowths compared to one another.

Figure 29 shows the minor element relationships for compiled analyses of several type IA chondrule olivine phenocrysts excluding data for ferroan overgrowths. Representative ranges of the elements discussed here are summarized in Table 1. The data show a number of systematic relationships, despite some scatter in the data. For FeO vs MnO, there is a well-defined positive correlation from low MnO (<0.04 wt%) contents in the most forsteritic olivines, increasing progressively with FeO content to ~ 0.16 wt%. The opposite relationships are observed for Cr_2O_3, TiO_2, and CaO, although the behavior is somewhat more complex. The most forsteritic (<5 wt% FeO) compositions show a spread in Cr_2O_3 and TiO_2 contents, but with increasing FeO contents, both elements show a negative correlation, which starts at or close to the highest Cr_2O_3 and TiO_2 contents observed in the most forsteritic compositions. The CaO behavior has additional complexity; the most forsteritic olivines show a bimodal distribution with a high CaO group (0.3-0.56 wt%) and low CaO group (~0.05 wt%). Within the high CaO group there is a well-defined negative correlation with FeO content, which continues, albeit with considerable scatter, as the FeO content increases beyond Fo_5. With a few exceptions, olivines with FeO contents >5 wt% have CaO contents <0.3 wt%, i.e. consistently lower than the high CaO group of forsteritic olivines. This is consistent with observations from chondrules in other CV3 chondrites (Brearley and Jones, 1998).

The refractory elements, CaO, Al_2O_3, and TiO_2 are positively correlated, although the correlation is best defined for Al_2O_3 vs. TiO_2 (Figure 29). For CaO vs. Al_2O_3, there is no obvious correlation at low values of Al_2O_3 (<0.1 wt%), but a correlation appears above this value. There are a few analyses above 0.25 wt% Al_2O_3, which show no correlation with CaO. The Cr_2O_3 content also shows a slight positive correlation with Al_2O_3 content. In comparing the FeO and Al_2O_3 there appears to be two behaviors with increasing FeO content (Figure 30). At lower values of FeO (<5 wt%), the Al_2O_3 is heavily clustered at values (<0.2 wt%). As FeO increases, Al_2O_3 contents decrease and remain <0.2 wt% with the exception of one analysis that extends to approximately 0.5 wt%.

Table 1: Oxide weight percent ranges for type IA and IIA chondrule olivine phenocrysts in the LI and Host, type IA chondrule olivine phenocryst ferroan overgrowths in the LI type IA, LI type IIA, and host type IA, LI and host matrix, fine-grained chondrule rims in the LI, Mg-rich isolated olivine grains in the LI and Fe-rich isolated olivine grains in the LI.

LI Type IA Olivine Chondrule Phenocrysts-W/O Ferroan Overgrowths							**LI Type IA Olivine Chondrule Phenocrysts- Ferroan Overgrowths**						
	TiO_2	Al_2O_3	Cr_2O_3	FeO	MnO	CaO		TiO_2	Al_2O_3	Cr_2O_3	FeO	MnO	CaO
Maximum	0.103	0.465	0.366	27.387	0.241	0.689	Maximum	0.091	1.008	2.947	36.745	0.301	0.463
Minimum	b.d	b.d	0.013	0.344	0.001	0.081	Minimum	0.023	0.049	0.127	30.922	0.214	0.141
LI Type IIA Olivine Chondrule Phenocrysts-W/O Ferroan Overgrowths							**LI Type IIA Olivine Chondrule Phenocrysts- Ferroan Overgrowths**						
	TiO_2	Al_2O_3	Cr_2O_3	FeO	MnO	CaO		TiO_2	Al_2O_3	Cr_2O_3	FeO	MnO	CaO
Maximum	0.030	0.238	0.472	40.209	0.408	0.367	Maximum	0.056	1.048	0.294	35.177	0.264	0.251
Minimum	b.d	b.d	0.003	13.636	0.138	0.062	Minimum	0.041	0.465	0.227	34.560	0.242	0.222
LI Fine-grained Chondrule Rims							**LI Matrix**						
	TiO_2	Al_2O_3	Cr_2O_3	FeO	MnO	CaO		TiO_2	Al_2O_3	Cr_2O_3	FeO	MnO	CaO
Maximum	0.211	10.455	0.809	40.425	0.297	1.566	Maximum	0.251	9.983	1.982	41.965	0.344	2.696
Minimum	0.067	0.459	0.060	32.151	0.170	0.155	Minimum	0.009	0.270	0.013	31.651	0.157	0.094
LI Mg-rich Isolated Grains							**LI Fe-rich Isolated Grains**						
	TiO_2	Al_2O_3	Cr_2O_3	FeO	MnO	CaO		TiO_2	Al_2O_3	Cr_2O_3	FeO	MnO	CaO
Maximum	0.088	0.448	0.206	11.323	0.166	0.784	Maximum	0.024	0.054	0.155	39.365	0.421	0.351
Minimum	b.d	0.007	0.033	0.328	0.000	0.038	Minimum	b.d	0.013	0.029	14.548	0.163	0.068
Host Type IA Olivine Chondrule Phenocrysts-W/O Ferroan Overgrowths							**Host Type IA Olivine Chondrule Phenocrysts- Ferrroan Overgrowths**						
	TiO_2	Al_2O_3	Cr_2O_3	FeO	MnO	CaO		TiO_2	Al_2O_3	Cr_2O_3	FeO	MnO	CaO
Maximum	0.344	9.284	0.534	31.471	0.175	0.649	Maximum	0.167	5.441	1.340	38.060	0.248	0.303
Minimum	b.d	0.002	0.040	0.160	0.000	0.035	Minimum	b.d	0.050	0.092	21.240	0.132	0.074
Host Type IIA Olivine Chondrule Phenocrysts-W/O Ferroan Overgrowths							**Host Matrix**						
	TiO_2	Al_2O_3	Cr_2O_3	FeO	MnO	CaO		TiO_2	Al_2O_3	Cr_2O_3	FeO	MnO	CaO
Maximum	0.090	0.164	0.297	36.949	0.362	0.519	Maximum	0.210	3.872	1.423	44.957	0.314	0.588
Minimum	b.d	0.017	0.030	12.287	0.092	0.137	Minimum	b.d	0.018	0.033	34.452	0.144	0.093

Table 2: Representative electron microprobe analyses of host type IA chondrule olivine phenocrysts without ferroan overgrowths with formulae calculated on the basis of [4] oxygen atoms.

Oxide (wt%)

SiO_2	TiO_2	Al_2O_3	Cr_2O_3	FeO	MnO	MgO	CaO	Na_2O	K_2O	NiO	S	P_2O_5	TOTAL
41.70	0.04	0.09	0.11	7.28	0.09	51.34	0.21	0.01	0.01	0.05	0.01	0.02	100.96
41.72	0.05	0.11	0.12	7.19	0.09	51.36	0.28	0.01	b.d	0.04	0.01	b.d	100.98
41.53	0.06	0.12	0.17	8.16	0.09	50.41	0.29	0.02	0.01	0.00	b.d	b.d	100.86
38.91	0.02	0.02	0.05	23.03	0.16	37.66	0.19	0.01	b.d	0.05	0.01	b.d	100.11
39.09	b.d.	0.01	0.04	20.26	0.16	39.96	0.19	0.01	b.d	0.02	0.01	b.d	99.77
39.70	b.d	0.02	0.07	19.42	0.15	40.68	0.19	0.01	b.d	0.07	b.d	b.d	100.32
40.14	0.14	0.02	0.07	12.86	0.07	46.61	0.37	0.01	0.01	0.03	NA	NA	100.31
39.08	b.d	0.04	0.10	22.88	0.12	38.18	0.12	0.02	0.01	0.10	0.01	b.d	100.67
42.20	0.02	0.12	0.13	2.00	0.00	56.12	0.34	0.01	0.03	0.01	NA	NA	100.97
37.20	b.d	0.07	0.05	28.64	0.18	32.71	0.17	0.01	0.00	0.02	0.01	b.d	99.08

Number of cations per 4 Oxygen anions

Si	Ti	Al	Cr	Fe	Mn	Mg	Ca	Na	K	Ni	S	P	Sum	Fa (mol%)
1.000	0.001	0.002	0.002	0.146	0.002	1.835	0.005	0.001	b.d	0.001	b.d	b.d	2.996	7.37
1.000	0.001	0.003	0.002	0.144	0.002	1.835	0.007	0.001	b.d	0.001	b.d	b.d	2.996	7.28
1.001	0.001	0.004	0.003	0.164	0.002	1.811	0.008	0.001	b.d	b.d	b.d	b.d	2.995	8.32
1.012	b.d	b.d	0.001	0.501	0.004	1.461	0.005	b.d	b.d	0.001	b.d	b.d	2.986	25.54
1.007	b.d	b.d	0.001	0.437	0.003	1.535	0.005	0.001	b.d	b.d	0.001	b.d	2.991	22.15
1.013	b.d	0.001	0.001	0.414	0.003	1.547	0.005	0.001	b.d	0.001	b.d	b.d	2.987	21.12
0.995	0.003	b.d	0.001	0.267	0.001	1.723	0.010	0.001	0.001	b.d	NA	NA	3.002	13.40
1.010	b.d	0.001	0.002	0.494	0.003	1.471	0.003	0.001	0.002	b.d	b.d	b.d	2.988	25.16
0.990	b.d	0.003	0.002	0.039	0.000	1.963	0.008	b.d	b.d	0.001	NA	NA	3.008	1.96
1.007	b.d	0.002	0.001	0.649	0.004	1.320	0.005	b.d	b.d	b.d	0.001	b.d	2.990	32.94

[1]b.d., [2]NA

---

[1] below detection limit, [2] Not analyzed

Table 3: Representative electron microprobe analyses of host type IA olivine chondrule phenocryst ferroan overgrowths with formulae calculated on the basis of [4] oxygen atoms.

Oxide (wt%)

SiO_2	TiO_2	Al_2O_3	Cr_2O_3	FeO	MnO	MgO	CaO	Na_2O	K_2O	NiO	S	P_2O_5	TOTAL
34.20	0.04	1.77	1.11	36.40	0.22	24.99	0.22	0.25	0.01	0.04	0.01	0.57	99.84
36.71	0.02	0.10	0.34	32.32	0.16	29.81	0.07	0.03	0.01	0.05	0.01	0.02	99.66
37.52	0.01	0.05	0.09	29.56	0.15	32.29	0.12	0.03	0.01	0.05	b.d	0.01	99.89
36.28	0.16	0.32	0.37	35.08	0.21	27.16	0.17	0.02	b.d	0.07	0.01	0.05	99.92
35.81	0.08	0.29	0.18	38.06	0.25	25.61	0.13	0.02	0.01	0.03	0.01	0.02	100.51
35.38	0.04	0.47	0.88	37.13	0.21	25.74	0.17	0.05	0.01	0.02	0.01	0.10	100.21
36.71	b.d	0.07	0.11	32.29	0.19	30.24	0.07	0.08	0.01	0.00	NA	NA	99.78
35.84	b.d	0.02	0.04	31.47	0.17	30.58	0.15	b.d	0.06	0.00	NA	NA	98.35

Number of cations per 4 Oxygen anions

Si	Ti	Al	Cr	Fe	Mn	Mg	Ca	Na	K	Ni	S	P	Sum	Fa Mol%
0.959	0.001	0.058	0.025	0.854	0.005	1.045	0.007	0.013	b.d	0.001	0.001	0.014	2.984	44.96
1.007	b.d	0.003	0.007	0.741	0.004	1.219	0.002	0.001	b.d	0.001	b.d	b.d	2.987	37.82
1.011	b.d	0.002	0.002	0.666	0.004	1.297	0.003	0.002	b.d	0.001	b.d	b.d	2.988	33.93
1.006	0.003	0.011	0.008	0.814	0.005	1.123	0.005	0.001	b.d	0.001	b.d	0.001	2.979	42.01
1.002	0.002	0.010	0.004	0.891	0.006	1.068	0.004	0.001	b.d	0.001	b.d	0.001	2.989	45.46
0.991	0.001	0.015	0.019	0.870	0.005	1.075	0.005	0.003	b.d	b.d	b.d	0.002	2.988	44.72
1.005	b.d	0.002	0.002	0.739	0.004	1.234	0.002	0.004	b.d	b.d	NA	NA	2.995	37.46
1.00	b.d	b.d	b.d	0.73	b.d	1.27	b.d	b.d	b.d	b.d	NA	NA	3.000	36.60

Table 4: Representative electron microprobe analyses of host type IIA olivine chondrule phenocrysts without ferroan overgrowths with formulae calculated on the basis of [4] oxygen atoms.

Oxide (wt%)

SiO_2	TiO_2	Al_2O_3	Cr_2O_3	FeO	MnO	MgO	CaO	Na_2O	K_2O	NiO	S	P_2O_5	TOTAL
36.31	b.d.	0.03	0.06	33.72	0.28	29.02	0.18	0.02	b.d.	0.05	0.01	0.01	99.71
36.50	b.d.	0.03	0.04	33.30	0.27	29.56	0.18	0.02	b.d.	0.07	0.01	0.01	100.01
36.48	b.d.	0.02	0.03	32.82	0.28	29.73	0.16	0.02	b.d.	0.04	0.01	0.03	99.62
36.43	b.d.	0.03	0.06	32.51	0.28	29.93	0.14	0.03	b.d.	0.05	b.d.	0.06	99.53
36.67	b.d.	0.03	0.05	32.49	0.27	30.22	0.15	0.02	0.01	0.06	0.01	0.04	100.02
37.17	0.02	0.03	0.07	24.75	0.18	36.47	0.23	b.d.	0.01	0.01	NA	NA	98.94
35.63	b.d.	0.04	0.07	36.95	0.33	26.77	0.26	b.d.	0.01	0.05	NA	NA	100.10
35.79	b.d.	0.02	0.06	36.21	0.33	27.31	0.25	0.02	0.02	0.05	NA	NA	100.06
35.86	b.d.	0.04	0.06	35.85	0.36	27.90	0.25	0.01	0.01	0.02	NA	NA	100.37
35.87	b.d.	0.04	0.07	35.25	0.35	28.24	0.20	0.01	0.01	0.03	NA	NA	100.07

Number of cations per 4 Oxygen anions

Si	Ti	Al	Cr	Fe	Mn	Mg	Ca	Na	K	Ni	S	P	Sum	Fa (mol%)
1.003	b.d.	0.001	0.001	0.779	0.007	1.195	0.005	0.001	b.d.	0.001	b.d.	b.d.	2.995	39.46
1.003	b.d.	0.001	0.001	0.765	0.006	1.211	0.005	0.001	b.d.	0.002	0.001	b.d.	2.995	38.72
1.004	b.d.	0.001	0.001	0.755	0.007	1.220	0.005	0.001	b.d.	0.001	b.d.	0.001	2.994	38.24
1.002	b.d.	0.001	0.001	0.748	0.007	1.227	0.004	0.002	b.d.	0.001	b.d.	0.001	2.995	37.86
1.003	b.d.	0.001	0.001	0.743	0.006	1.232	0.004	0.001	b.d.	0.001	b.d.	0.001	2.995	37.62
0.991	b.d.	0.001	0.001	0.552	0.004	1.450	0.007	b.d.	b.d.	b.d.	NA	NA	3.007	27.58
0.998	b.d.	0.001	0.001	0.865	0.008	1.118	0.008	b.d.	b.d.	0.001	NA	NA	3.001	43.64
0.999	b.d.	0.001	0.001	0.845	0.008	1.136	0.007	0.001	0.001	0.001	NA	NA	3.001	42.65
0.996	b.d.	0.001	0.001	0.833	0.009	1.155	0.007	b.d.	b.d.	b.d.	NA	NA	3.003	41.89
0.996	b.d.	0.001	0.001	0.819	0.008	1.169	0.006	0.001	b.d.	0.001	NA	NA	3.003	41.19

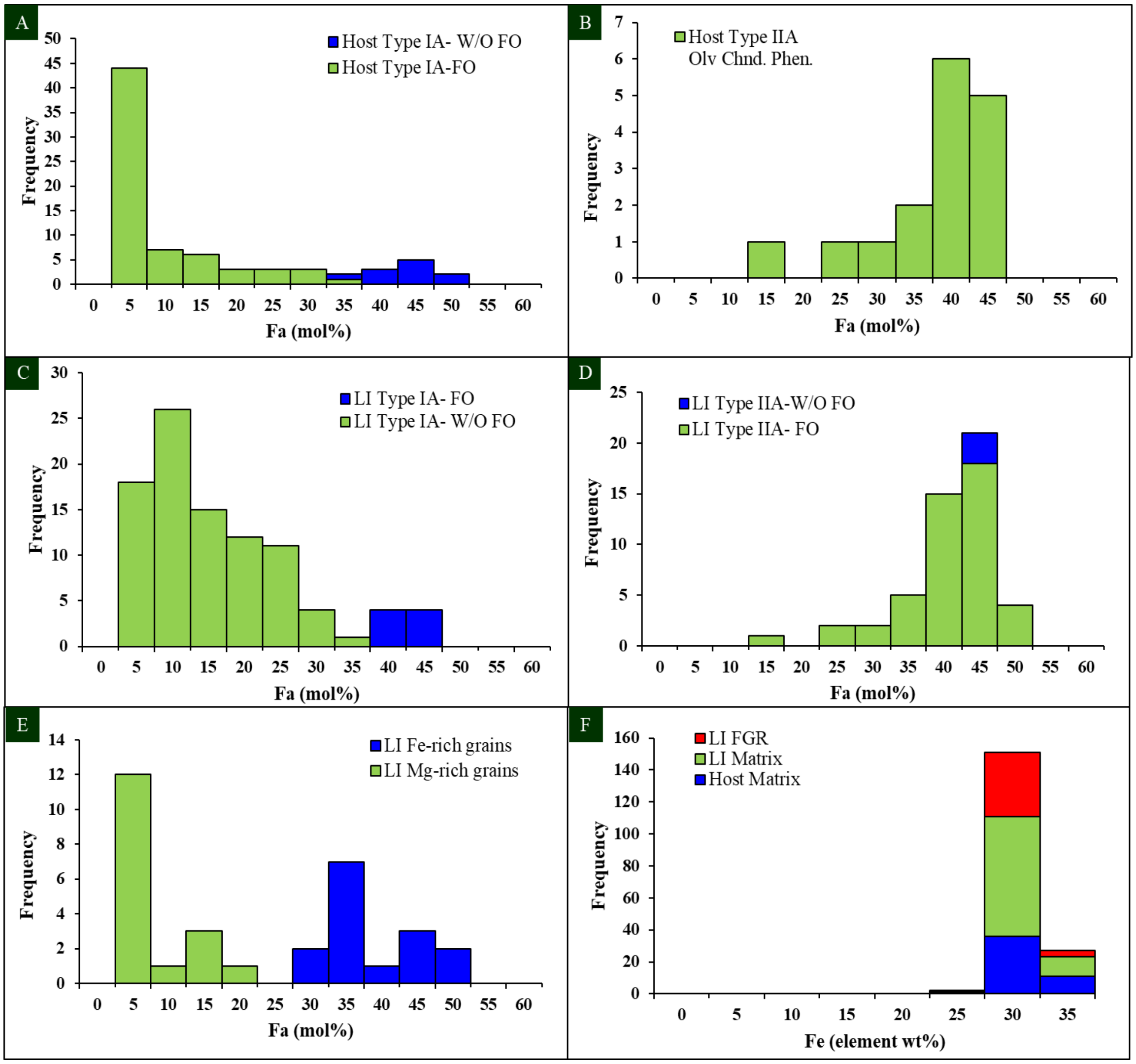

Figure 28: Histograms shown in (A)-(E) showing compiled olivine compositions (Fa mol%) obtained by electron microprobe (1µm beam size). (F) Compilation of broad beam electron microprobe analyses (50 µm beam size) of the fine-grained matrices of the LI, host, and the fine-grained chondrule rims for LI chondrules. (A) Host type IA chondrule olivine phenocrysts (green) and the host type IA chondrule olivine phenocryst ferroan overgrowths (blue). (B) Host type IIA chondrule olivine phenocrysts. (C) LI type IA chondrule olivine phenocrysts (green) and the LI type IA chondrule olivine phenocryst ferroan overgrowths (blue). (D) LI type IIA chondrule olivine phenocrysts (green) and the type IIA chondrule olivine phenocryst ferroan overgrowths (blue). (E) LI Fe-rich isolated olivine grains (green) and the LI Mg-rich isolated olivine grains (blue). (F) Histogram of bulk Fe contents (element wt%) for the host matrix material (blue), the LI matrix material (green), the LI fine-grained chondrule rim material (red).

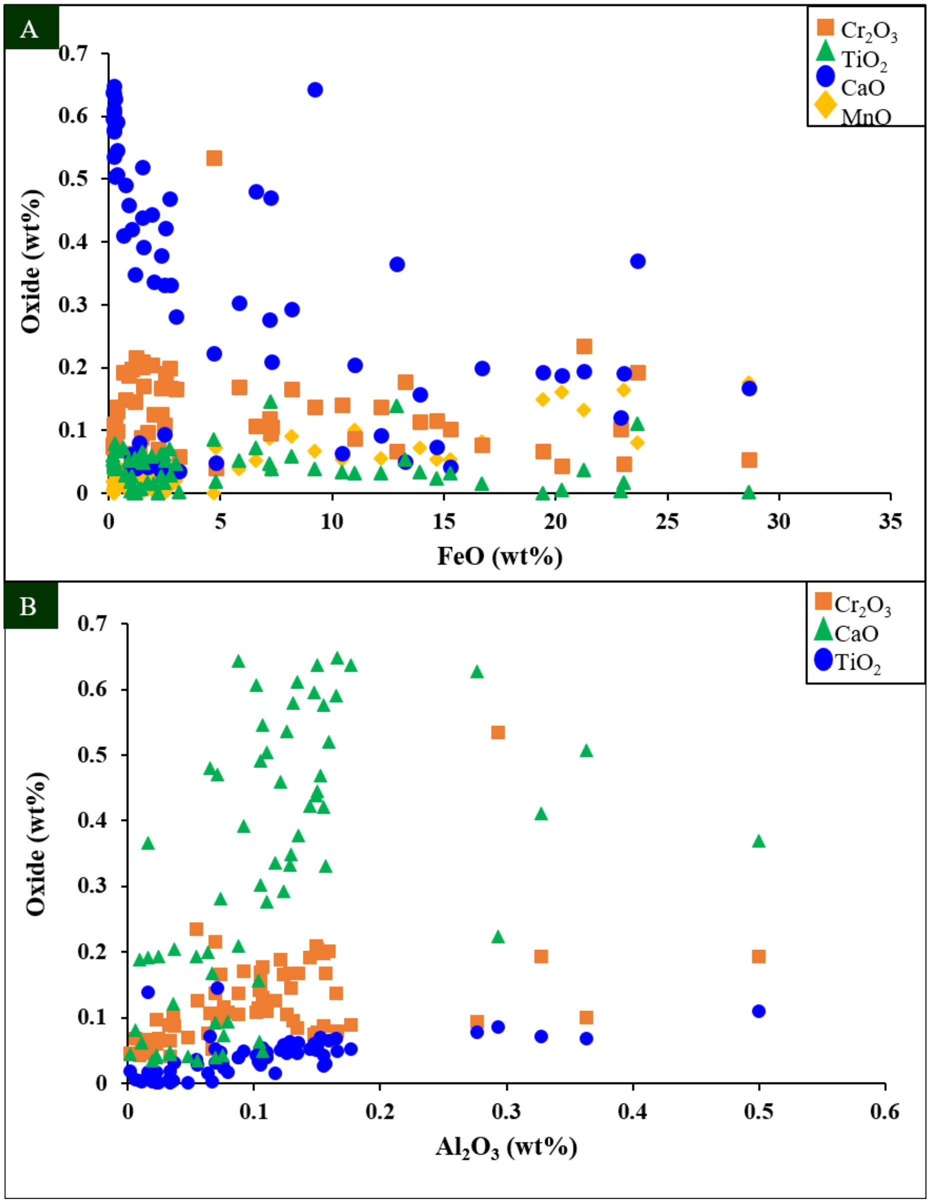

Figure 29: (A) Variation diagram of oxide contents (wt%) versus FeO contents (wt%) for a compilation of analyses of host type IA chondrule olivine phenocrysts. (B) A variation diagram of oxide contents (wt%) versus Al_2O_3 contents (wt%) for a compilation of analyses of host type IA chondrule olivine phenocrysts.

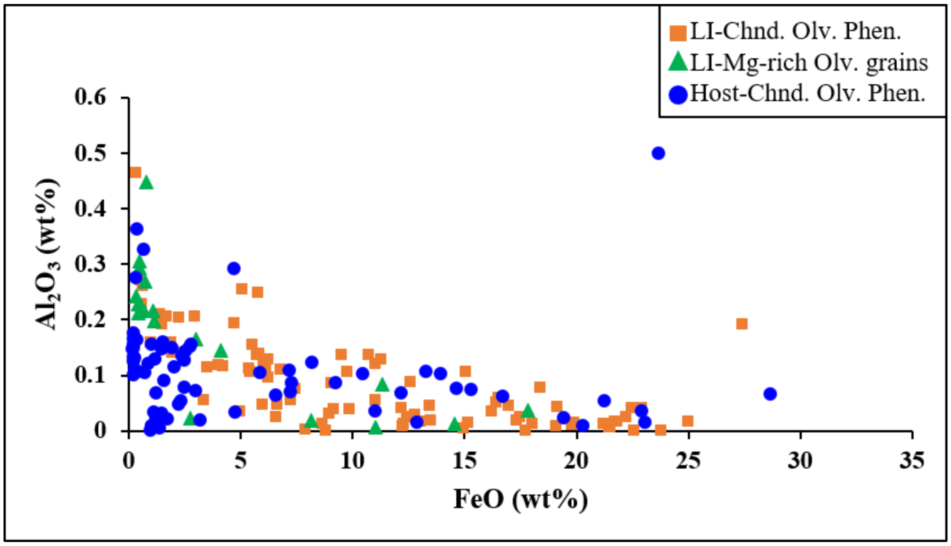

Figure 30: A variation diagram of Al_2O_3 contents (wt% oxide) versus FeO contents (oxide wt%) of a compilation of analyses from three different olivine-bearing objects in NWA 2364 and the LI.

Compositional data from the host type IA chondrule ferroan growths are plotted separately in Figure 31 and representative analyses and averages are reported in Table 3. Figure 30 shows the variation diagrams for some of the oxides compared against FeO and Al_2O_3 concentrations. As FeO increases, MnO shows a consistent increase, but for TiO_2 there is a general increase, but with significantly more scatter. The CaO content of the overgrowths shows no change with increasing Al_2O_3 content. However, for Al_2O_3 vs. Cr_2O_3, the data fall into two distinct groups. For Al_2O_3 contents <2 wt%, Cr_2O_3shows a strong positive correlation, but this correlation is lost at Al_2O_3 contents >4 wt%, although the data are very limited. It should be noted that in these ferroan overgrowths the high Al_2O_3 contents (greater than 1 wt%) are most likely not reflecting the behavior of these elements within the olivine crystal structure, but a mixing relationship with submicron inclusions within the ferroan overgrowths.

We also obtained a number of compositional zoning profiles by EPMA measured from the matrix material, through the ferroan overgrowth (if the chondrule type has them), into the interior of the chondrule phenocryst including the metamorphic diffusion zone within the phenocrysts. Figure 32a-d shows an example of one of these compositional zoning profiles for a host type IA chondrule olivine phenocryst. The only element that shows a systematic change in moving from the ferroan overgrowth rim into the phenocryst is the fayalite content, which decreases from Fa_{45} to Fa_{10}. The first 6 μm of the profile are within the fine-grained matrix material followed by 9 μm of a consistent composition through the ferroan overgrowth. Finally, the remaining profile points showing a decrease in the Fa content represent compositional zoning across the interface between the ferroan overgrowth and the interior of the phenocryst. The minor elements are characterized by spikes in concentration at different points along the profile, suggesting that there may be small inclusion phases within the excitation volume of the electron beam. For example, Ca has a correlated spike in concentration within the ferroan overgrowth, but then decreases moving into the chondrule phenocryst. Sulfur and Al also have a correlated spike in concentrations, but not until the interface between the ferroan overgrowth and t chondrule phenocryst. The Ni concentration roughly taper off moving inward, but towards the very end of the traverse, within the original chondrule phenocryst both spike in concentration at the same step. The Cr shows no systematic correlations.

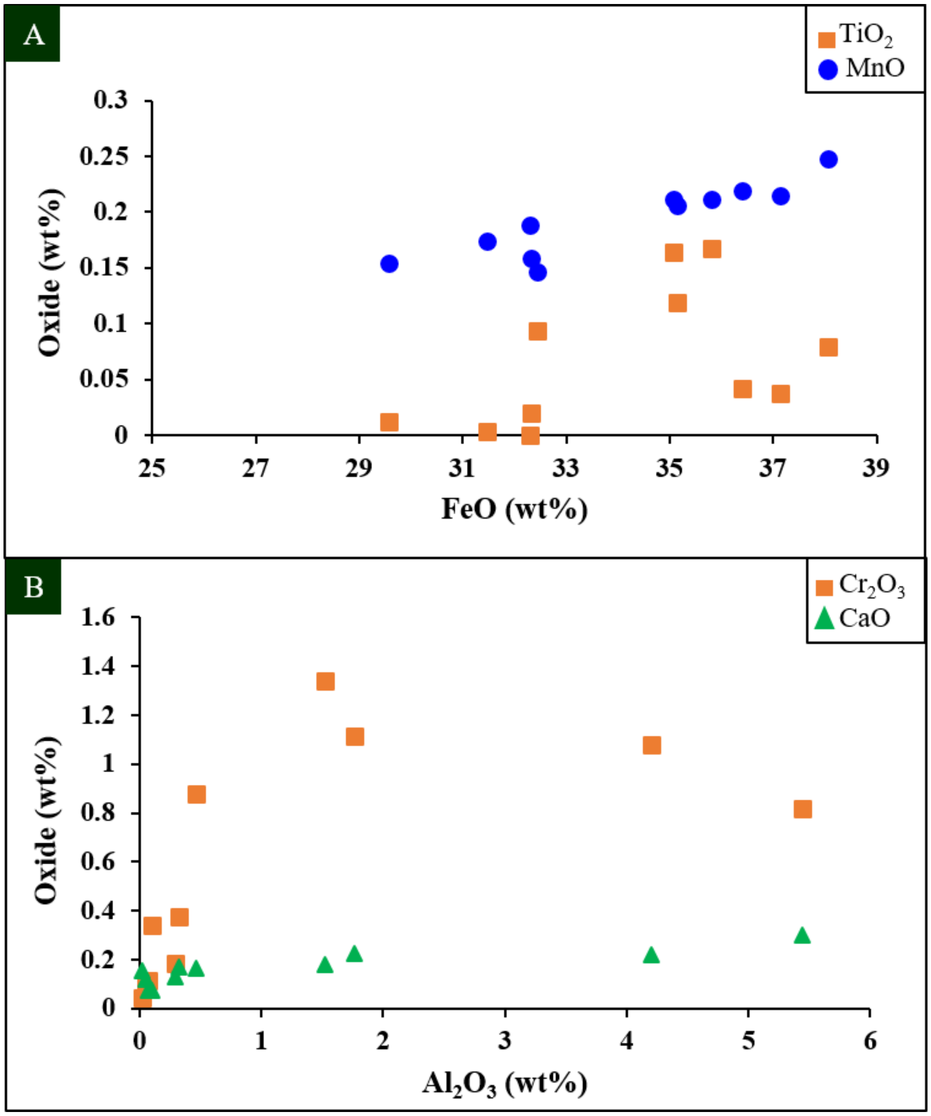

Figure 31: (A) A variation diagram of oxide contents (wt%) versus FeO contents (wt%) for a compilation of analyses of ferroan overgrowths in type IA host chondrule olivine phenocrysts. (B) The variation diagram of oxide contents (wt%) versus Al_2O_3 contents (wt%) for a compilation of analyses of ferroan overgrowths in type IA host chondrule olivine phenocrysts.

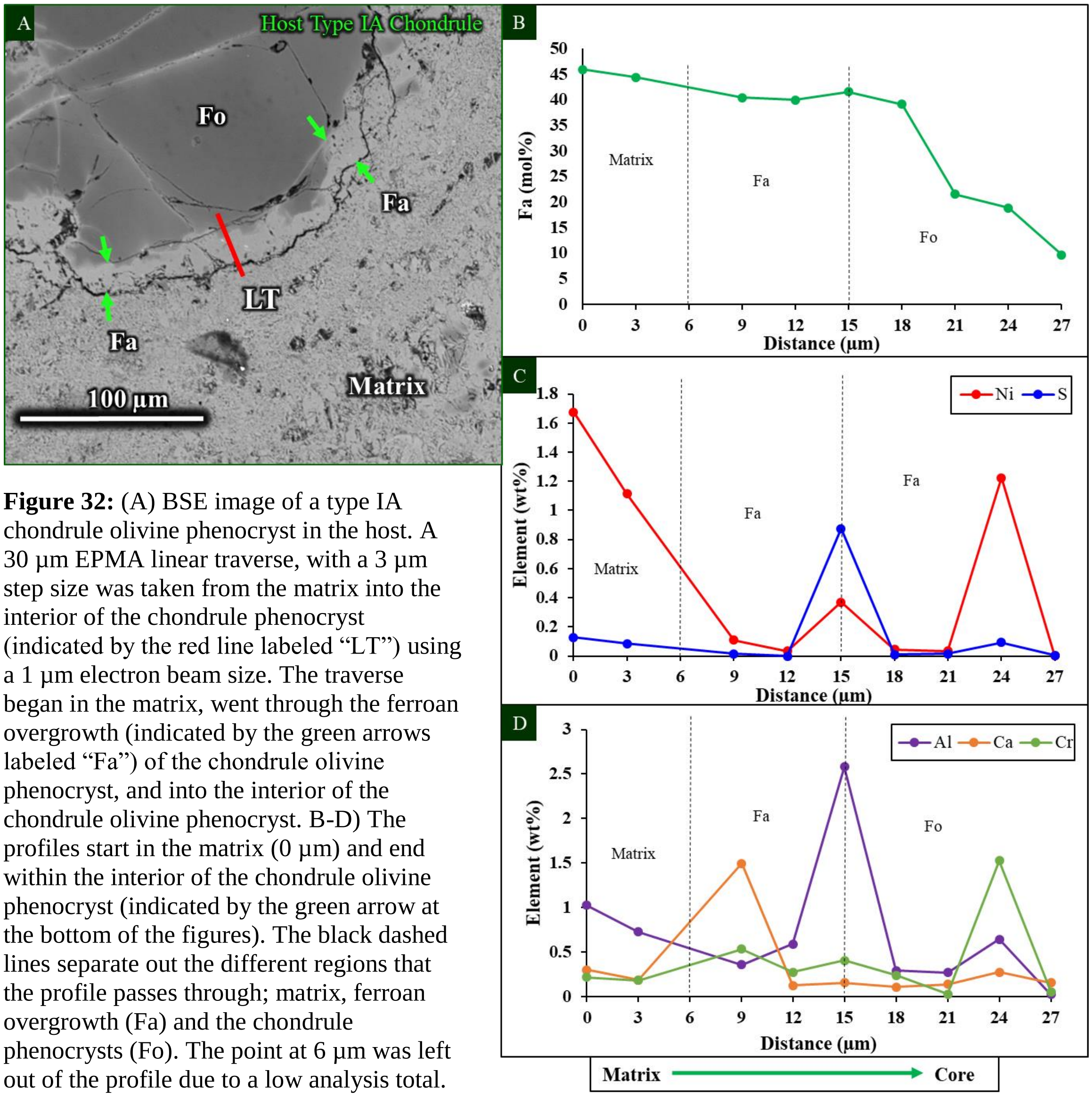

Figure 32: (A) BSE image of a type IA chondrule olivine phenocryst in the host. A 30 µm EPMA linear traverse, with a 3 µm step size was taken from the matrix into the interior of the chondrule phenocryst (indicated by the red line labeled "LT") using a 1 µm electron beam size. The traverse began in the matrix, went through the ferroan overgrowth (indicated by the green arrows labeled "Fa") of the chondrule olivine phenocryst, and into the interior of the chondrule olivine phenocryst. B-D) The profiles start in the matrix (0 µm) and end within the interior of the chondrule olivine phenocryst (indicated by the green arrow at the bottom of the figures). The black dashed lines separate out the different regions that the profile passes through; matrix, ferroan overgrowth (Fa) and the chondrule phenocrysts (Fo). The point at 6 µm was left out of the profile due to a low analysis total. (B) Fa (mol%) vs. distance in microns. (C) Ni and S (element wt%) vs. distance in microns. (D) Al, Cr, Ca (element wt%) vs. distance in microns.

The type IIA chondrule olivine phenocrysts within the host meteorite show a slightly different story. Figure 33 shows the changes in MnO, CaO TiO_2, versus FeO. The FeO content of the olivine shows a well-developed increase in concentration with MnO values as FeO increases beyond 10 wt%, consistent with igneous zoning patterns from fractional crystallization in chondrules (Jones, 1996). Lastly, the TiO_2 and CaO contents both exhibit a negative correlation with FeO content. The TiO_2 values show little variation, but above 25 wt% FeO show a decrease to below 0.1 wt%. The refractory element concentrations are consistently very low and show no apparent compositional (see Table 1) and are not discussed further.

Figures 34a-d show a compositional zoning profile taken of one of the type IIA chondrule olivine phenocrysts in the host meteorite. This profile was measured from the matrix material and into the phenocryst interior. The first 6 µm of the profile represents the fine-grained matrix material, with elevated Fa mol%, Al, Ca, Cr, Ni, and S. These elemental variations represent the mixing of phases within the matrix material. The remaining 24 µm of the profile is through the chondrule phenocryst and exhibits a decrease of approximately 5 mol% into the interior of the phenocryst. The S, Ni, Al, Ca, and Cr contents do not show any apparent zoning into the interior of the phenocryst.

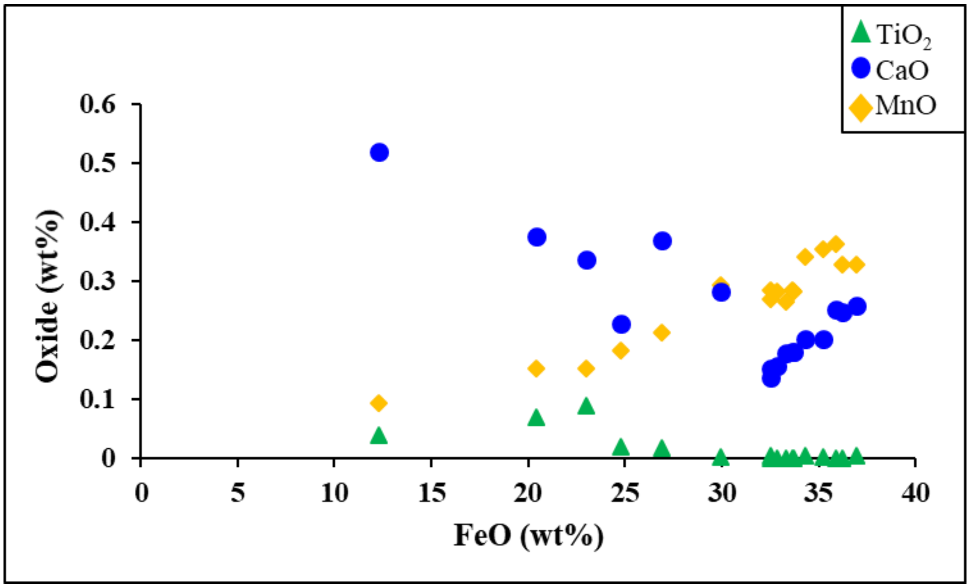

Figure 33: A variation diagram of oxide contents (wt%) versus FeO (wt%) of a compilation of analyses for the type IIA chondrule olivine phenocrysts in the host.

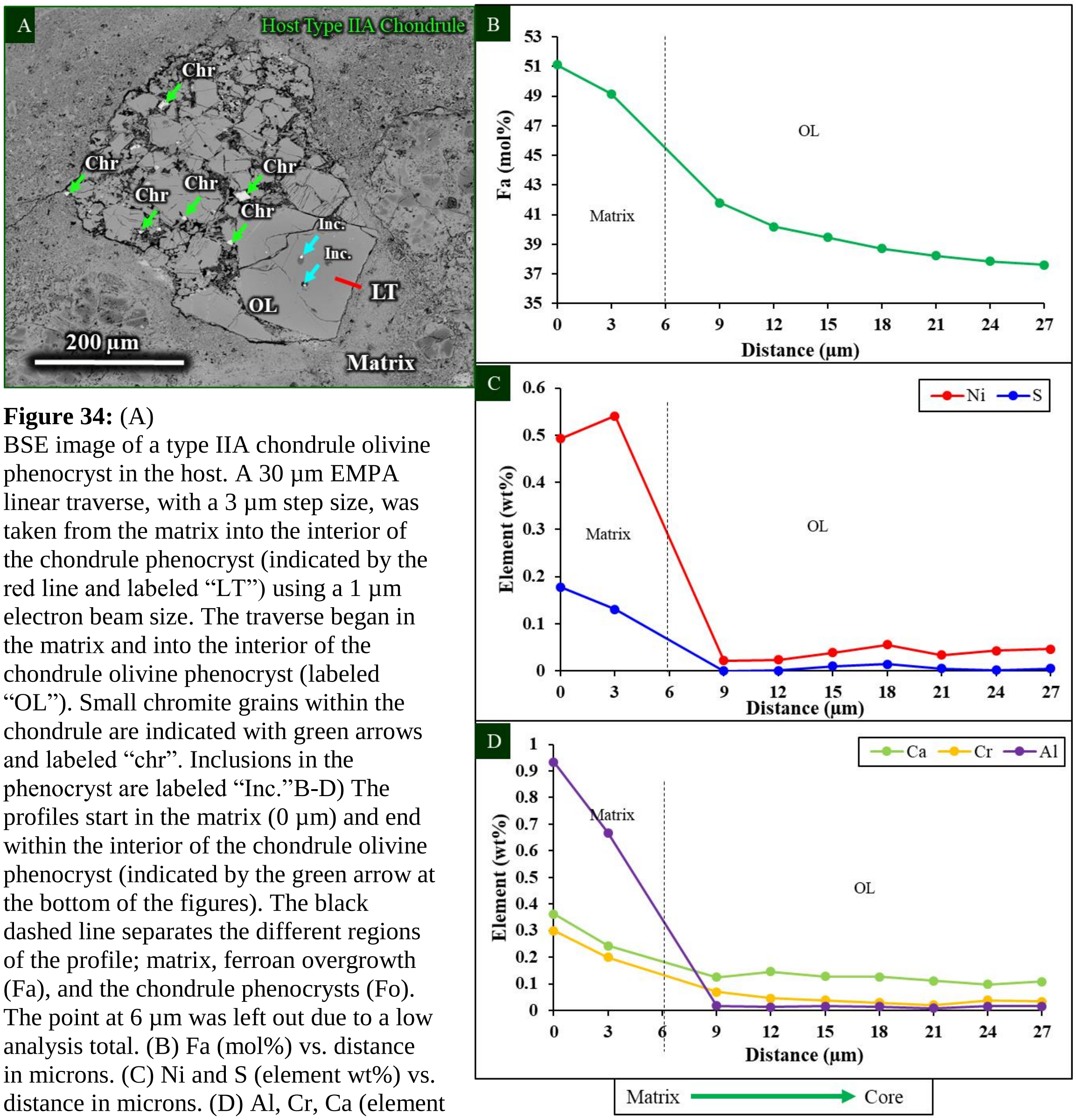

Figure 34: (A) BSE image of a type IIA chondrule olivine phenocryst in the host. A 30 µm EMPA linear traverse, with a 3 µm step size, was taken from the matrix into the interior of the chondrule phenocryst (indicated by the red line and labeled "LT") using a 1 µm electron beam size. The traverse began in the matrix and into the interior of the chondrule olivine phenocryst (labeled "OL"). Small chromite grains within the chondrule are indicated with green arrows and labeled "chr". Inclusions in the phenocryst are labeled "Inc."B-D) The profiles start in the matrix (0 µm) and end within the interior of the chondrule olivine phenocryst (indicated by the green arrow at the bottom of the figures). The black dashed line separates the different regions of the profile; matrix, ferroan overgrowth (Fa), and the chondrule phenocrysts (Fo). The point at 6 µm was left out due to a low analysis total. (B) Fa (mol%) vs. distance in microns. (C) Ni and S (element wt%) vs. distance in microns. (D) Al, Cr, Ca (element wt%) vs. distance in microns.

3.2.1.ii. Mineral Chemistry of Host chondrule minor phases

Anorthite (An_{84}) was found as a minor phase within one type IAB chondrule in the NWA 2364 host (Fig. 6). Table 5. The remaining phases found in this chondrule appear to be replacement products of anorthitic feldspar. These phases have Si+Al of approximately 4, based on 8 oxygens, but the rest of the cations are too low for a feldspar. At this point this phase is an unknown and needs additional work to fully characterize it. Representative analyses of this unknown alteration phase are listed in Table 6. Enstatite with a composition $En_{97.6}$ occurs in the same chondrule and is reported in Table 7.

Augite was another minor phase found in at least one type IAB chondrule in the host. The two electron microprobe analyses (taken with a 1 µm beam size) for this pyroxene are reported in Table 7. The relationships and compositions of the two different pyroxenes found in the host chondrules have been plotted on the ternary diagram in Figure 35.

Table 5: Electron microprobe analysis of anorthite in an NWA 2364 host type IAB chondrule with formulae calculated on the basis of [8] oxygen atoms.

						Oxide (wt%)								
SiO_2	TiO_2	Al_2O_3	Cr_2O_3	FeO	MnO	MgO	CaO	Na_2O	K_2O	NiO	S	P_2O_5	TOTAL	
45.16	0.10	33.75	0.02	1.05	0.01	0.64	15.97	1.58	0.04	b.d.	0.02	0.02	98.36	
						Number of cations per 8 Oxygen anions								
Si	Ti	Al	Cr	Fe	Mn	Mg	Ca	Na	K	Ni	S	P	Sum	An (mol%)
2.115	0.003	1.863	0.001	0.041	0.000	0.045	0.802	0.143	0.002	b.d.	0.002	0.001	5.018	84.63

Table 6: Electron microprobe analyses of unknown alteration phase within host chondrule.

						Oxide (wt%)							
SiO_2	TiO_2	Al_2O_3	Cr_2O_3	FeO	MnO	MgO	CaO	Na_2O	K_2O	NiO	S	P_2O_5	TOTAL
37.88	0.19	27.55	0.04	3.36	0.01	1.97	6.42	0.41	0.36	0.44	0.27	0.27	79.17
45.82	0.12	32.90	0.05	1.73	b.d.	1.00	8.95	0.98	0.40	0.24	0.23	0.18	92.61
33.86	0.19	25.77	0.03	3.18	b.d.	1.48	2.27	0.31	0.39	0.62	0.82	0.27	69.19
46.32	0.11	28.20	0.16	2.77	b.d.	1.85	4.56	0.39	0.60	0.41	0.43	0.41	86.21
						Number of cations per 8 Oxygen anions							
Si	Ti	Al	Cr	Fe	Mn	Mg	Ca	Na	K	Ni	S	P	Sum
2.157	0.008	1.849	0.002	0.160	b.d.	0.168	0.392	0.045	0.026	0.020	0.029	0.013	4.868
2.212	0.004	1.873	0.002	0.070	b.d.	0.072	0.463	0.092	0.025	0.010	0.021	0.007	4.851
2.131	0.009	1.912	0.002	0.168	b.d.	0.139	0.153	0.038	0.031	0.031	0.097	0.014	4.723
2.358	0.004	1.692	0.006	0.118	b.d.	0.141	0.249	0.038	0.039	0.017	0.041	0.018	4.720

Table 7: Representative electron microprobe analyses of pyroxene compositions in host chondrule phenocrysts with formulae calculated on the basis of [6] oxygen atoms. Shaded regions represent analyses from the same chondrule within the host.

	Oxide (wt%)							
SiO_2	55.89	51.36	51.64	58.53	58.22	56.37	52.43	53.81
TiO_2	0.93	1.04	0.83	0.34	0.33	0.40	1.03	0.80
Al_2O_3	6.96	8.73	7.63	1.58	1.76	2.61	5.83	4.56
Cr_2O_3	0.61	0.99	0.98	0.82	0.94	1.03	1.22	1.01
FeO	0.62	0.34	0.55	0.65	1.58	0.95	0.55	0.86
MnO	0.08	0.25	0.20	0.10	0.18	0.22	0.26	0.24
MgO	36.06	19.18	20.96	36.58	35.03	31.17	21.44	23.07
CaO	0.67	20.43	19.14	3.03	4.14	6.35	18.24	16.24
Na_2O	0.01	0.04	0.06	0.01	0.01	0.02	0.02	0.04
K_2O	0.01	0.01	0.00	0.00	0.02	0.00	0.02	0.00
NiO	0.02	0.04	0.00	0.00	0.00	0.02	0.01	0.02
S	0.02	N/A	N/A	N/A	N/A	N/A	N/A	N/A
P_2O_5	0.00	N/A	N/A	N/A	N/A	N/A	N/A	N/A
TOTAL	101.86	102.40	102.00	101.64	102.20	99.14	101.05	100.65

	Cations per 6 Oxygens							
Si	1.849	1.792	1.805	1.954	1.948	1.950	1.846	1.890
Ti	0.023	0.027	0.022	0.009	0.008	0.010	0.027	0.021
Al	0.272	0.359	0.314	0.062	0.069	0.106	0.242	0.189
Cr	0.016	0.027	0.027	0.022	0.025	0.028	0.034	0.028
Fe	0.017	0.010	0.016	0.018	0.044	0.028	0.016	0.025
Mn	0.002	0.007	0.006	0.003	0.005	0.006	0.008	0.007
Mg	1.779	0.998	1.093	1.820	1.748	1.607	1.126	1.208
Ca	0.024	0.764	0.717	0.108	0.148	0.235	0.688	0.611
Na	0.000	0.003	0.004	0.001	0.000	0.001	0.001	0.003
K	0.000	0.001	0.000	0.000	0.000	0.000	0.001	0.000
Ni	0.001	0.001	0.000	0.000	0.000	0.001	0.001	0.001
S	0.001	N/A	N/A	N/A	N/A	N/A	N/A	N/A
P	0.000	N/A	N/A	N/A	N/A	N/A	N/A	N/A
Sum	3.983	3.989	4.004	3.996	3.997	3.974	3.989	3.983

	Cation ratios Mg:Fe:Ca							
En	97.77	56.317	59.838	93.503	90.075	85.950	61.513	65.501
Fs	0.94	0.556	0.888	0.925	2.283	1.473	0.878	1.375
Ca	1.34	43.128	39.273	5.572	7.642	12.578	37.609	33.124

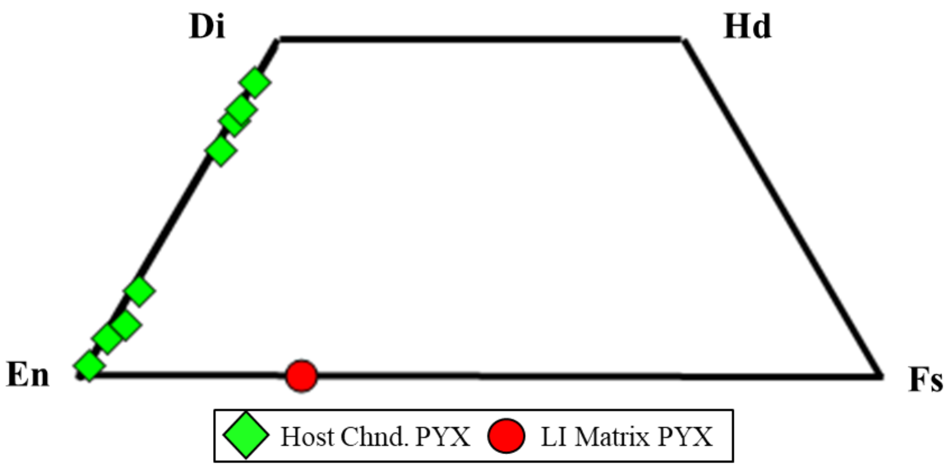

Figure 35: Pyroxene quadrilateral showing pyroxene compositions in the host and LI (mol%). The host pyroxenes that were analyzed are from chondrule phenocrysts. These analyses were taken with a 1 µm beam size. The one analysis for the LI came from an isolated pyroxene grain in the matrix. This analysis was obtained using a 50 µm beam size.

3.2.1.iii. Host matrix Compositions

Here we describe the compositional characteristics of the matrix material from the host (see Table 8). The matrix consists primarily of fine-grained ferroan olivines with a few additional minor phases (hercynitic spinels and Ca-rich pyroxenes, see petrography section) present. Broad beam analyses (50 μm beam diameter) of the bulk composition were obtained from the matrix material. Figure 36 shows minor element variation diagrams for several oxides relative to FeO and Al_2O_3. The minor element concentrations show significant variability (0-0.21 wt% TiO_2; 0.09-0.59 wt% CaO; 0.14-0.31 wt% MnO; 0.03- 1.42 wt% Cr_2O_3; 0.02-3.87 wt%). There are no apparent correlations for any of these elements with FeO content, but there appears to be two groups of data for these oxides at different FeO wt% values. The first group clusters between 34 wt% and 39 wt% FeO. The second starts at FeO values > 40 wt% and extends to 46 wt% FeO. Al_2O_3 does show well-defined positive correlations with Cr_2O_3, TiO_2, and CaO contents as it increases up to 2 wt%.

Table 8: Compilation of EPMA analyses of representative bulk analyses of the fine-grained matrix material for the host. Analyses taken with a 50 µm beam size.

Oxide (wt%)													
SiO_2	TiO_2	Al_2O_3	Cr_2O_3	FeO	MnO	MgO	CaO	Na_2O	K_2O	NiO	S	P_2O_5	TOTAL
32.59	0.08	0.67	0.22	36.30	0.25	26.44	0.24	0.07	0.01	0.30	0.22	0.08	97.80
28.29	0.13	1.08	0.50	34.45	0.21	15.83	0.42	0.11	0.03	0.78	0.19	0.21	82.52
34.97	0.08	0.49	0.26	36.94	0.23	24.54	0.26	0.04	0.01	0.24	0.15	0.08	98.52
26.63	0.16	1.35	0.90	41.90	0.23	20.49	0.48	0.06	0.06	0.67	0.10	0.39	93.57
32.99	0.00	0.10	0.03	35.38	0.25	29.95	0.13	0.00	0.01	0.03	0.01	0.01	98.91
28.91	0.06	0.42	0.28	35.43	0.23	20.89	0.17	0.02	0.00	0.39	0.07	0.08	87.04
33.29	0.00	0.15	0.27	37.76	0.20	26.65	0.19	0.07	0.00	0.17	0.13	0.55	99.63
31.98	0.02	0.54	0.26	40.09	0.23	22.53	0.23	0.05	0.00	0.53	0.06	0.18	96.77
29.77	0.09	0.83	0.32	38.43	0.27	21.31	0.29	0.05	0.02	0.58	0.32	0.16	92.92
26.09	0.10	0.83	0.41	38.15	0.22	18.78	0.30	0.03	0.02	0.50	0.06	0.17	85.73
24.37	0.14	1.52	0.50	37.10	0.27	23.74	0.39	0.03	0.07	0.84	0.14	0.19	89.52

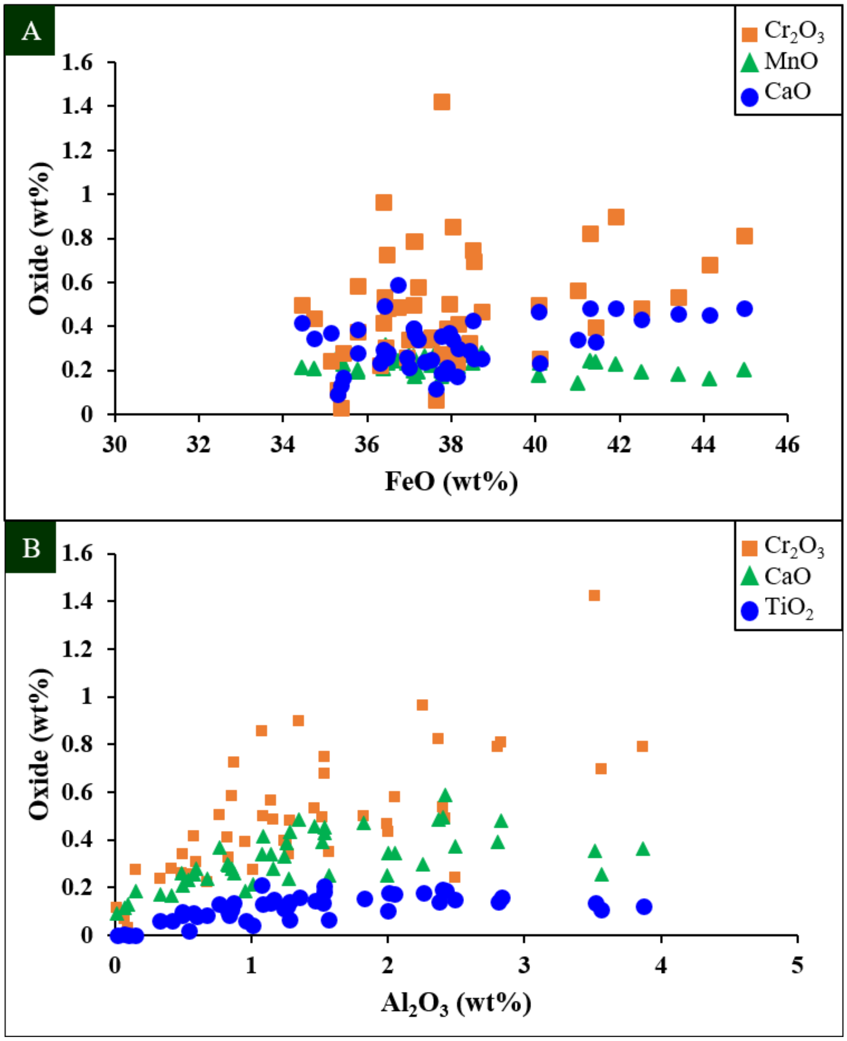

Figure 36: (A) A variation diagram of oxide contents (wt%) versus FeO contents (wt%) for the host matrix material. (B) A variation diagram of oxide contents (wt%) versus Al_2O_3 contents (wt%) for the host matrix material. These analyses for the host matrix were obtained using a 50 µm beam size and thus reflect compositions of bulk matrix material and not individual mineral phases.

3.2.1.iv. Halo Region Bulk Composition Relationships

Within the host matrix, unique high Z haloes occur, as described earlier (Figure 10). An EPMA traverse was taken across one region of a halo using a 1 μm beam size to examine the compositional variations across the boundary defined by the halo (Figure 37). Due to the fine-grained nature of this material and resultant variable analytical totals for the EPMA analyses, the profile data are plotted as ratios to Si. There are significant variations in the Mg/Si and Fe/Si ratios along the profile, but no evidence of a significant difference between the ratios on either side of the high Z zone. There is spike in the Fe/Si ratio and a correlated decrease in the Mg/Si ratio that coincides with the inner part of high Z zone. There are other peaks in the Fe/Si ratios along the profile elsewhere in the matrix, but the inverse correlation with the Mg/Si ratio is not so pronounced. The increase in Fe/Si in the high Z zone is also correlated with spikes in the Al/Si, Ni/Si, and S/Si ratios. In the case of the latter two elements, the correlated increase indicates the possibility of small Ni-sulfide inclusions within the matrix The Ca/Si concentration remains low and not variable at the beginning of the traverse but spikes to about 11wt% by the end of the traverse, recording a pyroxene grain within the matrix. The Al/Si besides having a few spikes along the profile remains relatively consist around 0.2.

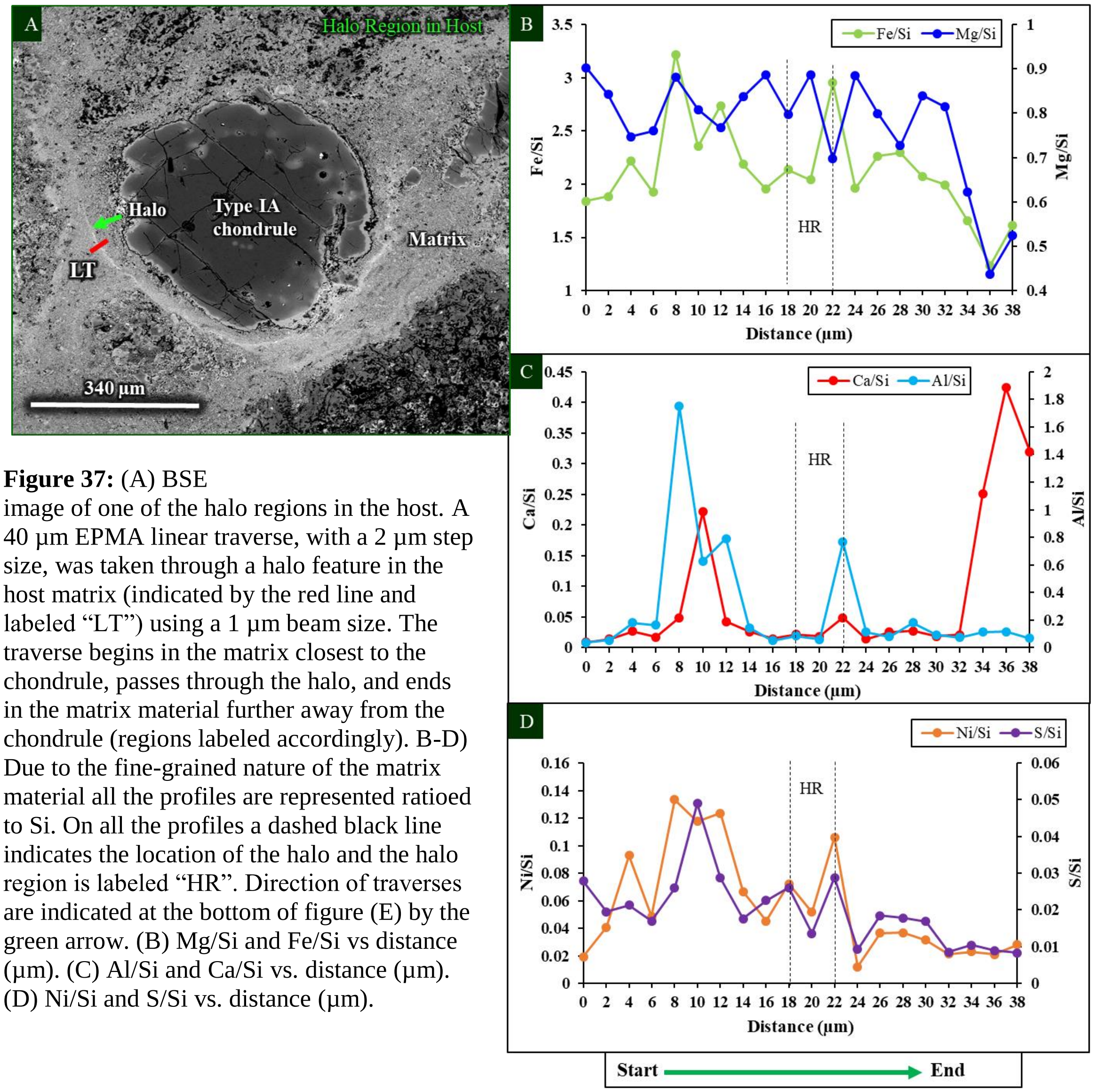

Figure 37: (A) BSE image of one of the halo regions in the host. A 40 µm EPMA linear traverse, with a 2 µm step size, was taken through a halo feature in the host matrix (indicated by the red line and labeled "LT") using a 1 µm beam size. The traverse begins in the matrix closest to the chondrule, passes through the halo, and ends in the matrix material further away from the chondrule (regions labeled accordingly). B-D) Due to the fine-grained nature of the matrix material all the profiles are represented ratioed to Si. On all the profiles a dashed black line indicates the location of the halo and the halo region is labeled "HR". Direction of traverses are indicated at the bottom of figure (E) by the green arrow. (B) Mg/Si and Fe/Si vs distance (µm). (C) Al/Si and Ca/Si vs. distance (µm). (D) Ni/Si and S/Si vs. distance (µm).

3.2.2 Lithic Inclusion

3.2.2.i. LI Mineral Chemistry of type IA chondrules, type IIA chondrules, Mg-rich & Fe-rich grains: Olivines

Representative chondrule olivine phenocrysts and Mg- and Fe-rich isolated olivine grains were chosen from the two sections (the thin section and thick section) of the LI to examine the mineral chemistry of the primary and secondary phases seen by SEM. Both the type IA and type IIA chondrules show signs of alteration, as shown in Figures 12-20, notably development of ferroan overgrowths around the original primary chondrule olivine phenocrysts, the complete replacement of enstatite, and the replacement of metal nodules within both types of chondrules. The type IA chondrule olivine phenocryst cores range in composition from $Fa_{0.34}$-$Fa_{31.42}$ (see Table 9), compared with $Fa_{37.58}$-$Fa_{44.72}$ for the ferroan overgrowths (see Table 10). In type IIA chondrules, the olivine phenocrysts range in composition from $Fa_{14.65}$-$Fa_{49.25}$ (see Table 11) with overgrowth compositions from $Fa_{42.3}$-$Fa_{43.63}$ (see Table 12). The Mg-rich grains range in composition from $Fa_{0.32}$-$Fa_{4.22}$ (see Table 13) and the Fe-rich grains vary in composition from $Fa_{25.35}$-$Fa_{43.01}$ (see Table 14). Histograms of the Fa (mol%) contents for type IA chondrule olivine phenocrysts, ferroan overgrowths, and the Mg-rich isolated olivine grains are shown in Figures 28c-e.

Figure 38 shows the minor element relationships for olivine analyses from several type IA chondrule olivine phenocrysts and Mg-rich isolated olivine grains. For both types of olivine, the CaO and Cr_2O_3 contents decrease with increasing FeO content, although there is some scatter in the type IA chondrule olivine phenocryst data. The MnO contents also show a positive correlation with increasing FeO content. The range in MnO contents for occurrences of olivine is similar with a maximum MnO content of ~0.3 wt%. In contrast, both CaO and Cr_2O_3 contents are a negatively correlated with FeO content.

The refractory element CaO for both the Mg-rich isolated olivine grains and the chondrule olivine phenocrysts increases with increasing Al_2O_3 values. In general the TiO_2 concentrations for both olivine occurrences do not show much change with increasing Al_2O_3. The TiO_2 values are all approximately less than 0.1 wt%. The Cr_2O_3 content is positively correlated with Al_2O_3 until the Al_2O_3 concentration reaches approximately 0.2 wt%. At this value, Cr_2O_3 becomes negatively correlated with Al_2O_3 wt%.

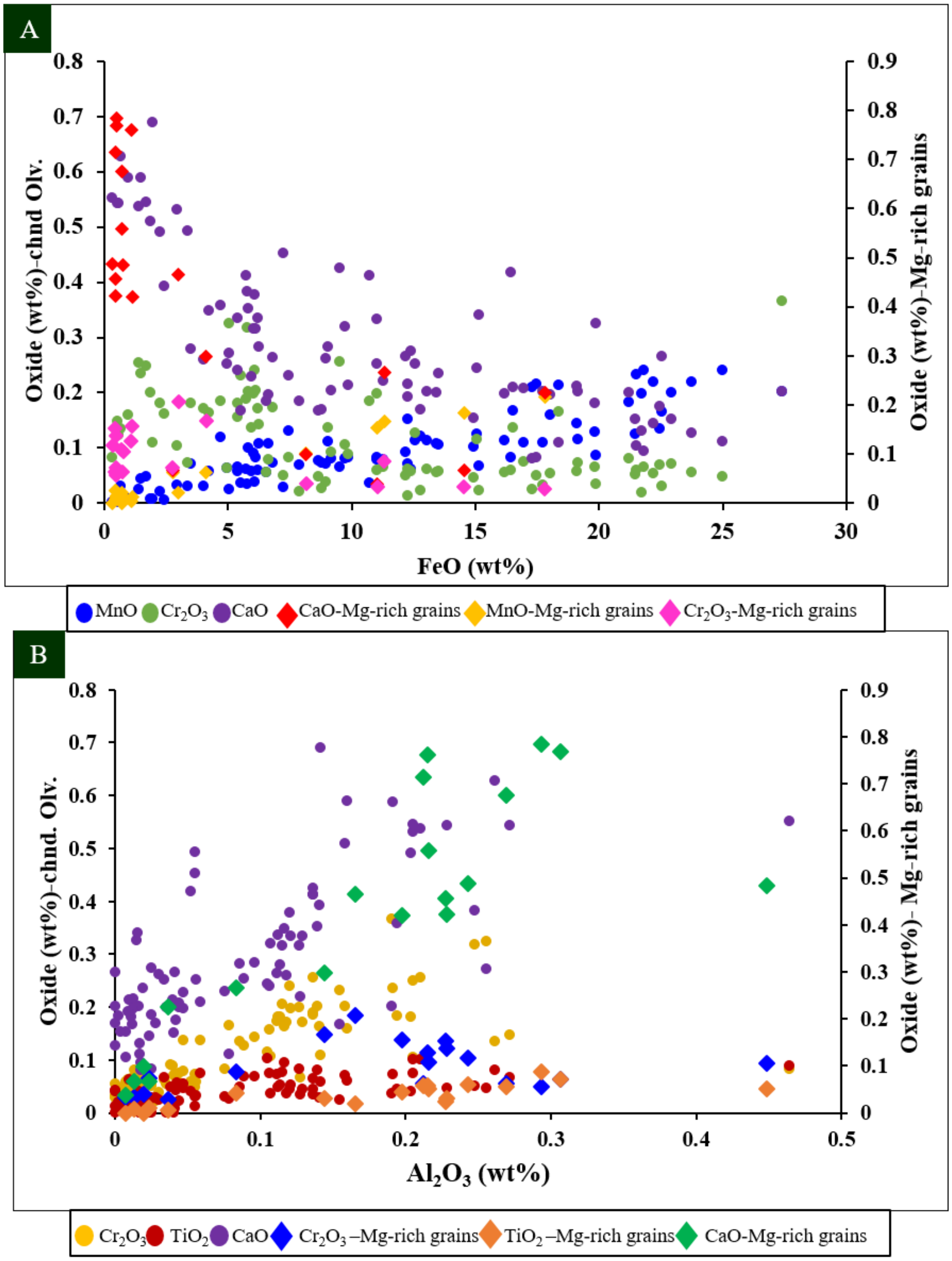

Figure 38: (A) A variation diagram of oxide contents (wt%) versus FeO contents (wt%) of compiled analyses for the LI type IIA chondrule olivine phenocrysts, the type IIA chondrule olivine ferroan overgrowths, and the Fe-rich isolated olivine grains. (B) A variation diagram of oxide contents (wt%) versus Al_2O_3 contents (wt%) of compiled analyses for the LI type IIA chondrule olivine phenocrysts and the type IIA chondrule olivine ferroan overgrowths. (C) A variation diagram of oxide contents (wt%) versus Al_2O_3 contents (wt%) of compiled analyses for the type IIA chondrule olivine phenocrysts and the Fe-rich isolated olivine grains.

Lastly, Figure 30 shows the Mg-rich isolated olivine grains, the LI type IA chondrule olivine phenocrysts, and the host type IA chondrule olivine phenocrysts for FeO wt% vs Al_2O_3 wt%. In general, the Al_2O_3 contents for both the LI type IA chondrule olivine phenocrysts and the Mg-rich isolated olivine grains are negatively correlated with increasing FeO concentration, the same relationship observed for the host type IA chondrule olivine phenocrysts. The main difference between the three types of olivine is that the LI inclusion olivines have higher Al_2O_3 concentrations than the host type IA chondrule olivine phenocrysts do. However, as FeO content increases, the Al_2O_3 concentrations in all three occurrences of olivine become similar.

The compositional variations in ferroan olivine overgrowths on type IA chondrule olivine phenocrysts are shown in Figure 39. There is a slight increase in MnO concentration as FeO increases, but the MnO values never exceed ~0.3 wt%, similar to that of the type IA chondrule olivine phenocrysts. The CaO concentration is positively correlated with increasing FeO values until approximately 37 wt% FeO. There is no evident correlation with the TiO_2 concentration as FeO increases. The Cr_2O_3 concentration has some scatter and no correlation with FeO as is seen in the type IA chondrule olivine phenocrysts and the Mg-rich isolated olivine grains. The elevated Cr_2O_3 concentrations (0.6 wt%) are likely attributable to submicron-sized chromite grains found within the ferroan overgrowth. The refractory elements do not show any evident element correlations and are not discussed here.

Figure 40a-d show a compositional zoning profile from a LI type IA chondrule olivine phenocryst. As for previous examples, the first few microns are fine-grained matrix, followed by a ferroan overgrowth and into the chondrule phenocrysts. In the matrix, the analyses are a mixture of fine-grained phases, so that peaks in Al, Cr, Ni, S, Ti, and Na are the result of a combination of phases being analyzed simultaneously. The ferroan overgrowth has composition of Fa_{40} with little variation. The minor elements Mn, Al, Ti, Na, S, and Ni are also constant through the overgrowth. The Cr profile has a sharp increase at 30 to 40 μm along the profile, most likely attributable to the presence of chromite grains (≤1 μm) present within the ferroan overgrowth. The Fa content decreases in the last part of the profile into the interior of the phenocryst, in the same manner as observed in profiles from the host. All of the minor elements (Mn, Al, Ni, Ti, S, and Cr) decrease from the overgrowth into the phenocryst.

Table 9: Representative electron microprobe analyses of LI type IA chondrule olivine phenocrysts without ferroan overgrowths with formulae calculated on the basis of [4] oxygen atoms. All analyses taken with a 1 µm beam size.

Oxide (wt%)

SiO_2	TiO_2	Al_2O_3	Cr_2O_3	FeO	MnO	MgO	CaO	Na_2O	K_2O	NiO	S	P_2O_5	TOTAL
39.92	0.04	0.05	0.06	16.43	0.08	43.80	0.42	b.d.	b.d.	0.02	0.01	b.d.	100.84
42.48	0.10	0.21	0.10	2.95	0.03	54.34	0.53	0.01	b.d.	b.d.	b.d.	0.01	100.76
38.81	0.01	0.02	0.03	19.89	0.09	40.52	0.33	b.d.	b.d.	0.03	0.01	b.d.	99.73
40.23	0.02	0.04	0.06	13.43	0.11	46.01	0.20	0.01	b.d.	0.12	b.d.	0.01	100.23
40.63	0.03	0.13	0.07	11.28	0.08	47.53	0.22	0.05	b.d.	0.11	b.d.	0.01	100.15
39.71	0.04	0.00	0.03	17.74	0.11	41.67	0.20	b.d.	b.d.	0.00	b.d.	N/A	99.52
40.70	0.01	0.01	0.01	12.28	0.15	46.73	0.21	b.d.	0.01	0.02	b.d.	N/A	100.15
41.86	0.05	0.05	0.08	6.63	0.11	50.69	0.20	0.01	b.d.	0.00	b.d.	N/A	99.66
41.68	0.05	0.19	0.18	4.71	0.12	51.83	0.36	0.01	b.d.	0.03	b.d.	N/A	99.16
42.20	0.07	0.27	0.15	0.52	0.01	55.67	0.54	b.d.	0.02	0.00	b.d.	N/A	99.45

Number of cations per 4 Oxygen anions

Si	Ti	Al	Cr	Fe	Mn	Mg	Ca	Na	K	Ni	S	P	Sum	Fa (mol%)
1.000	0.001	0.002	0.001	0.344	0.002	1.636	0.011	b.d.	b.d.	b.d.	b.d.	b.d.	2.997	17.39
1.001	0.002	0.006	0.002	0.058	0.001	1.909	0.013	b.d.	b.d.	b.d.	b.d.	b.d.	2.993	2.95
1.000	b.d.	b.d.	0.001	0.429	0.002	1.557	0.009	b.d.	b.d.	0.001	b.d.	b.d.	2.999	21.60
1.000	b.d.	0.001	0.001	0.279	0.002	1.705	0.005	b.d.	b.d.	0.002	b.d.	b.d.	2.998	14.07
1.001	0.001	0.004	0.001	0.232	0.002	1.745	0.006	0.002	b.d.	0.002	b.d.	b.d.	2.996	11.75
1.013	0.001	b.d.	0.001	0.378	0.002	1.585	0.006	b.d.	b.d.	b.d.	b.d.	NA	2.986	19.27
1.006	b.d.	b.d.	b.d.	0.254	0.003	1.723	0.006	b.d.	b.d.	b.d.	b.d.	NA	2.993	12.85
1.012	0.001	0.001	0.001	0.134	0.002	1.828	0.005	b.d.	b.d.	b.d.	b.d.	NA	2.986	6.83
1.006	0.001	0.006	0.004	0.095	0.002	1.865	0.009	b.d.	b.d.	0.001	b.d.	NA	2.989	4.85
0.998	0.001	0.008	0.003	0.010	b.d.	1.962	0.014	b.d.	0.001	b.d.	b.d.	NA	2.996	0.52

Table 10: Representative electron microprobe analyses of LI type IA chondrule olivine phenocryst ferroan overgrowths with formulae calculated on the basis of [4] oxygen atoms. All analyses taken with a 1 µm beam size.

Oxide (wt%)													
SiO_2	TiO_2	Al_2O_3	Cr_2O_3	FeO	MnO	MgO	CaO	Na_2O	K_2O	NiO	S	P_2O_5	TOTAL
38.95	0.09	0.42	0.27	32.80	0.23	27.49	0.30	0.07	0.01	0.05	0.02	0.06	100.79
35.64	0.05	0.18	0.13	31.59	0.24	27.92	0.22	0.08	0.01	0.07	0.02	0.10	96.27
34.12	0.04	0.86	0.54	31.13	0.23	25.64	0.19	0.13	0.03	0.12	0.02	0.17	93.26
35.17	0.05	0.72	0.24	31.53	0.23	29.37	0.14	0.07	0.01	0.02	0.01	0.15	97.70
34.71	0.09	0.73	2.84	30.92	0.25	28.06	0.25	0.13	0.02	0.02	0.02	0.13	98.21
35.71	0.02	0.05	0.18	36.74	0.30	25.48	0.20	0.02	0.01	0.04	b.d.	b.d.	98.77
36.24	0.04	0.26	0.65	31.61	0.21	29.40	0.16	0.06	0.01	0.01	0.01	0.05	98.72

Number of cations per 4 Oxygen anions														
Si	Ti	Al	Cr	Fe	Mn	Mg	Ca	Na	K	Ni	S	P	Sum	Fa (mol%)
1.050	0.002	0.013	0.006	0.739	0.005	1.105	0.009	0.004	b.d.	0.001	0.001	0.001	2.937	40.10
1.013	0.001	0.006	0.003	0.751	0.006	1.183	0.007	0.004	b.d.	0.002	0.001	0.002	2.978	38.83
1.005	0.001	0.030	0.013	0.767	0.006	1.125	0.006	0.008	0.001	0.003	0.001	0.004	2.969	40.52
0.984	0.001	0.024	0.005	0.738	0.005	1.225	0.004	0.004	b.d.	b.d.	b.d.	0.004	2.996	37.59
0.971	0.002	0.024	0.063	0.724	0.006	1.171	0.008	0.007	0.001	b.d.	0.001	0.003	2.980	38.20
1.013	0.001	0.002	0.004	0.872	0.007	1.077	0.006	0.001	b.d.	0.001	b.d.	b.d.	2.984	44.72
1.002	0.001	0.008	0.014	0.731	0.005	1.213	0.005	0.003	b.d.	b.d.	b.d.	0.001	2.985	37.62

Table 11: Representative electron microprobe analyses of LI type IIA chondrule olivine phenocrysts excluding ferroan overgrowths with formulae calculated on the basis of [4] oxygen atoms. All analyses taken with a 1 µm beam size.

						Oxide (wt%)							
SiO_2	TiO_2	Al_2O_3	Cr_2O_3	FeO	MnO	MgO	CaO	Na_2O	K_2O	NiO	S	P_2O_5	TOTAL
41.27	0.01	0.24	0.13	13.64	0.14	44.58	0.11	0.02	0.01	0.11	b.d.	NA	100.25
38.82	b.d.	0.03	0.06	21.80	0.18	38.97	0.18	b.d.	b.d.	0.05	b.d.	NA	100.09
37.46	0.01	0.03	0.07	27.58	0.26	33.98	0.10	b.d.	b.d.	0.06	b.d.	NA	99.56
36.28	b.d.	0.03	0.08	33.58	0.33	29.00	0.14	0.02	0.02	0.08	0.01	NA	99.58
36.12	b.d.	0.02	0.04	33.46	0.27	29.12	0.07	b.d.	b.d.	0.02	b.d.	NA	99.12
36.89	b.d.	0.02	0.06	32.01	0.24	30.22	0.07	0.02	b.d.	0.09	b.d.	NA	99.63
34.98	0.02	0.01	0.00	40.21	0.41	23.24	0.10	0.01	b.d.	0.08	b.d.	NA	99.06
35.11	b.d.	0.03	0.03	37.46	0.39	25.33	0.32	0.02	b.d.	0.03	NA	NA	98.72
36.00	b.d.	0.12	0.27	34.77	0.23	27.50	0.27	0.11	b.d.	0.06	NA	NA	99.33
36.58	0.01	0.02	0.05	35.27	0.23	27.71	0.18	0.01	b.d.	0.06	NA	NA	100.11

							Number of cations per 4 Oxygen anions							
Si	Ti	Al	Cr	Fe	Mn	Mg	Ca	Na	K	Ni	S	P	Sum	Fa (mol%)
1.023	b.d.	0.007	0.002	0.283	0.003	1.648	0.003	0.001	b.d.	0.002	b.d.	NA	2.972	14.65
1.005	b.d.	0.001	0.001	0.472	0.004	1.504	0.005	b.d.	b.d.	0.001	b.d.	NA	2.994	23.89
1.004	b.d.	0.001	0.001	0.619	0.006	1.358	0.003	b.d.	b.d.	0.001	b.d.	NA	2.994	31.29
1.004	b.d.	0.001	0.002	0.777	0.008	1.196	0.004	0.001	0.001	0.002	b.d.	NA	2.995	39.37
1.003	b.d.	0.001	0.001	0.777	0.006	1.206	0.002	b.d.	b.d.	0.000	b.d.	NA	2.996	39.19
1.010	b.d.	0.001	0.001	0.733	0.006	1.234	0.002	0.001	b.d.	0.002	b.d.	NA	2.989	37.27
1.008	b.d.	b.d.	b.d.	0.969	0.010	0.998	0.003	b.d.	b.d.	0.002	b.d.	NA	2.991	49.25
1.002	b.d.	0.001	0.001	0.894	0.009	1.078	0.010	0.001	b.d.	0.001	NA	NA	2.997	45.35
1.005	b.d.	0.004	0.006	0.812	0.005	1.145	0.008	0.006	b.d.	0.001	NA	NA	2.993	41.50
1.013	b.d.	b.d.	0.001	0.816	0.005	1.143	0.005	b.d.	b.d.	0.001	NA	NA	2.987	41.66

Table 12: Representative electron microprobe analyses of LI type IIA chondrule olivine phenocryst ferroan overgrowths with formulae calculated on the basis of [4] oxygen atoms. All analyses taken with a 1 µm beam size.

Oxide (wt%)

SiO_2	TiO_2	Al_2O_3	Cr_2O_3	FeO	MnO	MgO	CaO	Na_2O	K_2O	NiO	S	P_2O_5	TOTAL
35.19	0.04	1.05	0.25	35.12	0.26	25.45	0.22	0.09	0.02	0.07	0.13	0.06	97.97
33.06	0.06	0.61	0.29	34.56	0.25	26.44	0.25	0.06	0.01	0.12	0.11	0.05	95.87
34.49	0.05	0.47	0.23	35.18	0.24	26.49	0.22	0.05	0.01	0.09	0.21	0.03	97.77

Number of cations per 4 Oxygen anions

Si	Ti	Al	Cr	Fe	Mn	Mg	Ca	Na	K	Ni	S	P	Sum	Fa (mol%)
0.999	0.001	0.035	0.006	0.833	0.006	1.077	0.007	0.005	0.001	0.002	0.003	0.001	2.975	43.63
0.966	0.001	0.021	0.007	0.844	0.006	1.151	0.008	0.003	b.d.	0.003	0.002	0.001	3.014	42.31
0.984	0.001	0.016	0.005	0.839	0.006	1.127	0.007	0.003	0.001	0.002	0.005	0.001	2.996	42.69

Table 13: Representative electron microprobe analyses of Mg-rich isolated olivine grains in the LI with formulae calculated on the basis of [4] oxygen atoms. All analyses taken with a 1 µm beam size.

Oxide (wt%)													
SiO_2	TiO_2	Al_2O_3	Cr_2O_3	FeO	MnO	MgO	CaO	Na_2O	K_2O	NiO	S	P_2O_5	TOTAL
42.25	0.03	0.14	0.17	4.11	0.06	52.37	0.30	0.02	b.d.	0.02	0.01	NA	99.49
43.21	0.06	0.21	0.06	0.44	0.03	56.75	0.71	b.d.	b.d.	b.d.	b.d.	NA	101.48
43.54	0.07	0.31	0.07	0.48	0.01	55.44	0.77	b.d.	b.d.	b.d.	b.d.	NA	100.69
42.52	0.09	0.29	0.06	0.48	0.01	56.76	0.78	b.d.	b.d.	0.01	0.01	NA	101.03
43.47	0.06	0.22	0.13	1.09	b.d.	54.93	0.76	b.d.	b.d.	b.d.	b.d.	NA	100.65
42.43	0.05	0.45	0.10	0.77	0.01	57.34	0.48	b.d.	0.01	0.01	b.d.	NA	101.67
41.70	0.02	0.23	0.15	0.43	0.01	56.37	0.46	b.d.	b.d.	0.03	b.d.	NA	99.42
42.16	0.06	0.24	0.12	0.33	b.d.	57.56	0.49	b.d.	b.d.	0.01	b.d.	NA	100.96
42.96	0.03	0.23	0.14	0.46	0.03	56.24	0.42	b.d.	b.d.	b.d.	b.d.	NA	100.50
42.34	0.06	0.27	0.06	0.73	b.d.	56.90	0.67	0.01	0.01	0.01	b.d.	NA	101.07

Number of cations per 4 Oxygen anions														
Si	Ti	Al	Cr	Fe	Mn	Mg	Ca	Na	K	Ni	S	P	Sum	Fa (mol%)
1.012	0.001	0.004	0.003	0.082	0.001	1.870	0.008	0.001	b.d.	b.d.	0.001	NA	2.983	4.22
1.001	0.001	0.006	0.001	0.009	0.001	1.959	0.018	b.d.	b.d.	b.d.	b.d.	NA	2.995	0.43
1.014	0.001	0.008	0.001	0.009	b.d.	1.926	0.019	b.d.	b.d.	b.d.	b.d.	NA	2.980	0.48
0.991	0.002	0.008	0.001	0.009	b.d.	1.972	0.020	b.d.	b.d.	b.d.	b.d.	NA	3.003	0.47
1.016	0.001	0.006	0.002	0.021	b.d.	1.914	0.019	b.d.	b.d.	b.d.	b.d.	NA	2.979	1.10
0.984	0.001	0.012	0.002	0.015	b.d.	1.982	0.012	b.d.	b.d.	b.d.	b.d.	NA	3.008	0.74
0.987	b.d.	0.006	0.003	0.009	b.d.	1.990	0.012	b.d.	b.d.	b.d.	b.d.	NA	3.008	0.43
0.983	0.001	0.007	0.002	0.006	b.d.	2.000	0.012	b.d.	b.d.	b.d.	b.d.	NA	3.012	0.32
1.003	0.001	0.006	0.003	0.009	0.001	1.959	0.011	b.d.	b.d.	b.d.	b.d.	NA	2.991	0.46
0.988	0.001	0.007	0.001	0.014	b.d.	1.978	0.017	0.001	b.d.	b.d.	b.d.	NA	3.007	0.71

Table 14: Representative electron microprobe analyses of Fe-rich isolated olivine grains in the LI with formulae calculated on the basis of [4] oxygen atoms. All analyses taken with a 1 µm beam size.

Oxide (wt%)													
SiO_2	TiO_2	Al_2O_3	Cr_2O_3	FeO	MnO	MgO	CaO	Na_2O	K_2O	NiO	S	P_2O_5	TOTAL
36.78	0.01	0.05	0.09	27.55	0.25	33.71	0.19	0.01	0.01	0.02	b.d.	NA	98.68
37.18	b.d.	0.03	0.10	26.84	0.22	33.59	0.12	0.01	b.d.	0.09	b.d.	NA	98.19
37.53	0.02	0.05	0.07	30.88	0.30	30.24	0.16	0.01	b.d.	0.06	b.d	NA	99.32
37.17	b.d.	0.03	0.07	30.05	0.31	31.46	0.19	0.02	b.d.	0.05	b.d.	NA	99.40
35.99	b.d.	0.03	0.06	35.92	0.38	26.70	0.35	b.d.	b.d.	0.05	0.01	NA	99.50
37.33	b.d.	0.02	0.05	34.34	0.37	26.55	0.26	0.04	b.d.	0.06	0.01	NA	99.05
37.25	0.02	0.05	0.11	28.49	0.18	33.14	0.21	0.02	b.d.	0.03	b.d.	NA	99.52
37.52	b.d.	0.05	0.10	29.04	0.23	32.12	0.20	b.d.	b.d.	0.05	b.d.	NA	99.31
37.58	b.d.	0.04	0.09	29.79	0.27	31.66	0.21	b.d.	b.d.	0.04	0.01	NA	99.71
36.70	0.01	0.04	0.09	34.64	0.29	27.88	0.13	0.01	b.d.	0.05	b.d.	NA	99.84
37.68	b.d.	0.05	0.07	22.58	0.16	37.29	0.12	0.02	b.d.	0.08	b.d.	NA	98.07

Number of cations per 4 Oxygen anions														
Si	Ti	Al	Cr	Fe	Mn	Mg	Ca	Na	K	Ni	S	P	Sum	Fa (mol%)
0.997	b.d.	0.001	0.002	0.625	0.006	1.363	0.005	0.001	b.d.	0.001	b.d.	NA	3.001	31.44
1.009	b.d.	0.001	0.002	0.609	0.005	1.358	0.004	0.001	b.d.	0.002	b.d.	NA	2.990	30.95
1.024	b.d.	0.002	0.002	0.704	0.007	1.230	0.005	0.001	b.d.	0.001	b.d.	NA	2.975	36.42
1.011	b.d.	0.001	0.002	0.683	0.007	1.275	0.006	0.001	b.d.	0.001	0.001	NA	2.987	34.89
1.009	b.d.	0.001	0.001	0.842	0.009	1.116	0.011	b.d.	b.d.	0.001	b.d.	NA	2.990	43.01
1.038	b.d.	0.001	0.001	0.799	0.009	1.101	0.008	0.002	b.d.	0.001	0.001	NA	2.961	42.05
1.004	b.d.	0.002	0.002	0.642	0.004	1.332	0.006	0.001	b.d.	0.001	b.d.	NA	2.994	32.53
1.015	b.d.	0.002	0.002	0.657	0.005	1.295	0.006	b.d.	b.d.	0.001	b.d.	NA	2.983	33.66
1.016	b.d.	0.001	0.002	0.673	0.006	1.276	0.006	b.d.	b.d.	0.001	b.d.	NA	2.982	34.55
1.016	b.d.	0.001	0.002	0.802	0.007	1.150	0.004	0.001	b.d.	0.001	b.d.	NA	2.983	41.08
1.002	b.d.	0.002	0.002	0.502	0.004	1.479	0.003	0.001	b.d.	0.002	b.d.	NA	2.997	25.35

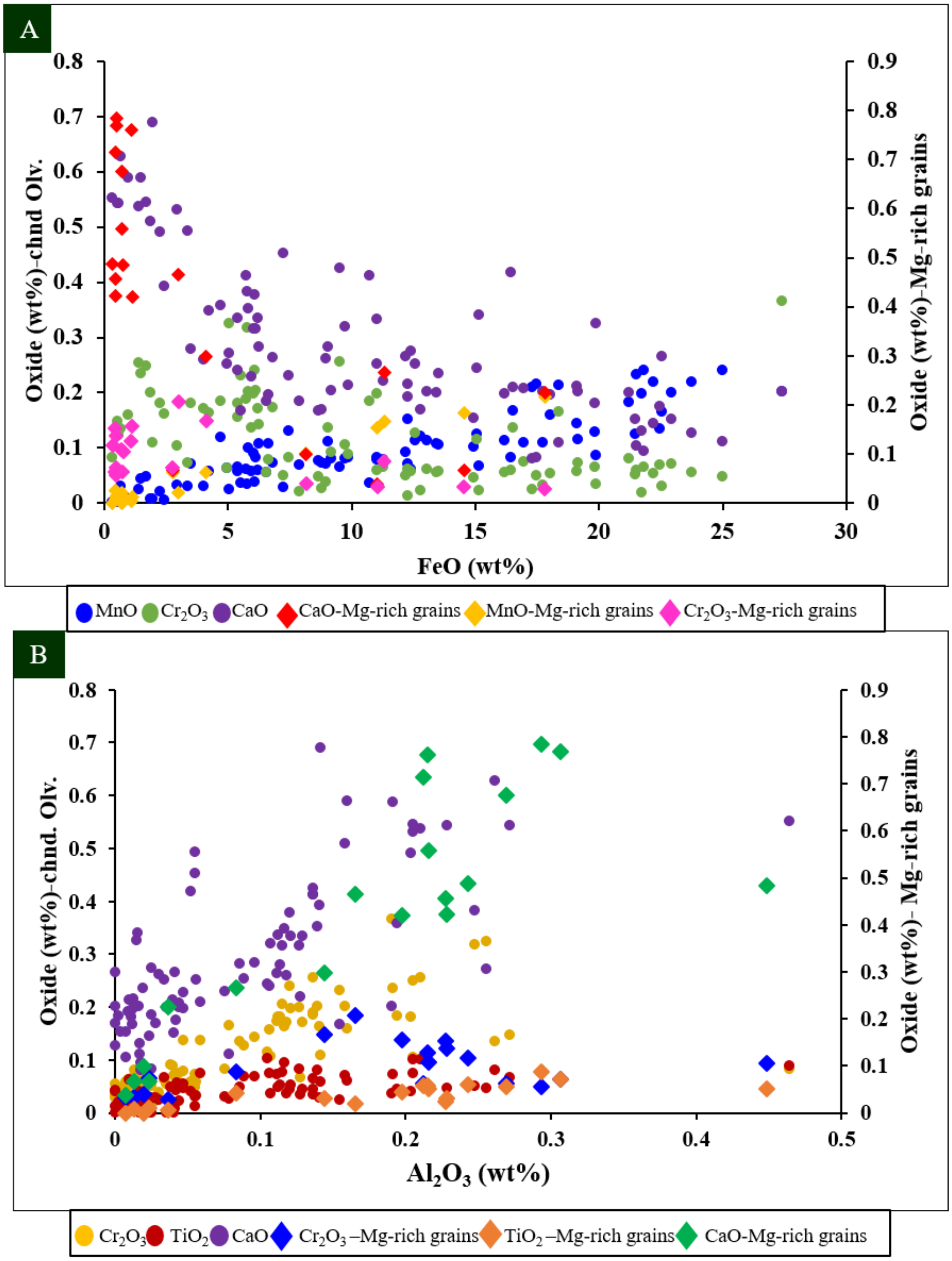

Figure 38: (A) A variation diagram of oxide contents (wt%) for analyses of LI type IA chondrule olivine phenocrysts (left y-axis) and oxide contents (wt%) for compiled analyses of LI Mg-rich isolated olivine grains (secondary y-axis) versus FeO contents (wt%). (B) A variation diagram of oxide contents (wt%) for compiled analyses of LI type IA chondrule olivine phenocrysts (primary y-axis) and oxide contents (wt%) for compiled analyses of LI Mg-rich isolated olivine grains (secondary y-axis) versus Al_2O_3 contents (wt%).

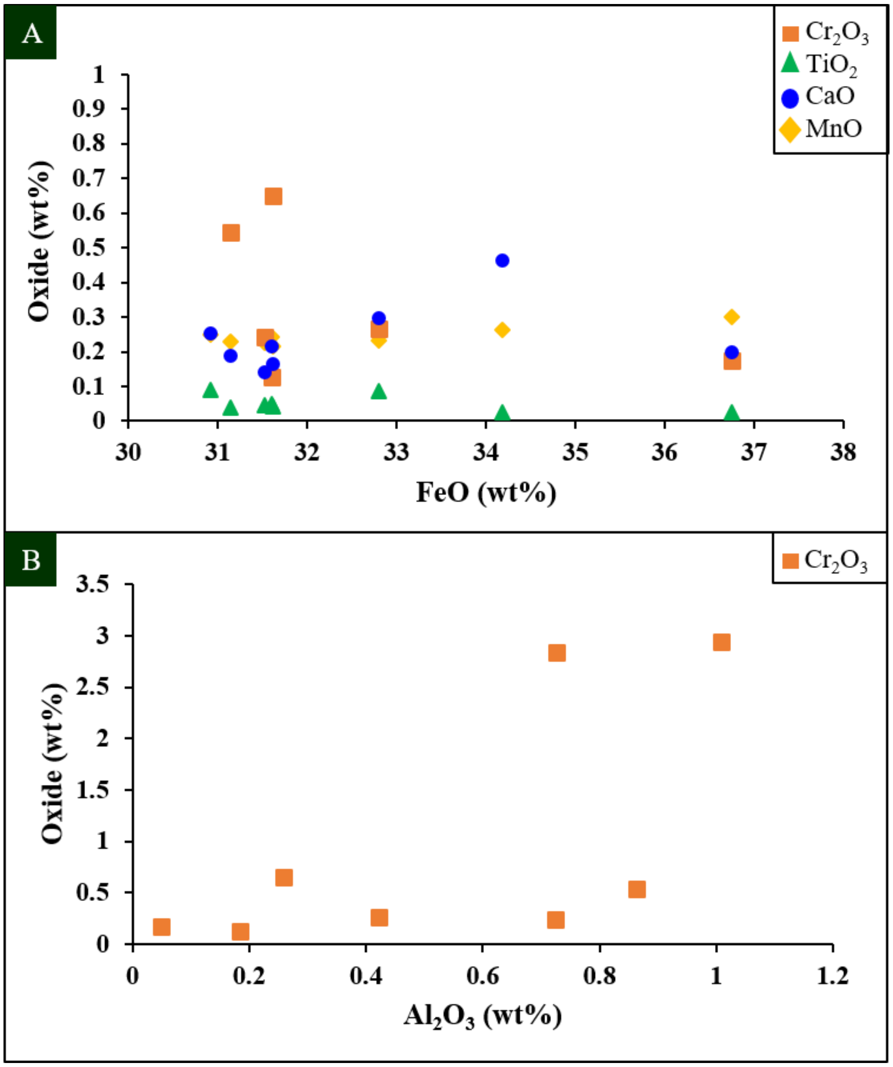

Figure 39: (A) A variation diagram of oxide contents (wt%) versus FeO contents (wt%) for ferroan overgrowth analyses from the type IA LI chondrule olivine phenocrysts. (B) A variation diagram of oxide contents (wt%) versus Al_2O_3 contents (wt%) for a compilation of analyses of ferroan overgrowths in type IA host chondrule olivine phenocrysts.

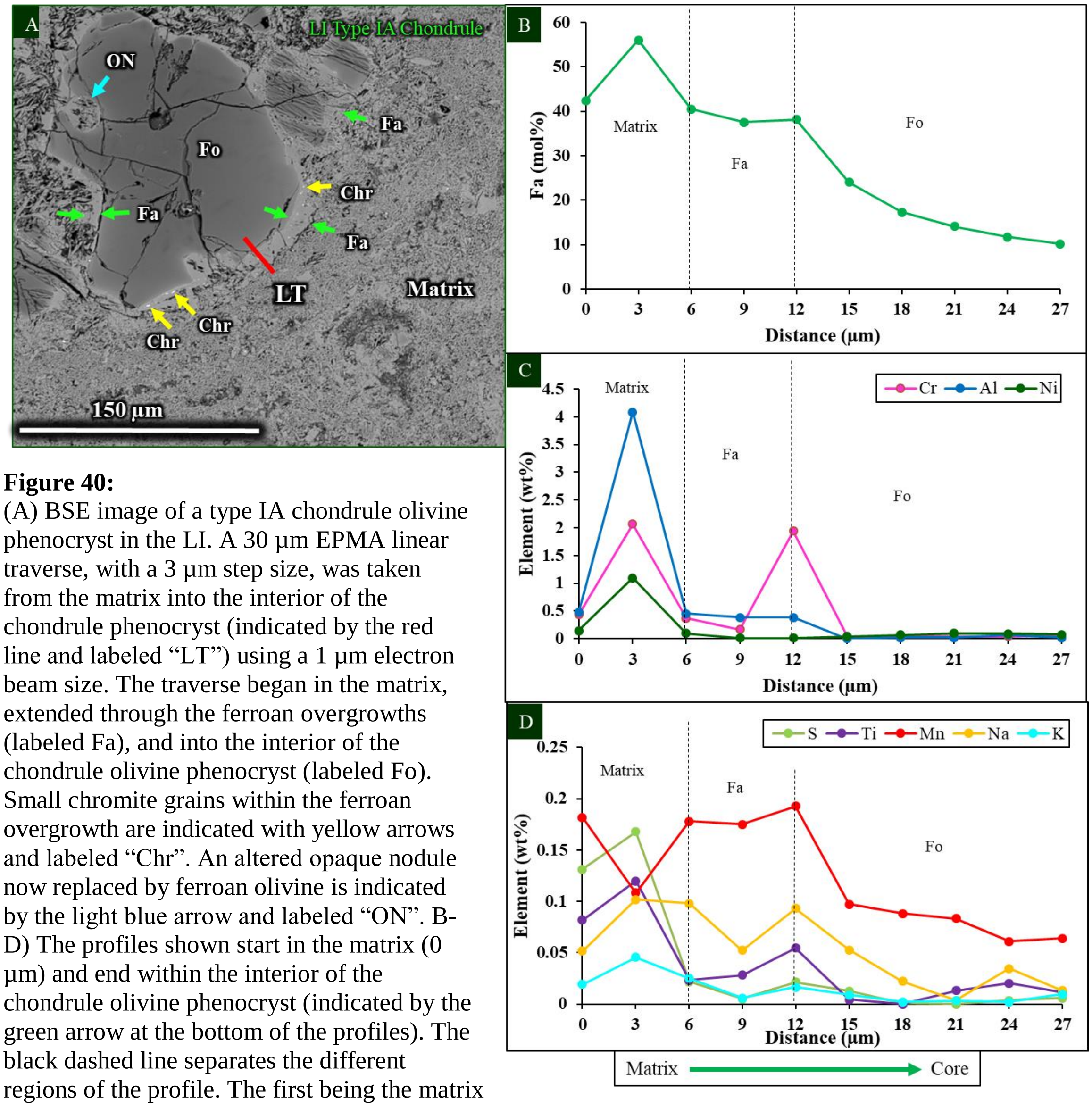

Figure 40:
(A) BSE image of a type IA chondrule olivine phenocryst in the LI. A 30 µm EPMA linear traverse, with a 3 µm step size, was taken from the matrix into the interior of the chondrule phenocryst (indicated by the red line and labeled "LT") using a 1 µm electron beam size. The traverse began in the matrix, extended through the ferroan overgrowths (labeled Fa), and into the interior of the chondrule olivine phenocryst (labeled Fo). Small chromite grains within the ferroan overgrowth are indicated with yellow arrows and labeled "Chr". An altered opaque nodule now replaced by ferroan olivine is indicated by the light blue arrow and labeled "ON". B-D) The profiles shown start in the matrix (0 µm) and end within the interior of the chondrule olivine phenocryst (indicated by the green arrow at the bottom of the profiles). The black dashed line separates the different regions of the profile. The first being the matrix labeled "matrix" and the second is the ferroan overgrowth region labeled "Fa", and the interior portion of the chondrule olivine phenocryst, labeled "Fo". (B) This profile shows the change in Fa (mol%) versus the distance (µm). (C) Ni, Al, Cr (element wt%) vs. distance in microns. (D) Ti, Na, K, S, and Mn (element wt%) vs. distance in microns.

The type IIA chondrule phenocrysts and their ferroan overgrowths show some interesting elemental correlations, as shown in Figures 41a &41b. In the phenocrysts, MnO shows a well-developed positive correlation with FeO, but a negative correlation with Al_2O_3. CaO is also positively correlated with FeO, above a FeO content of ~30 wt%, but at FeO contents <30 wt% shows no systematic behavior. The Cr_2O_3 contents are more scattered, except at high FeO contents, where they show more variability up to much higher Cr_2O_3 values. The refractory elements Al_2O_3 and CaO are uncorrelated.

Type IIA chondrule ferroan overgrowths are comparatively rare in the LI, consequently only a limited amount of EPMA data was collected These overgrowths have FeO contents of 35 wt% with MnO, Cr_2O_3, and CaO contents that do not vary by more than 0.1 wt%. However, the ferroan overgrowths have a higher Cr_2O_3 and CaO content than the majority of the chondrule phenocrysts, whereas the MnO contents are comparable to chondrule phenocryst compositions with similar FeO contents. The ferroan overgrowths contain higher Al_2O_3 contents than the phenocrysts, however there are no systematic correlations between the Al_2O_3 and MnO, Cr_2O_3, and CaO contents.

The FeO contents vs MnO, Cr_2O_3, and CaO contents for the FeO-rich isolated olivine grains show similar correlations as the type IIA chondrule olivine phenocrysts (Figure 41a). The Cr_2O_3 contents have a negative correlation with increasing FeO content, whereas MnO is positively correlated with FeO. The CaO contents show the similar branching at approximately 35 wt% FeO as seen in the type IIA chondrule olivine phenocrysts. Figure 41c shows the variation diagrams for the FeO-rich isolated olivine grains compared with the type IIA chondrule olivine phenocrysts. There are no systematic correlations among the different oxides with increasing Al_2O_3 contents for the isolated grains. The Fe-rich isolated olivine grains all have Al_2O_3 contents <0.05 wt% whereas the type IIA chondrule olivine phenocrysts have up to 0.25 wt% Al_2O_3 contents.

In the type IIA chondrule olivine phenocrysts, the ferroan overgrowths are not as common or as well defined as in the type IA chondrule olivine phenocrysts, but we report this profile as being a representative example. Figures 42a-d show a zoning profile for one of these type IIA chondrules. The first step, plotted at 0 µm, shows the compositions in the fine-grained matrix material. The Fa mol% content decreases by approximately 6 mol% by the 3 µm step representing the transition through the ferroan overgrowth region. The Ca, S, and Ni follow a similar correlation as the profile reaches 3 µm. The Cr wt% follows an opposite pattern and slightly increases. The ferroan overgrowth width is roughly 2-3 µm and is probably not captured well in this profile. The Fa mol% decreases by approximately 2 mol% across this step in the profile. Ni, S, Ca, and Cr also all decrease in content within this region along the profile with Ni decreasing the most, by approximately 0.3 element wt%.

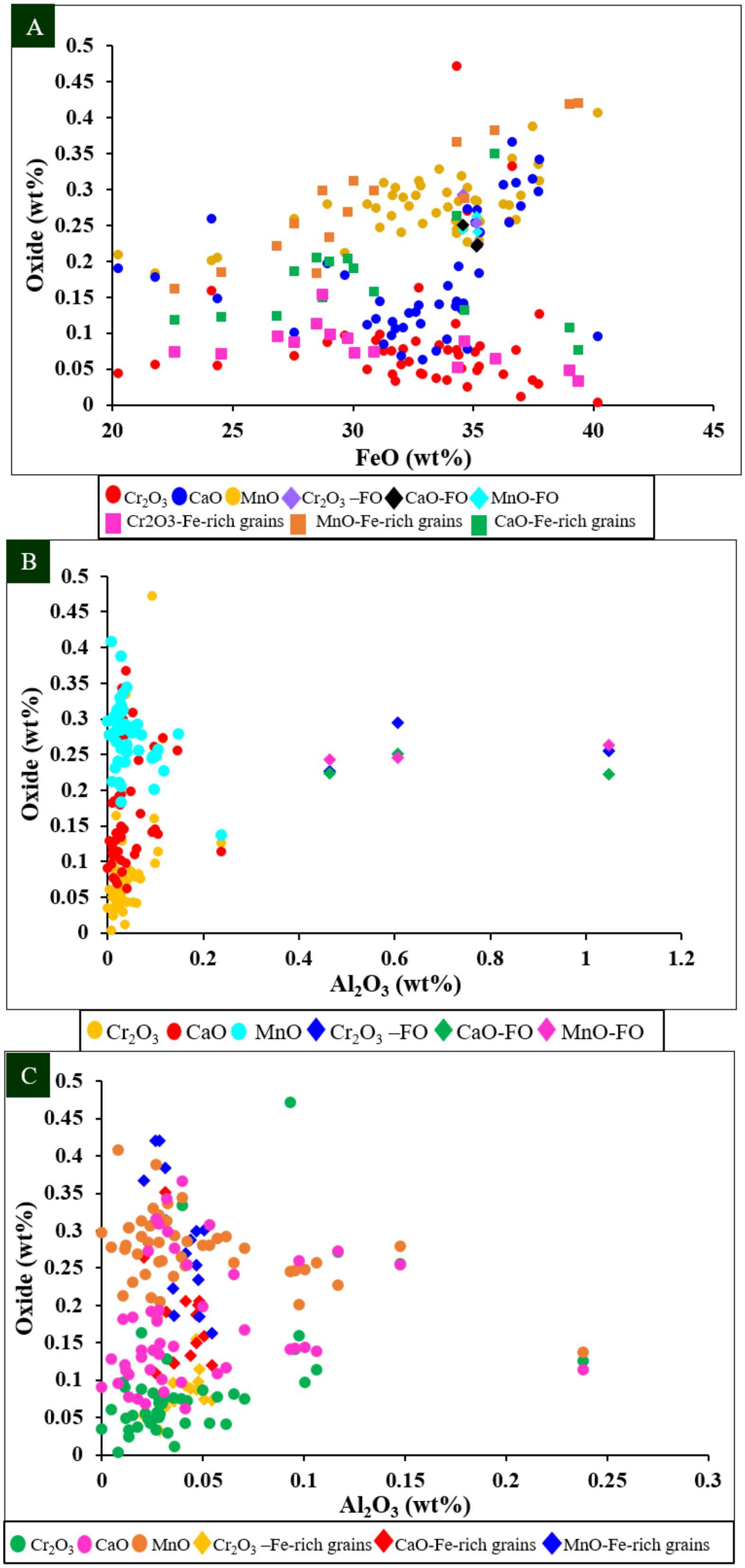

Figure 41: (A) A variation diagram of oxide contents (wt%) versus FeO contents (wt%) of compiled analyses for the LI type IIA chondrule olivine phenocrysts, the chondrule olivine ferroan overgrowths, and the Fe-rich isolated olivine grains. (B) A variation diagram of oxide contents (wt%) versus Al_2O_3 contents (wt%) of compiled analyses for the LI type IIA chondrule olivine phenocrysts. (C) A variation diagram of oxide contents (wt%) versus Al_2O_3 contents (wt%) of compiled analyses for the type IIA chondrule olivine phenocrysts and the Fe-rich isolated olivine grains.

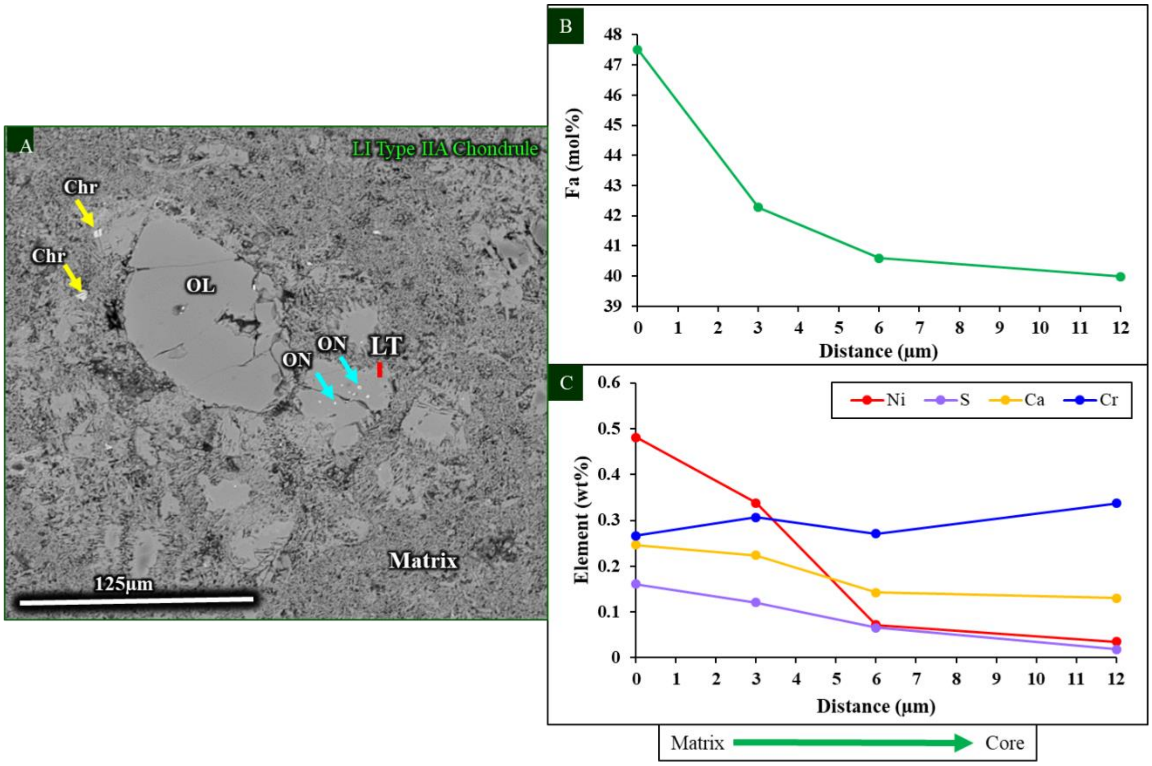

Figure 42: (A) BSE image of a type IIA chondrule olivine phenocryst in the LI. A 15 µm EPMA linear traverse, with a 3 µm step size, was taken from the matrix into the interior of the chondrule phenocryst (indicated by the red line and labeled "LT") using a 1 µm beam size. The traverse began in the matrix, extended through the ferroan overgrowths, and into the interior of the chondrule olivine phenocryst (labeled OL). Small chromite grains on the exterior of the chondrule olivine phenocryst are indicated with yellow arrows and labeled "Chr". Remaining opaque nodules within the phenocryst are indicated by the light blue arrow and labeled "ON". B-D) The profiles start in the matrix (0 µm) and end within the interior of the chondrule olivine phenocryst (indicated by the green arrow at the bottom of the profiles). The first point of the profile is the only one to analyze the ferroan overgrowth of this type IIA chondrule olivine phenocryst. The remaining analyses represent the interior region of the phenocryst. On all of the profiles the analysis at 9 µm was that of an inclusion phase and was left out. B) Fa (mol%) vs. distance in microns. C) Ni, Al, Cr (element wt%) vs. distance in microns. D) Ti, Na, K, S, and Mn (element wt%) vs. distance.

3.2.2.ii. Matrix material & fine-grained chondrule rims: Bulk Compositional Relationships

Broad beam analyses (50 µm beam size) were obtained of matrix material and fine-grained chondrule rims within the LI. Representative bulk matrix analyses are reported in Table 15 and Table 16. As seen in Figure 28f, the LI matrix and the fine-grained chondrule rims have a very narrow range of Fe contents (25-35 wt% Fe), which is similar to that of the host matrix. Figure 43 shows the minor element relationships for the LI matrix and the LI fine-grained chondrule rims. While there are no systematic correlations for any of the elements with increasing FeO content, the minor elements for both the LI matrix and fine-grained chondrule rims are within the same range (Table 1). The MnO contents for both fine-grained materials remains below 0.5 wt%, as FeO content increases. The range of Cr_2O_3 contents for the fine-grained chondrule rims is distinctly less than the matrix; matrix Cr_2O_3 contents reach as a high as 2 wt% when FeO contents are around 34-36 wt%, whereas the maximum Cr_2O_3 contents in the chondrule rims is ~1 wt%. The CaO for both fine-grained materials show relatively similar ranges with the lower FeO contents.

The refractory elements also show no distinct correlations with increasing Al_2O_3 contents (Figure 43b). The majority of the bulk compositions of these minor elements cluster between <0.5-3 wt% Al_2O_3 and the matrix and fine-grained chondrule rims have similar compositional ranges for all the minor elements. The TiO_2 contents below 0.5 wt% as Al_2O_3 increases. The CaO data for the matrix exhibit more scattering than the fine-grained rims, but the majority of the data points contain <1 wt% CaO. The Cr_2O_3 data follow a similar pattern with a maximum value of 2 wt% Cr_2O_3.

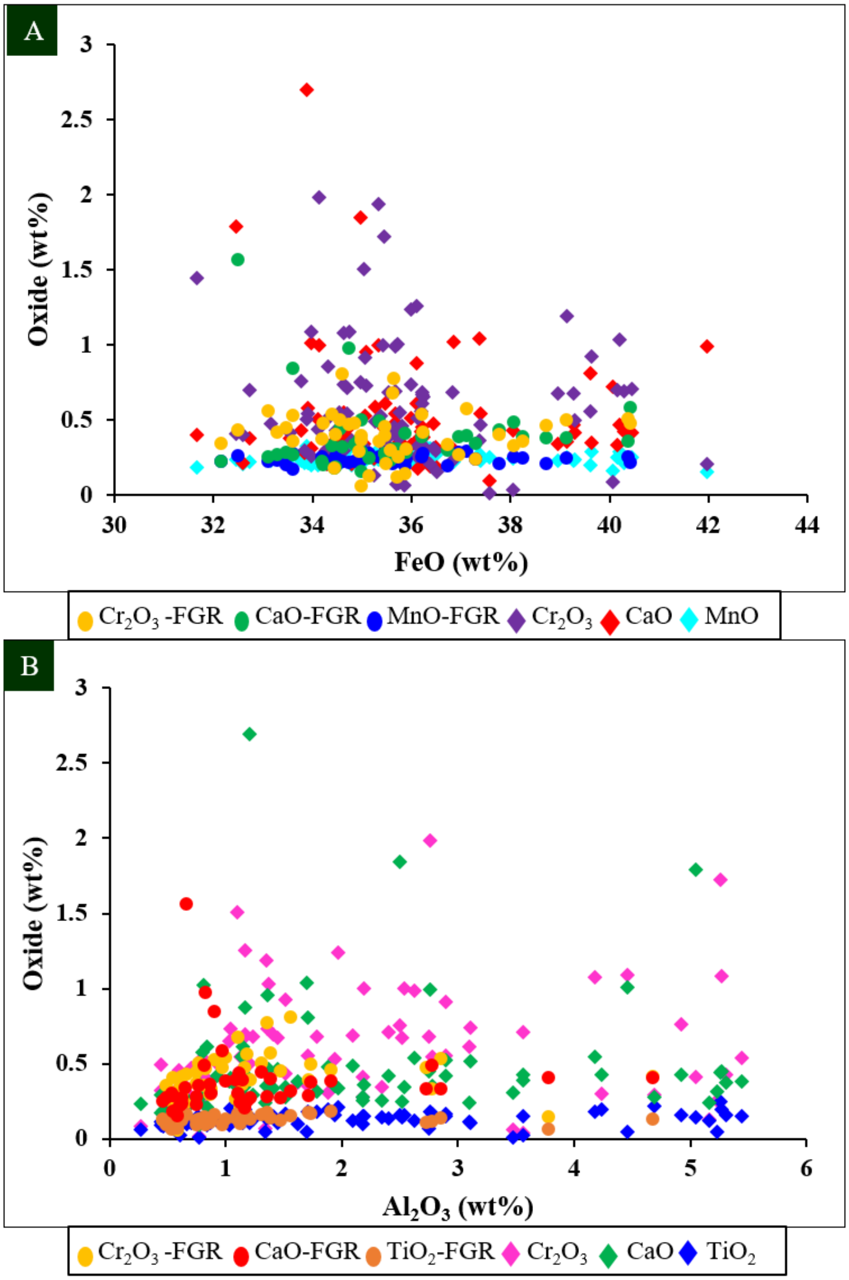

Figure 43: These analyses for the LI matrix and LI chondrule fine-grained rims were obtained using a 50 µm beam size and thus reflect compositions of bulk matrix material and not individual mineral phases. (A) A variation diagram of oxide contents (wt%) versus FeO contents (wt%) for the LI matrix material and chondrule fine-grained rim material. (B) A variation diagram of oxide contents (wt%) versus Al_2O_3 contents (wt%) for the LI matrix material and chondrule fine-grained rim material.

Table 15: Representative electron microprobe broad beam (50 µm beam size) analyses of bulk matrix material from the LI.

Oxide (wt%)													
SiO_2	TiO_2	Al_2O_3	Cr_2O_3	FeO	MnO	MgO	CaO	Na_2O	K_2O	NiO	S	P_2O_5	TOTAL
34.98	0.11	0.81	0.23	36.85	0.22	24.14	1.02	0.09	0.03	0.32	0.19	0.37	99.64
32.55	0.12	1.13	0.47	37.40	0.23	21.11	0.54	0.07	0.05	0.27	0.09	0.31	94.47
26.84	0.09	1.03	0.65	36.24	0.21	18.72	0.38	0.07	0.03	1.64	0.18	0.42	86.77
33.39	0.08	0.51	0.30	34.28	0.24	22.46	0.20	0.07	0.01	0.42	0.13	0.15	92.46
28.44	0.10	0.70	0.47	33.15	0.23	20.78	0.24	0.07	0.01	0.63	0.09	0.17	85.20
32.22	0.10	0.67	0.31	35.07	0.23	21.99	0.27	0.07	0.02	0.68	0.08	0.20	92.02
29.46	0.09	0.84	0.40	32.59	0.20	21.57	0.21	0.06	0.01	0.77	0.17	0.17	86.82
32.43	0.13	1.13	0.55	34.53	0.21	22.84	0.31	0.07	0.02	0.98	0.10	0.23	93.66
29.20	0.10	1.62	0.38	35.75	0.24	21.74	0.38	0.07	0.01	1.06	0.06	0.42	91.11
30.12	0.10	1.15	0.26	36.10	0.27	22.46	0.61	0.09	0.03	0.96	0.08	0.52	92.88

Table 16: Representative electron microprobe broad beam (50 µm beam size) analyses of fine-grained chondrule rims.

Oxide (wt%)													
SiO_2	TiO_2	Al_2O_3	Cr_2O_3	FeO	MnO	MgO	CaO	Na_2O	K_2O	NiO	S	P_2O_5	TOTAL
32.91	0.07	0.54	0.12	35.71	0.22	27.76	0.30	0.10	0.03	0.53	0.07	0.26	98.71
31.49	0.17	0.54	0.41	34.46	0.25	25.87	0.19	0.03	0.01	0.56	0.14	0.24	94.55
30.40	0.16	0.66	0.43	32.49	0.26	24.27	1.57	0.05	0.02	0.37	0.08	1.00	91.88
31.40	0.13	0.74	0.45	33.46	0.20	26.07	0.28	0.05	0.01	0.58	0.10	0.26	93.88
32.07	0.12	0.57	0.18	34.44	0.24	25.06	0.18	0.01	0.00	0.72	0.16	0.20	94.19
29.63	0.18	1.90	0.46	38.72	0.21	20.93	0.38	0.05	0.02	1.06	0.18	0.45	94.45
31.13	0.15	1.14	0.36	38.25	0.25	23.50	0.39	0.03	0.04	1.69	0.16	0.38	97.70
26.00	0.14	0.62	0.42	33.28	0.23	21.16	0.27	0.04	b.d.	0.45	0.11	0.27	83.17
29.30	0.13	1.21	0.40	35.45	0.29	26.44	0.28	0.03	0.02	0.48	0.14	0.11	94.48
28.55	0.13	0.46	0.13	35.13	0.28	27.59	0.25	0.06	b.d.	0.19	b.d.	0.13	92.89

3.2.2.iii. LI chondrule and matrix minor phases: Spinels

Based on the Al X-ray maps (Figure 22), there is relatively high abundance of Al-bearing phases within the LI. Electron microprobe analyses of several of these larger Al-bearing phases were collected using a 1 µm beam size (Figure 21d). These analyses indicate the main Al-rich phase is hercynitic spinel; representative analyses are reported in Table 19. Hercynitic spinel was also found within one of the CAIs in the LI (Figure 11). Representative electron microprobe analyses (taken with a 1 µm beam size) of these are also listed in Table 18. The hercynitic spinels found within the matrix appear to be more iron-rich ($Her_{37.87}$- $Her_{50.68}$) than those in the altered CAI.

Table 17: Representative electron microprobe analyses of orthopyroxene from the isolated pyroxene grain found in the LI matrix. This analysis was taken with a 50µm beam size, but the grain was about 75 µm across.

Oxide (wt%)													
SiO_2	TiO_2	Al_2O_3	Cr_2O_3	FeO	MnO	MgO	CaO	Na_2O	K_2O	NiO	S	P_2O_5	TOTAL
54.26	0.03	0.14	0.53	18.43	0.17	26.63	0.23	b.d.	0.01	0.03	b.d.	b.d.	100.46

Number of cations per 6 Oxygen anions														
Si	Ti	Al	Cr	Fe	Mn	Mg	Ca	Na	K	Ni	S	P	Sum	Fs (mol%)
1.973	0.001	0.006	0.015	0.560	0.005	1.444	0.009	b.d.	b.d	0.001	b.d.	b.d.	4.015	27.800

Table 18: Representative electron microprobe analyses of spinel grains in the matrix and a CAI in the LI with formulae calculated on the basis of [4] oxygen atoms. The shaded analyses are electron microprobe analyses of spinel in an altered CAI in the LI. All analyses taken with a 1 µm beam size.

Oxide (wt%)													
SiO_2	TiO_2	Al_2O_3	Cr_2O_3	FeO	MnO	MgO	CaO	Na_2O	K_2O	NiO	S	P_2O_5	TOTAL
0.10	0.26	62.07	7.23	17.41	0.10	16.05	0.03	0.02	0.01	0.02	b.d.	0.03	103.34
0.16	0.21	64.20	0.15	22.43	0.06	12.25	0.08	0.03	b.d.	0.01	NA	NA	99.60
0.88	0.66	64.36	0.13	15.92	0.03	17.26	0.75	0.01	b.d.	0.05	NA	NA	100.06
0.03	0.14	64.60	0.20	17.98	0.02	16.38	0.05	0.03	b.d.	b.d.	NA	NA	99.44
0.02	0.28	66.91	0.11	13.67	0.03	19.19	0.03	b.d.	b.d.	0.05	NA	NA	100.30

Number of cations per 4 Oxygen anions														
Si	Ti	Al	Cr	Fe	Mn	Mg	Ca	Na	K	Ni	S	P	Sum	Hercynite (mol%)
0.003	0.005	1.857	0.145	0.370	0.002	0.607	0.001	0.001	b.d.	b.d.	b.d.	0.001	2.991	37.84
0.004	0.004	1.997	0.003	0.495	0.001	0.482	0.002	0.002	b.d	b.d.	NA	NA	2.992	50.68
0.022	0.013	1.937	0.003	0.340	0.001	0.657	0.021	0.001	b.d	0.001	NA	NA	2.995	34.10
0.001	0.003	1.974	0.004	0.390	b.d.	0.633	0.001	0.002	b.d	b.d	NA	NA	3.008	38.11
0.001	0.005	1.983	0.002	0.288	0.001	0.720	0.001	b.d	b.d.	0.001	NA	NA	3.001	28.55

3.2.3. LI-Host Interface: Bulk Composition Relationships

The last area of interest is the contact between the LI and the host chondrite. This region is extremely porous and consists of fine-grained, elongate olivines with intermixed with other phases. Even though EPMA analyses were performed with a 1 μm sized beam the totals for these analyses are all poor with an exception of two data points. Representative analyses of olivine grains from this region are reported in Table 19. Due to the porous and fine-grained nature of this region, the elemental profiles across this interface are present as ratios to Si.

An EPMA traverse was taken across this interface along the upper right hand side of the LI and host boundary. (Figure 44a-e) in order to determine any compositional variations across the LI and host boundary. The profile begins within the host meteorite matrix, crosses the narrow high-Z zone at the boundary between the host and clast, and moves into the LI matrix. The first 10 μm the Mg/Si ratio is variable and changes by almost a value of 1, whereas the Fe/Si ratio remains quite constant. At the high-Z zone between 35 and 50 microns, the Fe/Si ratio peaks before decreasing slightly over the remaining 50 microns into the LI. The Al/Si, Na/Si, Ca/Si, and K/Si ratios also all peak at the same high-Z point in the traverse as Fe/Si, but S/Si and Ni/Si show no evidence of increasing at the interface.

Table 19: Representative electron microprobe analyses of the fine-grained, porous LI-Host interface with formulae calculated on the basis of [4] oxygen atoms. The analyses in green are examples of the best analyses of elongate ferroan olivine grains obtained within this region. These analyses were obtained using a 1 µm beam size.

Oxide (wt%)

SiO_2	TiO_2	Al_2O_3	Cr_2O_3	FeO	MnO	MgO	CaO	Na_2O	K_2O	NiO	S	P_2O_5	TOTAL
34.97	0.08	0.49	0.26	36.94	0.23	24.54	0.26	0.04	0.01	0.24	0.37	0.08	98.52
34.98	0.11	0.81	0.23	36.85	0.22	24.14	1.02	0.09	0.03	0.32	0.46	0.37	99.64
33.39	0.08	0.51	0.30	34.28	0.24	22.46	0.20	0.07	0.01	0.42	0.32	0.15	92.46
32.22	0.10	0.67	0.31	35.07	0.23	21.99	0.27	0.07	0.02	0.68	0.19	0.20	92.02
30.63	0.14	0.87	0.73	36.47	0.24	23.82	0.26	0.08	0.02	0.33	0.23	0.10	93.91
31.90	0.17	2.05	0.58	37.21	0.19	20.91	0.34	0.08	0.02	0.36	0.25	0.19	94.26
29.70	0.15	1.16	0.48	36.49	0.24	19.96	0.28	0.06	0.02	0.49	0.70	0.15	89.87
30.30	0.14	2.81	0.79	37.09	0.20	20.85	0.39	0.08	0.04	0.43	0.42	0.19	93.75

Number of cations per 4 Oxygen anions

Si	Ti	Al	Cr	Fe	Mn	Mg	Ca	Na	K	Ni	S	P	Sum	Fa (mol%)
0.996	0.002	0.016	0.006	0.880	0.006	1.042	0.008	0.002	b.d.	0.005	0.008	0.002	2.974	45.781
0.985	0.002	0.027	0.005	0.867	0.005	1.013	0.031	0.005	0.001	0.007	0.010	0.009	2.967	46.130
1.010	0.002	0.018	0.007	0.867	0.006	1.013	0.007	0.004	0.001	0.010	0.007	0.004	2.957	46.125
0.990	0.002	0.024	0.008	0.901	0.006	1.007	0.009	0.004	0.001	0.017	0.004	0.005	2.978	47.215
0.932	0.003	0.031	0.017	0.928	0.006	1.081	0.008	0.005	0.001	0.008	0.005	0.003	3.029	46.199
0.963	0.004	0.073	0.014	0.939	0.005	0.941	0.011	0.005	0.001	0.009	0.006	0.005	2.974	49.961
0.948	0.004	0.044	0.012	0.974	0.006	0.949	0.010	0.004	0.001	0.012	0.017	0.004	2.984	50.634
0.924	0.003	0.101	0.019	0.946	0.005	0.948	0.013	0.005	0.002	0.011	0.010	0.005	2.989	49.945

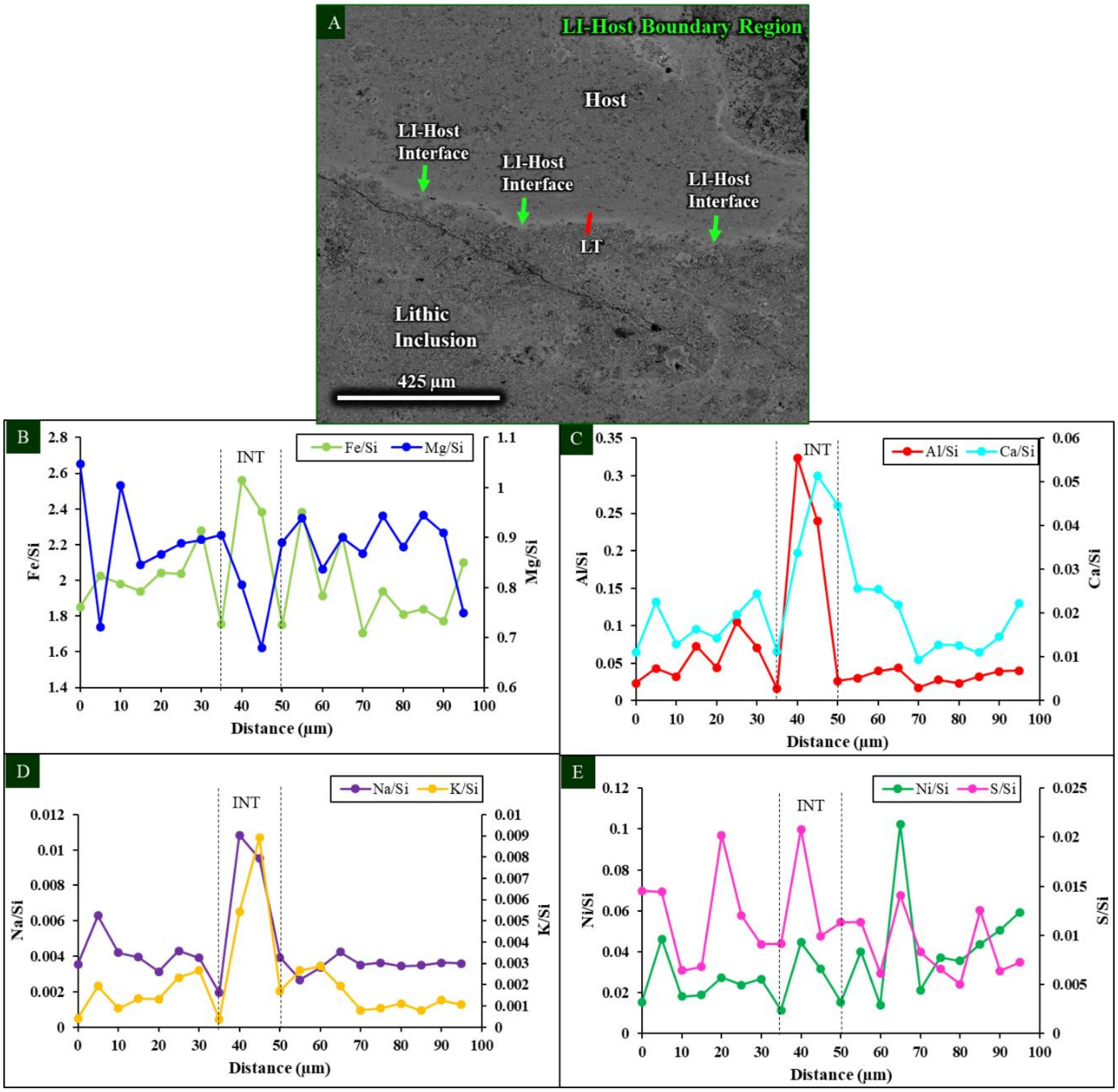

Figure 44: Compositional traverse across a region of the LI-Host interface with a 1 µm beam size. (A) A 100 µm linear traverse, with a 5 µm step size, was taken starting from the host matrix, passing through the interface, and into the LI matrix (indicated by the red line and labeled "LT"). The interface is indicated on the figure with green arrows and labeled "LI-Host Interface". B-D) Due to the fine-grained nature of the matrix material all the profiles are represented as elemental rations over Si. On all the profiles the dashed black line indicates the location of the interface and this region is labeled "INT". (B) Mg/Si and Fe/Si versus distance (µm). (C) Al/Si and Ca/Si versus distance (µm). (D) Na/Si and K/Si versus distance (µm). (E) Ni/Si and S/Si versus distance (µm).

3.3. Oxygen Isotope Composition

The regions sampled for oxygen isotope analyses were taken from the host chondrite, the LI, and a fragment from the fine-grained rim region between the host and the LI. The host and LI samples are taken to represent their bulk oxygen isotopic compositions.

Table 20 reports the oxygen isotopic composition of the host, LI, and rim. All values are in terms of per mil, V-SMOW. None of the samples has an oxygen isotopic composition that lies on the Carbonaceous Chondrite Anhydrous Mineral (CCAM) line. Instead, all the data lie to the right of the CCAM line (Figure 45). The two analyses from the host lie separated from one another with approximately a 2 ‰ difference in $\delta^{18}O$. The compositions of the LI and its rim composition lie between the two bulk host oxygen isotopic compositions. Compared with other CV3s and their dark inclusions (Figure 46), all the NWA 2364 samples lie among the more aqueously-altered CV3s such as Bali and a dark inclusion LV1 from Leoville. The host isotopic compositions are more displaced from the CCAM line than any other CV3 chondrite bulk oxygen composition. They both lie on the same mixing line defined by the compositions of dark inclusions in the reduced CV3 chondrites, Leoville and Vigarano. The host compositions are also very similar to those of the LI and rim compositions.

Table 20: Oxygen isotopic analyses data for NWA 2364 of two host chondrite samples, one LI sample and one sample from the rim around the LI.

Northwest Africa NWA 2364_{OxA} Samples				
	Weight (mg)	$\delta^{17}O$(‰)	$\delta^{18}O$(‰)	$\Delta^{17}O$(‰)
Host 1	1.3	-0.414	5.121	-3.118
Host 2	1.1	1.232	7.310	-2.628
Rim 1-4	1.6	0.416	5.768	-2.630
LI 1	2	0.988	6.474	-2.430

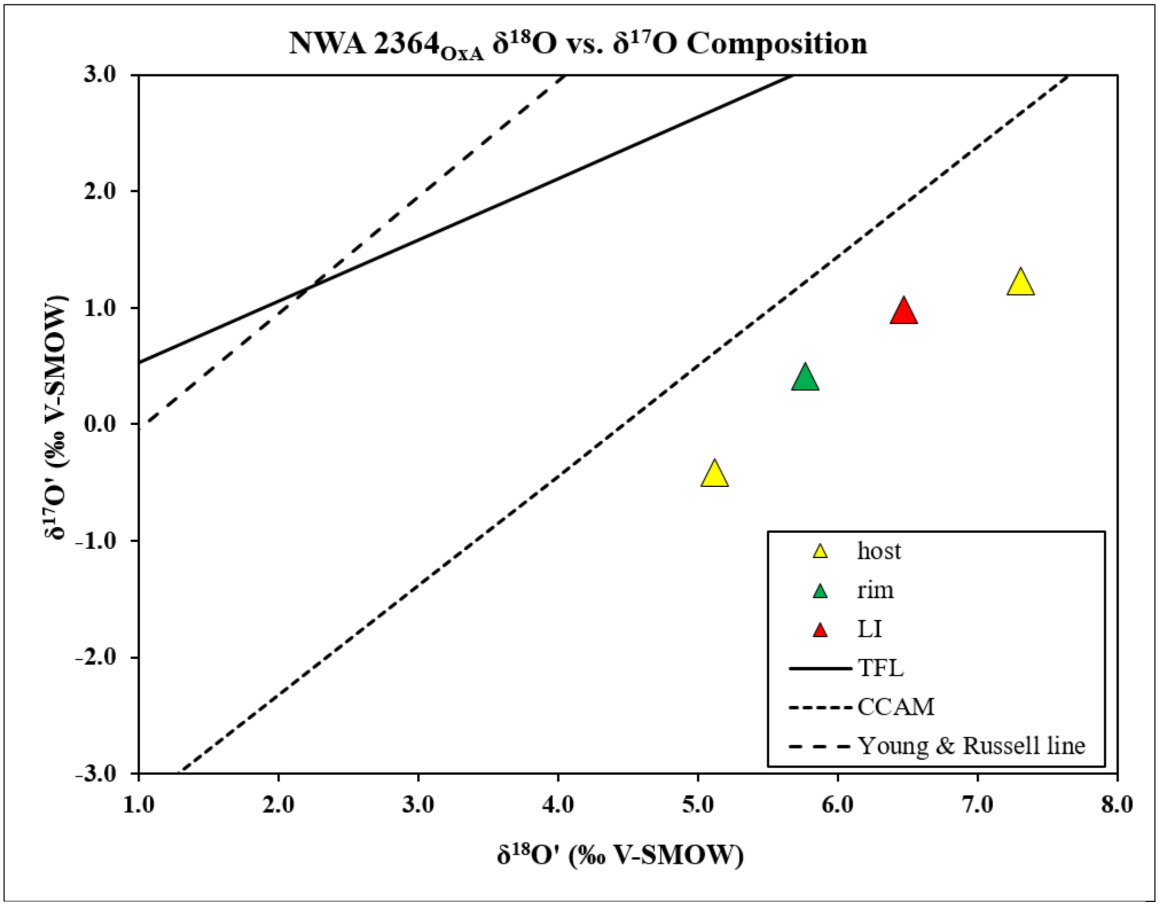

Figure 45: The NWA 2364 host, LI, and rim oxygen isotopic compositions plotted on an oxygen three-isotope diagram along with the Carbonaceous Chondrite Anhydrous Line (CCAM), the Young & Russell line, and the Terrestrial Fractionation Line (TFL). All four samples are displaced from the CCAM line and exhibit heavy isotope enrichments.

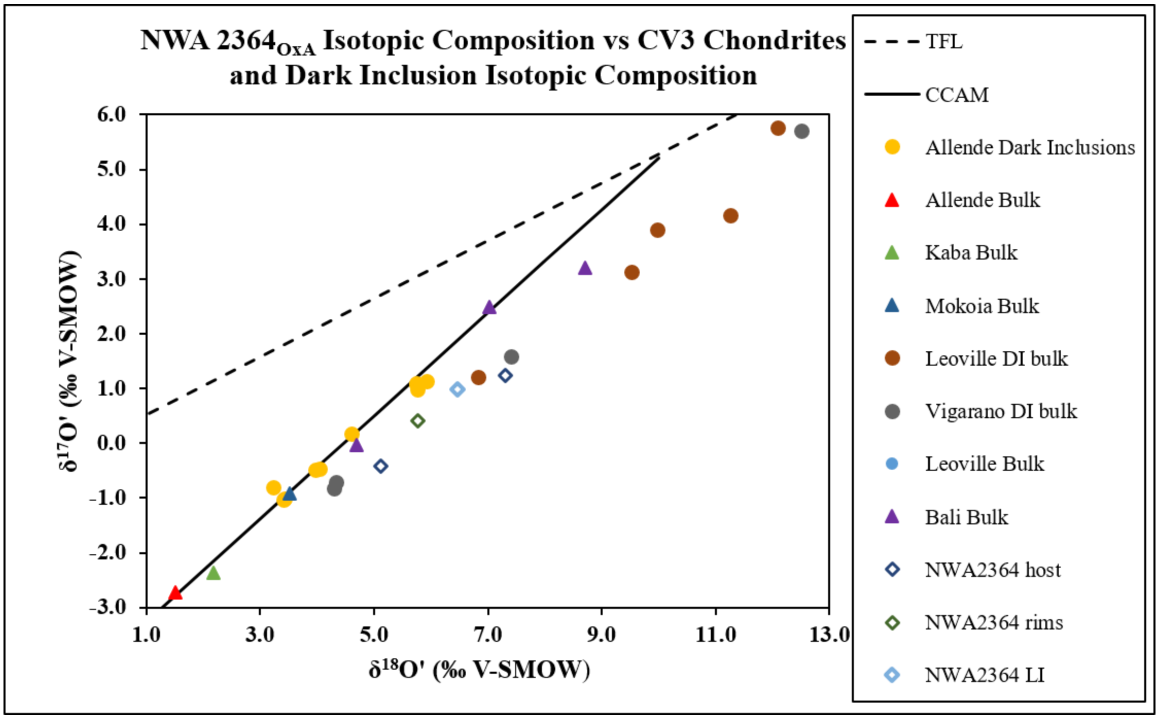

Figure 46: A compilation of the data from NWA 2364 compared with the bulk oxygen isotopic data for oxidized and reduced CV3 chondrites and their dark inclusions. Allende and Bali are from the oxidized CV3 chondrite subgroup while Leoville, Efremovka, and Leoville are from the CV3 chondrite reduced group. Data compiled from Keller et al. (1994); Kracher et al. (1985); Johnson et al. (1990); Bischoff et al. (1988); Clayton et al. (1997); Krot et al. (1997).

4. Discussion

The CV3 chondrites are a very complex group of meteorites. In addition to their nebular record of processes in the protoplanetary disk, they also show significant evidence of thermal metamorphism and alteration, which appears to have involved a fluid. These secondary processes have modified the primary characteristics of the meteorites to differing degrees. Similar alteration processes have also affected their dark inclusions and often to a greater extent. Unraveling these complex processes is challenging, because the effects of aqueous alteration and thermal metamorphism are superimposed on one another. The effects of metamorphic equilibration of mineral compositions, obscures the earlier alteration history of the rock, observations that are seen in chondritic components in the Allende-like CV3 chondrites and their dark inclusions. In this discussion, we examine the evidence for both types of alteration processes, i.e., aqueous alteration and thermal metamorphism in the NWA 2364 host and LI. We first present a brief overview of dark inclusions in CV3 chondrites to provide a context for the following discussion. We then discuss the alteration features in the NWA 2364 LI compared to other type A/B dark inclusions. We also compare the alteration features in the NWA 2364 host to those found in the Allende CV3 chondrite. Finally, we provide a synthesis of the evidence to develop a plausible evolutionary history for the NWA 2364 CV3 chondrite and its LI.

4.1. Dark Inclusions in CV3 chondrites: A brief overview

Previous work on CV3 chondrites has shown that they exhibit different alteration styles. CV3 chondrites also contain different types of dark inclusions that also show a variety of alteration features. The oxidized CV3 chondrite, Allende, and its dark inclusions, have been studied the most extensively, due to the large quantity of material recovered from this meteorite fall. Dark inclusions in other CV chondrites have been studied in detail, but because of the more limited amount of material for study, fewer inclusions have been studied than in Allende. Type A/B dark inclusions from Leoville, Vigarano, and Efremovka have been reported by various authors, e.g. (Kracher et al., 1985; Johnson et al., 1990; Kojima and Tomeoka, 1993, 1994, 1995, 1996; Krot et al., 1999).

Allende dark inclusions often resemble Allende in terms of chondritic components and similar secondary mineralogy, but show more extensive alteration and replacement of primary features. The type A/B dark inclusions found in Allende texturally have small chondrules, both Mg-rich type IA and rarer FeO-rich type IIAs, some remnant CAIs, isolated forsteritic and fayalitic olivine grains, fine-grained chondrule rims, chondrule pseudomorphs, and a very fine-grained matrix that is primarily made up of elongate olivines (Kurat et al., 1989; Johnson et al., 1990; Kojima and Tomeoka, 1994, 1996; Buchanan et al., 1997; Krot et al., 1995; Krot et al., 1997; Krot et al., 1998; Krot et al., 1999; Krot et al., 2000). A Leoville dark inclusion, LV2, reported in Johnson et al. (1990) resembles Allende macroscopically and contains chondrule pseudomorphs consisting of platy, elongate ferroan olivine grains, as well as a similar fine-grained matrix consisting of ferroan, elongate olivines with chondrules, and other mineral fragments. The Vigarano dark inclusions studied by Johnson et al. (1990) and Kojima and Tomeoka (1996) have textural and mineralogical characteristics that resemble the Allende and Leoville dark inclusions.

In general, the secondary minerals found within these type A/B Allende dark inclusions are very similar, but there are some variations between samples. Chondrule phenocrysts and isolated grains are typically forsteritic in composition. The widely observed ferroan olivine overgrowths on these forsteritic olivines have an average composition of Fa_{39} (Krot et al., 1997). Sulfide grains occur within the matrix and, in some instances, along the edges of isolated forsterite grains. The fine-grained chondrule rims often are made up of primarily of fine-grained ferroan olivines (micron to a few microns in size) with minor amounts of submicron- to micron-sized nepheline grains. Most of these chondrule rims are depleted in Ca-rich phases. Sodium and calcium have been leached from chondrules during alteration of chondrule mesostasis, and so these elements have been distributed to other regions within the dark inclusions. Other secondary phases such as sulfides, magnetite, sodalite, wollastonite, andradite, hedenbergite, diopside, and salitic pyroxene are often found within the matrix of the Allende dark inclusions. The type A/B dark inclusions in Leoville, Vigarano, and Efremovka are very similar in terms of mineralogy to those found in Allende.

A striking feature found in type A/B Allende dark inclusions is the presence of distinct, fine-grained rims that surround them. Similar rims have also been reported around type A and type B dark inclusions. These rims were first reported by Johnson et al. (1990), but have not been analyzed in detail with the exception of a study by Krot et al. (2000). The authors found that the rims consist of several distinct mineralogical zones. The inner zone of the rim consists of diopside-salitic pyroxenes (Fs_{10-15}, Wo_{48-50}) followed by a central zone of hedenbergite (Fs_{45-50}, Wo_{48-50}), wollastonite, and andradite, with textural evidence of replacement of andradite by wollastonite and hedenbergite. The outermost zone of these rims consists of salite-hedenbergite pyroxenes (Fs_{15-35}, Wo_{48-50}) intergrown with platy, ferroan olivine. While the occurrences of these rims have been best studied from Allende dark inclusions, they have also been reported surrounding Efremovka dark inclusions, E39 and E80 (Krot et al., 1999). However, the Efremovka rims are poorly developed, discontinuous, and thought to be made of kirschsteinite, compared with the thicker, zoned, multi-mineralic rims on Allende dark inclusions.

While the dark inclusions in reduced and oxidized CV chondrites mostly share similar alteration textures and minerals with some degree of variation, there is a difference in their oxygen isotopic compositions. Dark inclusions in reduced CV3 chondrites are enriched in the heavier oxygen isotope and are typically displaced to the right of the CCAM line (Figure 46). Their host chondrites typically fall along the CCAM line with little to no displacement from it, but their positions on the CCAM line vary (Figure 46). In contrast, the bulk oxygen isotopic composition of Allende and its dark inclusions invariably plot along the CCAM line, but the dark inclusions consistently have lower $\Delta^{17}O$ values. The dark inclusions from Leoville, Vigarano, and Efremovka all plot near the CM chondrite field, indicating they have been aqueously altered to a greater extent than their host chondrites. However, although these ^{17}O-enriched compositions are indicative of aqueous alteration, there is minimal evidence of hydrous phases in these dark inclusions. Instead the dark inclusions are dominated by anhydrous secondary phases, suggesting that either they have experienced fluid-rock interactions at temperatures above the stability of hydrous phases or alternatively may have experienced metamorphic dehydration (Clayton and Mayeda, 1999). These bulk analyses represent primary nebular isotopic compositions of original phases and the material that has been altered by aqueous fluids.

4.2. LI alteration vs. CV3 dark inclusion alteration

In this section we compare the alteration features found in the LI of NWA 2364 and discuss some significant characteristics that are distinct from previous descriptions of dark inclusions in CV3 chondrites. Here we call the dark inclusion found within the CV3 oxidized, Allende-like NWA 2364, a lithic inclusion (LI) because optically it is lighter in appearance compared to typical dark inclusions found within the CV3 chondrites. Based on previous work, although the inclusion in NWA 2364 is lighter in color, it still has the petrologic characteristics that are consistent with a type A/B dark inclusion. In general, the mineralogy and textures of the LI are very similar to Allende, Leoville, Vigarano, and Efremovka type A/B dark inclusions that have been described in the literature. The LI in NWA 2364 is primarily made up of chondrules and CAIs with smaller sizes than the NWA 2364 host, isolated grains, and a high abundance of fine-grained matrix, all typical characteristics of type A/B dark inclusions. The LI is surrounded by a fine-grained rim that is texturally distinct from the LI matrix (Figures 1-3). The matrix of the LI is dominated by fine-grained, elongate ferroan olivines, typical of other dark inclusions. Minor phases are distributed throughout the matrix, the most abundant of these being porous aggregates of Ca-rich pyroxene grains that are nearly identical to those found in the Allende dark inclusion, IV-I (Krot et al., 2000). The chondrules are dominantly porphyritic forsterite-rich type IAs and are altered to varying degrees.

As discussed in the results section, several distinct lines of evidence for alteration are present, including ferroan overgrowths on forsteritic olivine grains ranging in composition from $Fa_{37.9}$-$Fa_{44.72}$. Larger and coarser-grained chondrules are still recognizable with the LI, but smaller chondrules have been entirely pseudomorphed by aggregates of elongate, ferroan olivines (Figure 14). Low Ca-pyroxene and mesostasis is absent in all the chondrules in the LI; both have been replaced by platy, ferroan olivine grains. Chondrule phenocrysts have enrichments in iron along fractures and cracks, and most opaque nodules (formally metal grains) have also been replaced by ferroan olivine grains. Chondrules and chondrule pseudomorphs often have a distinct, but not continuous, rim of Ca-rich pyroxene aggregates that occur outside the fine-grained rims. All these features are ones that the LI shares in common with many dark inclusions from Allende, and are the lines of evidence that overall, suggest that there are similarities in their alteration histories.

4.2.1. Major Differences and Unique Findings

Although, as documented above, there are notable similarities in the mineralogy of the NWA 2364 LI to other CV dark inclusions, there are notable differences, which suggest that its alteration history was different. A significant difference is the absence of specific mineral phases that are commonly found in almost all other dark inclusions. Specifically, several different studies (e.g. Krot et al. 1998; Krot et al. 2000) have reported the presence of andradite, wollastonite, and grossular within dark inclusion Ca-Fe nodules and Ca-Fe-Mg-rich pyroxene aggregates and as part of the Ca-rich rims around the dark inclusions. None of these phases are present either within the Ca-rich pyroxene aggregates or within the rim along the NWA 2364 LI and host. There is no evidence of a mineralogical zonation in the rim around the LI; instead the rim is comprised of aggregates, a few tens of microns in size of diopside-hedenbergite solid solutions with a range in compositions, interspersed with ferroan olivines that extend into the host.

A further important and major difference between the NWA 2364 LI and Allende dark inclusions is the absence or rarity of Na, K, or Cl-bearing phases such as nepheline or sodalite. Sulfides are also absent from chondrules and the matrix of the LI. The dearth of these phases in the LI is readily apparent in Figures 47& 48 (Fe, S, Mg map and Al, Ca, Na map are X ray elemental maps that portray the lack of Na and S in the LI).

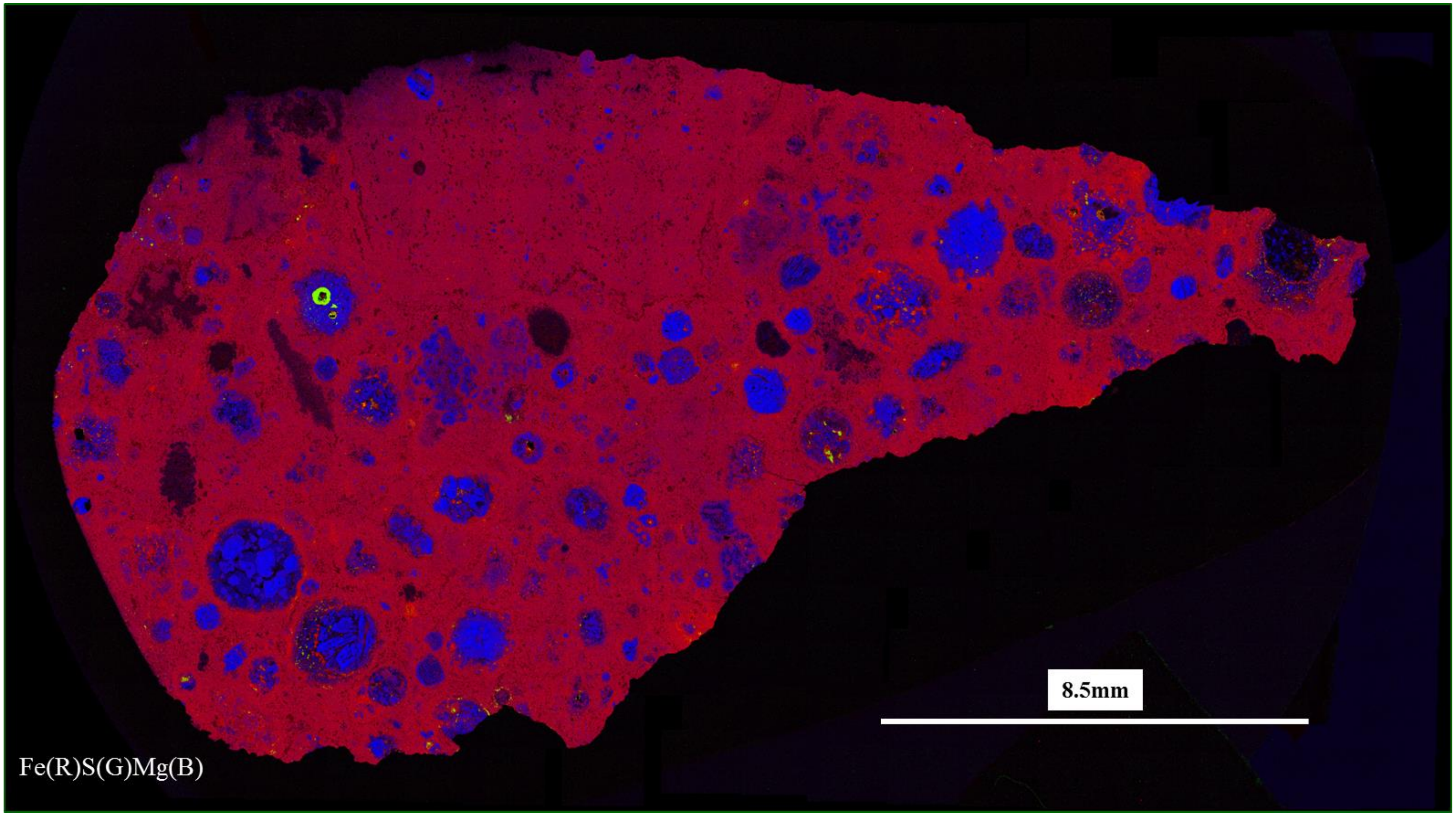

Figure 47: Composite Fe(R)S(G)Mg(B) X-ray map of NWA 2364 and its LI. As seen in this figure there is a stark absence in the sulfur content in both the host and the LI but it is more extreme in the LI, where no discernible sulfide grains (yellow or green in the image) are evident.

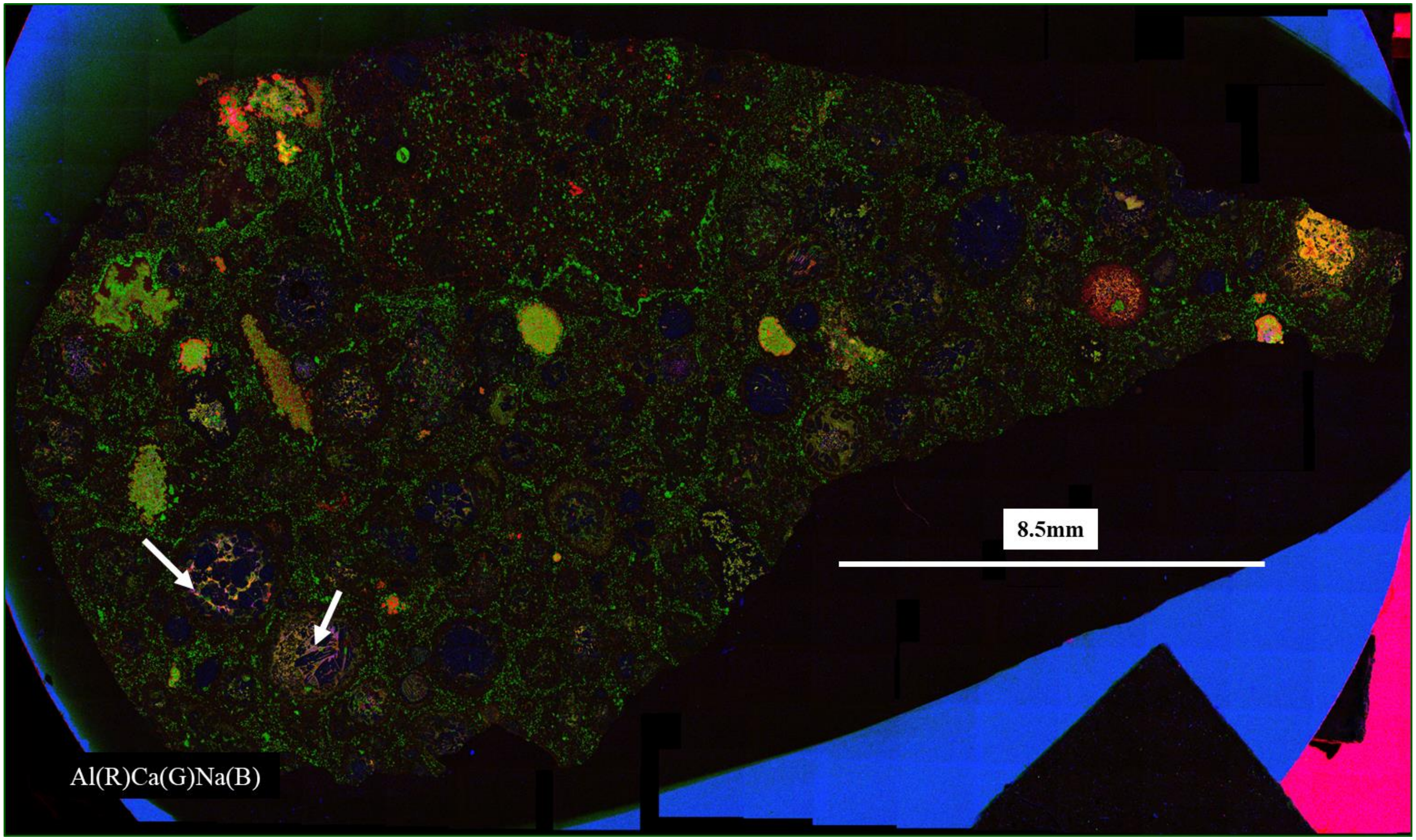

Figure 48: Composite Al(R)Ca(G)Na(B) X-ray map of NWA 2364 and its LI. The LI is completely devoid of Na-bearing phases in the chondrules or matrix material while the host retains some Na within the chondrules (purple mesostasis regions – arrowed in white).

This situation is very different from dark inclusions in Allende or the reduced CV chondrites. In both cases, nepheline and sodalite are common secondary alteration phases of CAIs and chondrule mesostasis in these dark inclusions (Johnson et al., 1990; Krot et al., 1995; Brearley and Jones, 1998; Krot et al., 1998). Similarly, fine-grained sulfides are also commonly present in the matrix material of these dark inclusions. Assuming that the protolith of the NWA 2364 LI was similar to that of other dark inclusions, i.e. was chondritic in character, as seems highly likely, these differences in mineralogy indicate that the alteration history of the NWA 2364 LI was significantly differently than the dark inclusions in Allende, Leoville, Vigarano, and Efremovka.

The CI-normalized elemental abundances for the NWA 2364 LI matrix bulk composition and two Allende dark inclusion matrix bulk compositions (Figure 49a) are consistent with the mineralogical observations. The volatile elements, Na, K, and S are all highly depleted in all three of the dark inclusions, in all cases being <0.2 x CI abundances. The depletions in Na and K are remarkably similar in all three dark inclusions, with NWA 2364 showing a similar depletion to Allende inclusion DI, 5a2 (Buchanan et al., 1997). Sulfur is notably significantly more depleted in NWA 2364 (~0.02 x CI) compared with the two Allende dark inclusions (approx.0.2 x CI). The refractory elements Ti and Mg are close to CI chondrite abundances, but Ca and Al are apparently fractionated with enriched Al (comparable to Allende DIs). Calcium is enriched in the Allende DIs, but in the LI matrix Ca is highly depleted ~0.2 x CI). The LI is more depleted in Ni than both Allende dark inclusions shown in (Figure 49a).

Figure 49b shows the LI plotted relative to bulk CV3 elemental abundances. Compared to bulk CV chondrites, the LI is significantly depleted in Ca, Na, K, Ni and S, but refractory Al, Mg, and Si are very similar to the bulk CV chondrite values as is Si.

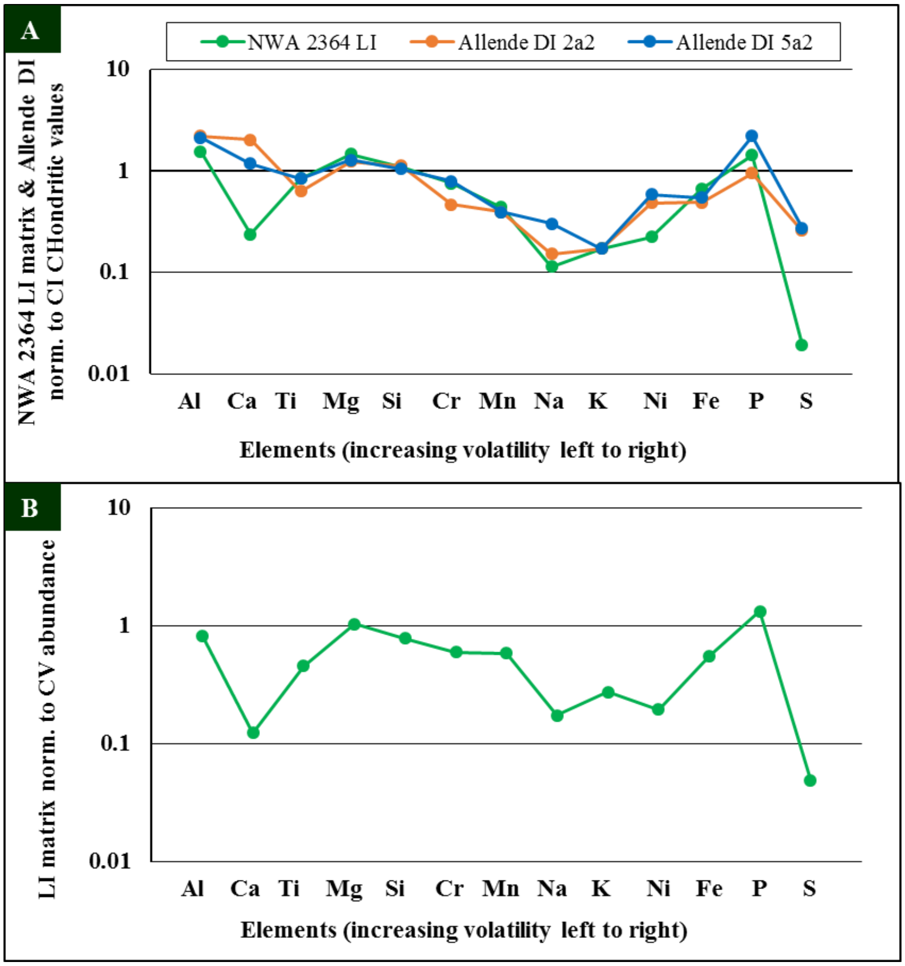

Figure 49: (A) CI abundance plot of bulk matrix compositions of two Allende dark inclusions, as well as the bulk matrix composition of the LI normalized and plotted against CI chondritic values. The Allende, bulk dark inclusion data comes from Buchanan et al. (1997) and the CI abundance data comes from Lodders et al. (2009). (B) CI abundance plot of the bulk matrix composition of the LI normalized and plotted against the bulk CV chondrite values. The CV chondritic values comes from Lodders and Fegley (1998).

In this study, we have observe an additional feature indicative of alteration which has not been reported previously in other CV3 chondrites or their dark inclusions. Although ferroan overgrowths in forsteritic olivines have been widely reported in the literature, in this study, we also find ferroan overgrowths on type IIA chondrule phenocrysts and on isolated grains in the LI. This alteration feature was not observed in the host chondrite, but was found in multiple instances in the LI (e.g. Figures 13, 14, & 16). It is possible that these overgrowths also occur in Allende dark inclusions, but have just not been recognized previously, because the BSE contrast difference between the overgrowths and the phenocrysts is relatively small.

Another significant textural observation from the NWA 2364 LI is the vein and vein filling textures (Figures 17a-j) found within the LI in both the type IA and type IIA chondrules. This type of vein texture has never been described in CV3 dark inclusions before. Veins of Ca-rich salitic pyroxenes and sulfide-rich veins crosscutting Allende dark inclusion matrix material were reported by Krot et al. (2000), whereas the veins in NWA 2364 crosscut individual chondrule olivine phenocrysts. These vein textures resemble alteration in fractures within chondrule phenocrysts in CM chondrites that are filled with serpentines (Hanowski and Brearley, 2001; Velbel et al., 2012; Lee and Lindgren, 2016). Similar vein textures are commonly identified in altered terrestrial olivine phenocrysts in basalts and peridotites, as well (Wicks and Whittaker, 1977; Boudier et al., 2010; Plümper et al., 2016). However, in the case of the LI, the vein fill consists of crystallographically-oriented, elongate ferroan olivine grains, not serpentine. Along the edge of the chondrule phenocryst, adjacent to the vein, the phenocrysts have a serrated appearance, a texture that is commonly attributed to dissolution due to interaction with aqueous fluids (Velbel et al., 2009).

As noted in the results section, the oxygen isotopic composition of the NWA2364 LI is very different from the measured compositions of dark inclusions in Allende. Instead the LI has a composition that is falls on the lower end of a mixing line that is defined by dark inclusions in the reduced CV3 chondrite, Leoville. This large difference from the other oxidized CV3 dark inclusions clearly suggests a different alteration history.

In conclusion, a comparison of the properties of the NWA 2364 LI with dark inclusions in other CV3 chondrites show that it shares some similarities, but importantly has important differences that have not been described previously in any other dark inclusion. These differences show that the LI had a complex history and was altered under different conditions than other dark inclusions.

4.3. Host Chondrite vs Allende

An important observation from previous studies is that dark inclusions show a different style and degree of alteration than the host meteorite that contains them. This observation is especially apparent in studies of dark inclusions in reduced CV chondrites. In Allende, there are some similarities in the types of secondary alteration effects in the dark inclusions and the host, although in detail they are different in part due to the primary characteristics of the dark inclusions versus the host. Most studies have concluded that the alteration histories of the DIs are different from the host meteorite, with a few exceptions (Krot et al. 1999, 2000). Here we compare the alteration features of the NWA 2364 host and Allende. In terms of its primary textural and petrologic characteristics, NWA 2364 is very similar to Allende, consistent with its classification as an oxidized CV3 chondrite. However, in detail there are clearly differences that set NWA 2364 apart from Allende. These differences indicate that NWA 2364 has been altered somewhat differently, from Allende.

Alteration affects have been widely documented in Allende CAIs, chondrules and matrix (Brearley and Krot, 2013). Allende has shown to be more altered and metamorphosed than the rest of the CV3 oxidized and reduced chondrites (Krot et al., 1995; Bonal et al., 2006; Brearley and Krot, 2013). In general, chondrules exhibit secondary replacement of mesostasis to nepheline, sodalite, and ferroan olivines, in some cases. Calcium and Si were removed from the chondrules and CAIs, to form Ca-rich minerals within the matrix. Secondary ferroan olivines also replace Mg-rich, low-Ca pyroxene in chondrules and there are ferroan overgrowths around the Mg-rich chondrule olivine phenocrysts, as well as along fractures within the phenocrysts (Brearley and Krot, 2013). In chondrule opaque nodules, kamacite has been replaced by sulfides, magnetite, carbides, and Ni-rich metal (taenite). CAIs show varying degrees of alteration, but replacement of primary CAI phases such as melilite by a wide variety of secondary phases including andradite, grossular, wollastonite, nepheline, and sodalite has been widely reported in the literatures (see Brearley and Krot, 2013) Within the matrix, magnetite is present, as well as Fe-Ni sulfides, Ni-rich metals in small quantities, and diopside-hedenbergite pyroxenes. Phyllosilicates are present in trace amounts as well (e.g. Brearley, 1997).

Like Allende, in NWA 2364 type IA and rarer type IIA chondrules are altered to varying degrees depending on the primary mineralogy and grain size. Some chondrules have very minor amounts of nepheline and/or sodalite that has replaced chondrule mesostasis, but many of the more extensively-altered chondrules are made up of ferroan olivines. In most cases, the more highly altered chondrules are those that contain low-Ca pyroxene, which has been replaced to a significant degree by fine-grained olivine, as seen in many instances within Allende. Many of the type IA chondrule olivine phenocrysts have prominent ferroan overgrowths, also a common feature in Allende.

4.3.1. Major differences and unique findings

The NWA 2364 host has several differences from Allende. The lower abundance of nepheline and sodalite replacing chondrule mesostasis is a common secondary feature in Allende that is extremely rare in NWA 2364. There are trace amounts present, but the main secondary alteration product of mesostasis is elongate, ferroan olivine. Metal nodules within the majority of chondrules have been altered to ferroan olivine, although a few cases are observed where they have been replaced by Fe-Ni sulfides (Figure 47). Magnetite is also not apparent in the NWA 2364 host chondrules. In Allende, Fe-Ni sulfides, magnetite, and carbides are the main secondary product of the alteration of the metal nodules. Chondrules in NWA 2364 still have fine-grained chondrule rims surrounding chondrules, whereas in Allende these features are less common.

Unlike Allende, no, nepheline, sodalite, grossular, and andradite are not present in the matrix of NWA 2364. The only Ca-rich phases are Ca-rich pyroxene aggregates of diopside-hedenbergite composition. No phyllosilicates have been found and sulfides, which are common in Allende matrix are lacking in NWA 2364 matrix. The matrix material also has small (few microns in size) hercynitic spinel grains heterogeneously present throughout.

In terms elemental compositions, there are a few notable differences between NWA 2364 and Allende. Figure 50a shows the host meteorite average matrix material plotted with averaged matrix material from Allende, normalized to the CI chondritic values. A major difference is the depletion in S in NWA 2364 matrix compared to Allende bulk matrix composition. Sulfur is highly depleted in NWA 2364 (0.02 x CI) whereas the value for Allende matrix is 0.15 x CI. Similarly Na is also more depleted in the host than Allende (0.09 vs. 0.5 x CI). Potassium is slightly enriched in the host matrix compared to Allende and P is slightly depleted. The NWA 2364 host matrix is also depleted in the refractory elements, Al, Ca, and Ti compared to Allende, which is enriched compared to CI chondritic values. The depletion in Ca is likely due to the fact that most of the matrix values taken for the host excluded the Ca-rich pyroxene nodules, which contain the majority of the Ca in the host matrix. All the other elements, Mg, Si, Cr, Mn, Ni and Fe are all very similar to the Allende host matrix. Compared to the bulk CV chondrite abundances, the NWA 2364 host is, in general, depleted in just about every element except for Mg (Figure 50b).

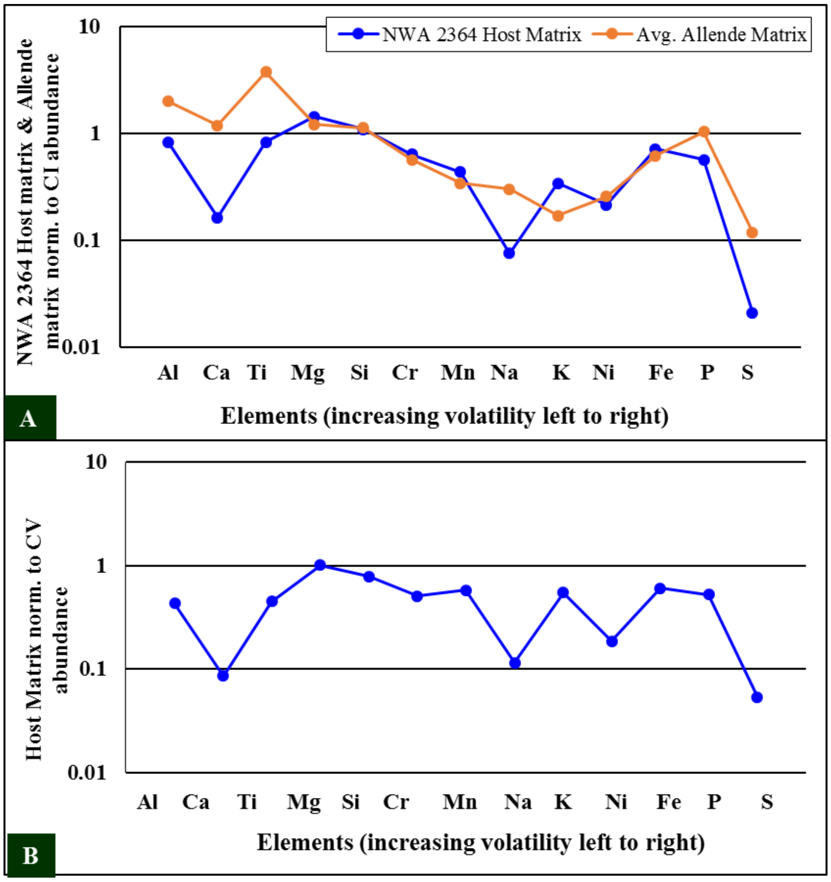

Figure 50: (A) CI abundance plot of the bulk matrix composition of NWA 2364 host and an averaged bulk matrix composition of Allende plotted together and normalized to CI chondritic values from Lodders et al. (2009). The Allende bulk matrix data comes from an average of data from Zolensky et al. (1993) and Buchanan et al. (1997). (B) CI abundance plot of the bulk matrix composition of the NWA 2364 host matrix normalized to bulk CV chondrite composition. The CV values come from Lodders and Fegley, (1998).

4.3.2. Halo Regions

Within the matrix and generally following the outline of some chondrules and other features within NWA 2364 host are distinct, continuous, curvilinear features several microns in width that appear bright in BSE images. These features strongly resemble zones of Fe enrichment described by Hanowski and Brearley (2000) surrounding altered metal grains in several CM chondrites. Following their terminology, we also term these features in NWA 2364 reaction fronts. These features have not been observed in Allende or any other CV3 chondrites before. In general these features are lower in porosity where the BSE contrast is higher, suggesting that the average atomic number is higher. Figure 37 shows a zoning profile across one of these regions with a step size of 2 µm. Within the region that is indicated to be the high-Z contrast zone there is a slight increase of Fe/Si, Ni/Si, and S/Si, but a large peak corresponding to a single elemental ratio is not apparent. The step size of the EPMA profile may not have been small enough to fully characterize the complexities of these features.

There are obvious differences between the NWA 2364 host and Allende that show that the NWA 2364 host has experienced a complex alteration indicated by the evidence above. In several ways, the alteration textures observed in the NWA 2364 host are very similar to those observed in the LI, but not the extent of the LI. For example, the alteration of chondrules is very similar with the common occurrence secondary ferroan olivines replacing primary phases. The most significant similarity between the two is the depletion in fluid mobile elements, Na, K, and S, which can be seen in Figure 51. The lack of sulfides in the host and the LI suggests that the mechanism of alteration was very similar, just more extreme in the LI.

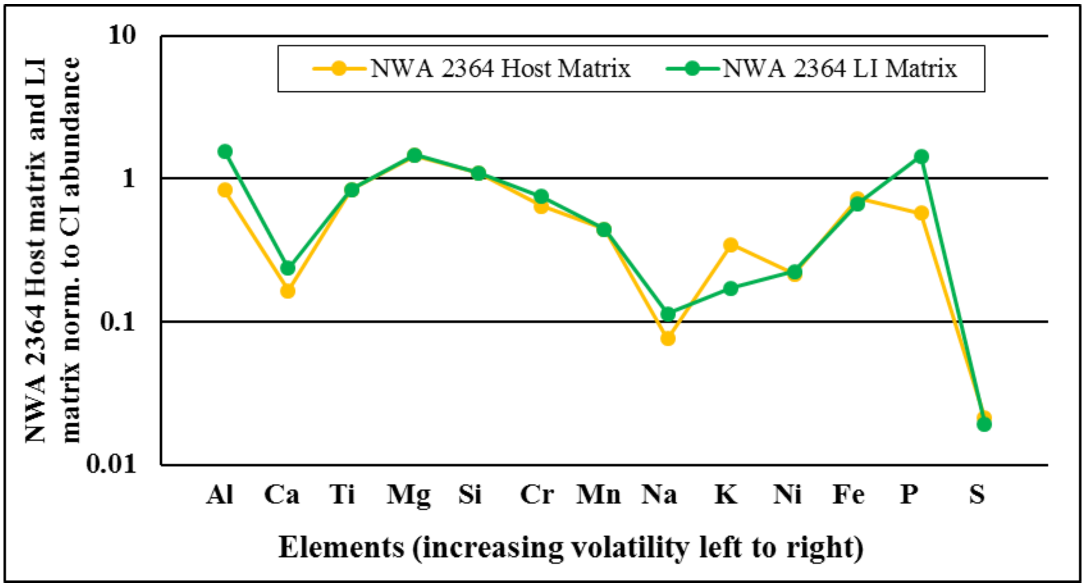

Figure 51: Compositions of bulk matrix of the NWA 2364 host and LI determined by EPMA, normalized to bulk CI chondrite values. The CI chondritic values are from Lodders et al (2009).

4.4. Alteration History of NWA 2364 and its Lithic Inclusion

The processes that altered dark inclusions are complex and have been discussed extensively in the literature e.g. (Johnson et al., 1990; Kojima and Tomeoka, 1996; Krot et al., 1997, 1998, 2000, 2001). In early studies, the idea was presented that many of the secondary features observed in the dark inclusions are the result of alteration within the solar nebula. This model is commonly referred to as the 'nebular hypothesis', e.g. (Kurat et al., 1989; Johnson et al., 1990). Over the years, the view shifted to support the concept alteration occurred post accretion on the CV3 asteroidal parent body. This major change in perspective came about as more evidence indicative of aqueous alteration at a lower temperature was found in these CV3 chondrites. Many of these later studies have argued that fluids have played an important role in the mineralogical and textural evolution of the dark inclusions as well (Krot et al., 1995, 1997, 1998, 1999, 2000, 2004; Kojima and Tomeoka, 1993, 1994, 1996; Brearley and Krot, 2013). But there are complexities in the geochemical and petrographic evidence, leading to the proposal of two different scenarios for the role of fluids; a two-step, hydration-dehydration model or a single step fluid-assisted metamorphism model. These two models are discussed in more detail below.

In order to evaluate the alteration of the LI and the host, we first briefly discuss what the likely protoliths for both rocks were, because this plays an integral role in the degree and effects of alteration. The NWA 2364 host is, as discussed above, an Allende-like oxidized CV3 chondrite consisting primarily of Mg-rich olivine-bearing chondrules. The chondrules range in size, but on average are a few hundred of microns in size up to a millimeter. Some of the chondrules contain low-Ca pyroxene, particularly in the more extensively altered chondrules. The matrix is fine-grained, but coarser grained than the matrix of the LI. The LI resembles a type A/B dark inclusion as indicated previously, but is not identical to those found in Allende. The type IA and type IIAs chondrules, even though they are heavily altered are clearly significantly smaller than those in the host. We infer that low-Ca pyroxene-rich chondrules were present before alteration. However, based on the fact that low Ca-pyroxene alters much more readily than olivine (Hanowski and Brearley, 2001), these chondrules are now represented by pseudomorphs by ferroan olivines. Heavily altered chondrules that still contain relict olivine phenocrysts were probably type IAB, low-Ca pyroxene–bearing chondrules. The protolith of the LI was clearly a carbonaceous chondrite of a type which is not represented by any specific meteorite type in our collections.

Here we discuss several lines of evidence which strongly support the idea that the NWA 2364 LI has been modified by aqueous fluids coupled with thermal metamorphism. Based on our observations of the mineralogical and textural characteristics of NWA 2364 and the LI, we propose the following scenario for the alteration history of NWA 2364 and its LI. We suggest that the components of the LI formed in the solar nebula and were accreted into the CV chondrite parent body to represent a distinct lithology. The LI was then extensively altered on the CV3 chondrite parent body via low temperature aqueous alteration that converted much of the rock into phyllosilicates. Following this episode of aqueous alteration, there was a progressive increase in temperature that ultimately dehydrated the hydrous phases and formed new anhydrous minerals. Following this alteration sequence, the LI was then emplaced into the NWA 2364 host, likely via impact regolith processes. Once emplaced into the host, the LI and host experienced minor amounts of aqueous alteration that resulted in incomplete chemical equilibration between the two lithologies. Below we present the evidence to support this interpretation.

4.4.1. LI alteration prior to emplacement: Evidence for Heating and Metamorphic Equilibration

There is definitive evidence in the lithic inclusion that it experienced an episode of thermal metamorphism at moderate temperatures. The record of thermal metamorphism is well preserved, because it was the last major event that affected the LI prior to its emplacement into the host chondrite. This thermal metamorphic event drove equilibration of mineral compositions in exactly the same manner as observed in several different chondrite groups including the ordinary chondrites and the CO3 chondrites (Brearley and Krot, 2013). The specific lines of evidence for thermal metamorphism are as follows:

- Iron enrichment along fractures in forsteritic chondrule olivine phenocrysts and Mg-rich isolated olivine grains driven by equilibration with the Fe-rich matrix.
- Compositional Mg-Fe zoning in forsteritic olivine type IA chondrule phenocrysts.
- Compositional zoning in forsteritic phenocrysts in chondrules and isolated olivine grains at the interface with ferroan overgrowths.
- Presence of hercynitic spinel in CAIs.
- Absence of hydrated minerals, but remaining textural features

Metamorphism drives the chemical equilibration of mineral phases that started off with a diverse range of compositions within the protolith material. For example, the iron enrichment we observe along the fractures and edges of Mg-rich or Fe-poor chondrule olivine phenocrysts and Mg-rich isolated olivine grains without ferroan overgrowths is a result of volume diffusion from the Fe-rich matrix olivine grains and the Fe-poor chondrule olivine phenocrysts.

The Mg-rich chondrule olivine phenocrysts and Mg-rich isolated olivine grains that have ferroan overgrowths also exhibit a Fe enrichment at the interface between the overgrowth and the original forsteritic phenocryst. This is indicative of volume diffusion, similar to the process that as has occurred for the Fe-enrichment along fractures and edges of phenocrysts that did not exhibit ferroan overgrowths. This metamorphic equilibrium would most likely have occurred after the ferroan overgrowths were in place.

The range of composition of the matrix olivines is another indicator of metamorphic equilibration. The more metamorphosed and equilibrated the meteorite is, the narrower the range in composition that will be observed in the matrix olivine compositions (Brearley and Jones, 1998 & Bonal et al., 2006). While we do not have exact compositions for the matrix olivines, as they were too small to acquire accurate compositions, the Fe content in the matrix as seen in the histogram (Figure 28) shows a peak clustered at 25-30 Fe wt%. A narrow range in composition has been noted several times in the metamorphosed oxidized CV3 chondrite, Allende, and its dark inclusions (e.g. Peck, 1984; Krot et al., 1995; Brearley and Krot, 2013).

Similarly, the compositions of the spinel present in the altered CAI also indicate metamorphic equilibration as well. Through volume diffusion, exchange with the Fe-rich matrix has caused the spinels in the CAIs to change from their initial pure $MgAl_2O_4$ composition to become hercynitic. In the CAI, the spinel composition extends to 34 mol % hercynite.

The final piece of evidence for heating is the absence of hydrous phases within the LI, but the relict textural features that indicate there were hydrous phases present prior to thermal metamorphism. Figure 17a is a representative example of the vein textures that have crystallographically-oriented, platy, ferroan olivines filling the vein. This vein texture is similar to those seen in serpentinized terrestrial olivines and other carbonaceous chondrites, notably the CM chondrites (e.g. Hanowski and Brearley, 2001 & Velbel et al., 2012). No other mechanism for the formation of this texture has been observed and it appears to be a unique characteristics of serpentinization of olivine. The difference in this case is that the crystallographically-oriented phases are olivines not serpentine grains, which suggests the serpentines were dehydrated and perhaps relatively quickly as the texture of the serpentine was maintained within the vein. A heating event similar to this, but not as complete, was proposed for partially heated phyllosilicates in the Yamato-86720, CM carbonaceous chondrite by Tomeoka et al. (1989). Aside from the ferroan olivine grains observed within veins, similar oriented, ferroan olivines have been observed within chondrule interiors. Figure 20 is a high magnification BSE image of a representative example of the oriented olivine grains within the interior of the chondrule where original chondrule mesostasis would have been. This texture could indicate a similar dehydration of phyllosilicate phases.

4.4.2. LI alteration prior to emplacement: Evidence for Aqueous Alteration

Many of the secondary phases and textures observed within the LI indicate that aqueous solutions coupled with metamorphic processes contributed significantly to the complex textural characteristics of the LI. Here we discuss each of these lines of evidence and discuss their implications for the role of aqueous fluids. The specific chemical, mineralogic, and textural evidence that supports the role of aqueous fluids is as follows:

- Redistribution of the alkali elements, Na and K, the alkali earth element, Ca, and the chalcophile element, S, within and out of the LI.
- The presence of cross-cutting veins and serrated textures along edges of phenocrysts.
- Replacement of primary phases in chondrules by ferroan olivine; ferroan overgrowths, replacement of opaque nodules, replacement of low Ca-pyroxene, and replacement of mesostasis material.
- Heavy oxygen isotope enrichment.

Mobilization and redistribution of fluid mobile elements

The LI shows significant evidence of the redistribution of the alkalis Na and K, the alkali earth, Ca, and the chalcophile element, S. All four of these elements are soluble in aqueous fluids, but their apparent behavior in the LI is significantly different, as discussed below. In unaltered chondritic materials, Na and K are dominantly contained within the mesostasis of chondrules either within a glass or sometimes within rare, primary igneous feldspar. Calcium is also commonly present in chondrule glass, feldspar, or Ca-rich pyroxene, but is also present in high concentrations in several CAI phases as well. Sulfur is only present in sulfides, either within chondrules or within the matrix material. All four of these elements are also present in matrix materials, but at significantly lower concentrations.

The cosmochemical behavior of Ca, Na, K, and S

Cosmochemically, Ca is classified as a lithophile, refractory element, and is one of the first elements to condense from a gas of solar composition at temperatures between

1,850-1,400K (Wasson, 1985; Palme and Jones, 2005). The elements, Na, K, and S are classified as moderately volatile elements and condensed over the temperature range 1,230-640K. Sulfur in particular is the most volatile of these elements and condenses at the lowest temperature. These elements are typically depleted in abundance in all chondrite groups, including the CV3 chondrites, relative to CI abundances, (Palme and Jones, 2005). Calcium, Na, K, and S are all important indicators of aqueous alteration, despite their different cosmochemical behavior, because each of these elements is soluble in aqueous fluids, such that changes in their abundances, relative to other less soluble elements is indicative of mobilization and transport of these elements via a fluid. Therefore, examining the alteration behavior of the phases that are the common carriers of these elements will provide insights into the mechanism of alteration, as well as how these elements may have been redistributed by aqueous fluids. Here we discuss the behavior of these four elements within different phases found within the LI and their implications for the role of aqueous alteration as an important processes in the geologic evolution of the LI.

The behavior of Ca

Our observations suggest that the Ca has not been lost to any significant degree from the LI, but instead has been extensively redistributed from the chondrules into the matrix. The Ca associated with primary, Ca-bearing mesostasis glass has been stripped from the chondrules and redistributed into the matrix in most instances. The Ca now occurs within the matrix in Ca-rich pyroxene aggregates that occur just outside the edge of the fine-grained chondrule rims of chondrules, as shown in Figures 19 & 26. The remaining Ca within the matrix is present as a high abundance of Ca-rich pyroxene aggregates distributed randomly through the matrix. On the other hand, the Ca-rich pyroxene aggregates that form the rim around the periphery of the LI formed in a second alteration event, after emplacement of the LI into the host, as discussed in the following section. The lack of Ca in the chondrules, but present in secondary pyroxene phases surrounding chondrules and within the matrix is very apparent and noted in other Allende dark inclusions (e.g. Krot et al., 1998; Krot et al., 2000; Brearley and Krot, 2013).

The behavior of Na and K

There is a large difference between the behavior of Na and K versus Ca. As discussed above, Ca appears to have been redistributed throughout the LI, whereas the K and Na are absent from the LI. This is evident within both the chondrules and the matrix. Figure 19 shows a-ray elemental map of a representative altered chondrule in the LI that is entirely devoid of Na-bearing phases, such as the original chondrule glass or secondary phases such as nepheline or sodalite. In addition, there is no evidence of any Na-bearing phases in the matrix. Figure 48 shows that the Na that would have been leached from chondrule glass by aqueous fluids was not incorporated in Na- and K-bearing phases in the matrix. This behavior contrasts with the behavior of Ca described above. This depletion, especially in Na is distinct from the behavior observed in Allende dark inclusions, where either the chondrule pseudomorphs contain secondary Na-bearing phases, or the matrix is enriched in the Na-bearing phases (Krot et al., 2000). In the NWA 2364 LI, the absence of Na and K-bearing phases in the matrix and the chondrules, implies that there has been significant removal of these elements from the LI, a process that can only be attributed to fluid-rock interaction.

The behavior of S

As shown in Figure 47, a composite S-Fe-Mg X-ray map, sulfides are entirely absent from the chondrules and matrix in the LI. The low mineralogical abundance of S is confirmed by the normalized elemental abundance diagram (Figure 49), discussed earlier, which shows S is very depleted in the LI matrix. This is contrary to all other observations of dark inclusions which show that sulfides are widely present in the matrix, but not in chondrules e.g. the Allende dark inclusion 4301-2 and IVa (Krot et al., 2000). We conclude that to completely remove S from both chondrules and matrix in the NWA 2364 LI, requires that sulfides underwent dissolution in a fluid and S in solution was lost from the LI, along with Na and K.

Elemental depletions indicative of aqueous alteration

The depletions the elements described can only reasonably be attributed to the interaction of a fluid with the LI. The elements Na, K, and S are all volatile elements that are depleted in bulk CV chondrites. However, the LI is significantly more depleted than normal CV elemental abundances (see Figure 49b) for these elements. There is no reasonable mechanism that can be invoked to explain this depletion, coupled with the mineralogical data, other than interaction with an aqueous fluid. The evidence for the involvement of a fluid is very clear; the highly fluid mobile elements have been completely modified from their original locations within the clast. Calcium has been redistributed from the chondrules into the matrix of the LI forming the Ca-rich pyroxene aggregates described above. The Na, K, and S have effectively been leached from the entirety of the LI, ultimately changing the chemical composition of the rock by the removal of these elements, i.e. the LI has been altered by a metasomatizing fluid. When compared to the Allende dark inclusions studied by Krot et al. (2000) it is apparent that all of them were altered by a fluid. However, the NWA 2364 LI was clearly altered more extensively, both mineralogically and geochemically, and has had its bulk composition significantly modified. It is plausible that this difference could be explained by a lower fluid-rock ratio in the Allende inclusions, such that a complete leaching of these fluid mobile elements did not occur.

Enrichment in heavy oxygen isotopic composition

The oxygen isotopic composition of the LI also provides evidence of fluid-rock interactions that is consistent with the petrographic observations. The oxygen isotopic composition of the LI is displaced from the CCAM line and shifted to a heavier isotopic composition. This is indicative of mass dependent fluid-rock interactions on the LI parent body, comparable to the alteration that has been invoked to explain the oxygen isotopic composition of dark inclusions in the reduced CV3 chondrites (Krot et al., 1999). The bulk oxygen isotopic composition is not recording just the mass dependent evolution resulting from aqueous alteration, because the bulk compositions of altered dark inclusions do not lie along a line with slope 0.5. Instead they lie on a mixing line that is the result of mixing of the oxygen isotopic compositions of remaining primary nebular phases, with secondary phases that have been formed by fluid-rock interaction and probably lie on a mass dependent fraction line. These displacements in bulk compositions to the right of the CCAM line for the reduced CV dark inclusions, as well as bulk CV_{OxB} chondrites, such as Bali that petrographically show evidence for aqueous alteration, suggest that the water-rock ratio was higher and the meteorites had more fluid to interact with, ultimately changing their bulk isotopic compositions (Clayton and Mayeda, 1999).

An additional process that can also result in an enrichment in heavy oxygen isotopes is dehydration of hydrous phases. As discussed earlier, there is evidence that the LI experienced dehydration of serpentine, that formed as result of aqueous alteration of primary olivine. Dehydration would also shift the isotopic composition to that of a heavier one, because ^{16}O is preferentially incorporated into the water that is lost. However, based on data for metamorphosed carbonaceous chondrites that have clearly experienced dehydration (Brearley and Krot, 2013), the enrichment in ^{17}O in the LI inclusion is not as large as would be expected for a rock that has undergone a dehydration event. This observation does not necessarily rule out a role for dehydration in the evolution of LI, because it is possible that the LI underwent later equilibration with a fluid in the host NWA 2364 chondrite.

The presence of cross cutting veins and serrated textures along the edges of olivine phenocrysts

The presence of cross cutting veins through olivine phenocrysts has been well documented in aqueously altered carbonaceous chondrites and in terrestrial samples e.g. (Wicks and Whittaker, 1977; Hanowski and Brearley, 2001; Velbel et al., 2012; Plümper et al., 2012; Lee and Lindgren, 2016). Several examples and different textural types of these veins cross-cutting chondrule olivine phenocrysts have been described in the results section for the LI (Figs. 15 and 17). It is clear that these veins represent alteration via fluid-rock interactions. As a result of the continued dissolution of the olivine the edges of the phenocryst take on a serrated texture (see Figure 17c from results section). This a well observed texture in terrestrial and extraterrestrial olivine phenocrysts undergoing dissolution (e.g. Hanowski and Brearley, 2001; Velbel et al., 2009; Lee and Lindgren, 2016).

Replacement of original phases by ferroan olivine

There are several different examples of ferroan olivine replacing primary phases that include: ferroan overgrowths on both type IA and type IIA chondrule olivine phenocrysts and isolated olivine grains, replacement of low-Ca pyroxenes in chondrules, replacement of opaque nodules, and replacement of chondrule mesostasis material, with complete chondrule pseudomorph in extreme cases (see Figures 13, 14, 15, & 16). Here we present the arguments that these different examples of ferroan olivine formed in the presence of a fluid. There are several complimentary lines of evidence that suggest the involvement of fluids as the best explanation. 1) There is significant evidence of elemental mobility for fluid-mobile elements indicating that a fluid was present as discussed above. 2) The growth of new ferroan olivine as rims and the replacement of low-Ca pyroxene by ferroan olivine are not just processes that involve metamorphic equilibration of cations. These processes involve significant elemental mass transport was involved, notably for major elements such as Mg, Fe, and Si. This evidence strongly implies the presence of a fluid acting as a catalyst and mass transfer agent. Simple metamorphic equilibration of Mg and Fe between olivine and pyroxene does not result in the replacement of pyroxene or the extensive growth of new ferroan olivine. 3) The textures of ferroan olivine in the LI are very similar to those that have been observed in Allende and Allende dark inclusions, particularly the ferroan overgrowths which have been explained as growth in the presence of a fluid (Krot et al., 2004). 4) The oxygen isotopic composition clearly indicates the LI was altered in the presence of a fluid as described in detail earlier. Combining all of these complimentary pieces of evidence for the presence of a fluid we argue that the formation of these secondary ferroan olivines was the result of interactions via aqueous fluids.

4.4.3. Mechanism for LI alteration- role of the fluid

In the following section we discuss the source of the fluids that were involved in the alteration of the LI inclusion and the sequence of events that produced the textural and mineralogical characteristics of the LI. We have evidence in the previous sections that suggests the LI was first hydrated, forming secondary hydrous minerals such as serpentine, and was subsequently heated causing dehydration. Those hydrous minerals became dehydrated and ultimately created secondary minerals like the ferroan overgrowths, through the process of fluid-assisted metamorphism as the rock heated before the fluid was ultimately lost. In the following sections we will provide a possible explanation for the source of the fluid and the role that it played in the alteration sequence of the LI.

4.4.3.i. Fluids that altered the LI prior to dehydration

Earlier, we presented evidence that the LI was altered by aqueous fluids at low temperatures, in order to form hydrous phases. The most likely source of the fluid was an internal source, produced from the melting of ices that accreted into the parent CV3 parent body asteroid when it formed. As these ices began to melt from heat produced from the decay of ^{26}Al, they interacted with the surrounding rock. This began the aqueous alteration process that led to the replacement of primary phases by hydrous minerals to form a partially hydrated meteorite that probably had mineralogical and textural similarities to CM chondrites. In common with altered CM chondrites, this stage of alteration did not go to completion, preserving some relict chondrule phenocrysts. The cryptic evidence for this stage of hydration is evident from the textures of olivine-rich veins that mimic the serpentine veins observed in CM chondrites. We propose that the crystallographically-oriented, platy, ferroan olivines in the veins are the dehydration products of serpentine. These veins show that the LI contained hydrous phases before temperature increased significantly to drive dehydration and metamorphism.

4.4.3.ii. Dehydration as a result of thermal metamorphism

The model of (Grimm and McSween, 1989) shows that the heat produced from the decay of accreted ^{26}Al is sufficient to increase temperatures on carbonaceous chondrite parent bodies to metamorphic temperatures. This increase in temperature causes H_2O to be released from the hydrous phases that had formed during the initial low temperature hydration phase. In addition, the hydration reaction of olivine to form serpentine is exothermic. As a consequence, once this reaction starts, it leads to a further increase in metamorphic temperatures. This metamorphic event probably reached temperatures, around 500˚C, high enough to form the anhydrous phases observed (Brearley and Krot, 2013).

With the progressive metamorphism the alteration style would have shifted to a scenario similar to that proposed for Allende dark inclusions, i.e., fluid-assisted metamorphism, also implying lower fluid-rock ratios, as well compared to that during the initial hydration event. As the fluid left the system, the soluble elements such as Na, K and S that the hydration event had mobilized, left with the fluid. This is a likely explanation for what stripped those elements from the LI. As cooling began to take place, it is likely that the fluid had been completely lost from the LI, as there are no hydrous minerals present that indicate back reactions while cooling endured.

4.4.4 Post-emplacement alteration of the Host and LI on the CV3 parent body

Following impact regolith processes that emplaced the LI into the host of the NWA 2364 chondrite, there are two lines of evidence that suggest the host and the LI have interacted. These are i) the Ca-rich rim surrounding the LI and ii) the zone of Ca depletion associated with the rim. This Ca-rich rim feature consists largely of Ca-rich pyroxene aggregates that define the interface between the host and the LI (see Figures 3 & 26a). Figure 26a shows the zones of depletions within the LI. The Ca-rich phases are concentrated along the boundary of the host and LI. Evidence of such an interaction was first reported in Allende dark inclusions described in Krot et al. (2000) (Figure 26b). Similar Ca-rich pyroxene rims were also described around Efremovka dark inclusions by Krot et al. (1999), but not to the extent as in Allende or in NWA 2364. The lack of andradite, wollastonite, and kirschsteinite as reported in the Krot et al. (2000) study in the rim feature in NWA 2364 suggest the alteration occurred in more reducing conditions; thus phases such as andradite never crystallized. The most likely mechanism for the formation of this layer is that it is the result of the growth as aqueous solutions attempted to equilibrate between the matrix of the host and that of the LI. Based on the zone of depletion, in the LI, it seems likely that the Ca was mobilized by the fluid, as a result of dissolution of Ca-rich pyroxene and precipitated along the boundary between the LI and the host. This exchange between the LI and host during equilibration could have occurred at lower temperatures with a lower fluid-rock ratio than the conditions that affected the LI as Krot et al. (2000) had suggested as a likely explanation for the growth of the rims along the dark inclusions and Allende host.

The TEM observations of one of the Ca-rich pyroxene aggregates within the matrix of the LI shows evidence of alteration of the pyroxene grains (see Figures 24 & 25). This aggregate was located on the right side of the clast, near a zone of Ca depletion, closer to the rim than the central region of the LI (see Figure 26a). A saw tooth texture is present along the edges of several different pyroxene grains, adjacent to pore spaces, indicative of dissolution of pyroxene (Velbel, 2007).

The final piece of evidence for the interaction of the LI and host, post emplacement comes from the oxygen isotopic composition of the host and LI. The LI and the rim oxygen isotopic compositions show an enrichment in the heavy oxygen isotopes and the host samples do as well (Figures 45 & 46). An aqueous fluid was involved in the alteration process as the rim and the host are displaced from the CCAM line. As mentioned in the above section, we proposed a dehydration event for the LI before it was emplaced into the host, yet the isotopic composition does not directly reflect a further enrichment in heavier oxygen in the LI. This lack of further enrichment in the oxygen isotopic composition could imply the equilibration of isotopic composition of the LI with fluids from NWA 2364 host following this emplacement.

4.4.5 Fluid that altered host and LI post emplacement

After the LI was emplaced into the host, it is clear that there was interaction between the two lithologies based mainly on the Ca-rich pyroxene rim that formed around the LI, as well as the associated depletion zone of Ca around the edge of the LI. There are three potential scenarios for the source of the fluid that resulted in the interaction between them. The first is that the host and LI were both dry and an external fluid entered the system and interacted with both rocks; the second is that the LI contained a fluid and the host was dry when emplacement occurred; the final scenario is the reverse situation, a fluid-bearing host and a dry LI.

The third scenario is probably the most likely, because 1) the LI appears to have lost all of its fluid, during the dehydration event thus making it dry and causing the depletion in Na, K, and S. 2) the interaction between the host and LI seems to be on a small scale, i.e. just around the edge of LI. Neither the host nor the LI exhibit wholesale signs of interaction and alteration that might be expected if an influx of fluid came from an external source. 3) Dissolution of Ca-rich pyroxene has only occurred in the LI; there is no evidence of dissolution or modification of phases in the adjacent host, suggesting that fluid infiltrated into the LI from the host, rather than the reverse. This scenario is broadly analogous to alteration of igneous glass, where a fluid front moves into the glass and causes dissolution and mobilization of elements (e.g. Burger and Brearley, 2004; 2005).

In this scenario, the host may still have been undergoing alteration at the time of emplacement of the LI. We suggest that the host was most likely being altered in a similar manner to Allende, but at a slightly higher fluid-rock ratio. This is based on the similarities and differences between NWA 2364 and Allende, with the most prominent evidence for more fluid involvement coming from the lack of fluid mobile elements, such as S and the displacement in the oxygen isotopes from the CCAM line. While the fluid-rock ratio was probably not as high for the host as in the LI during its earliest stages of hydration, it is likely there was a fluid involved and still present upon emplacement of the LI.

The dissolution of Ca-rich pyroxene in an outer zone of the LI suggests that the LI and the host were out of geochemical equilibrium with one another. We propose that the fluid that was in the host infiltrated into the LI and caused dissolution of the Ca-rich pyroxenes in the aggregates. Calcium in solution moved down a geochemical potential gradient, out of the LI, until geochemical conditions were encountered that caused new Ca-rich pyroxenes to precipitate out of the solution, i.e. along the interface between the LI and the host. This is similar to the model given by Krot et al. (2000) for the Ca-rich pyroxene rims around Allende dark inclusions. The main difference from NWA 2364 is that these rims do not have the same complex zoned mineralogy, as described by Krot et al. (2000), implying the geochemical conditions and composition of the fluid in Allende was different from those in NWA 2364. The growth of new Ca-rich pyroxene is most prominently seen around the left and bottom regions of the LI and host interface (Figure 26a). From this observation we suggest the growth of the new pyroxenes grew from the fluid in the NWA 2364 host. Calcium-rich pyroxene growth was not homogenous around the rim of the LI, as indicated by the lack of the tightly clustered Ca-rich pyroxene aggregates along portions of the right side of the LI (as indicated in Figure 26a). In these regions, it appears that the precipitation of high-Ca pyroxene occurred further into the host, possibly due to the heterogeneous distribution of fluid or localized variations in geochemical conditions.

In addition to the dissolution and reprecipitation of Ca-rich pyroxenes, it is likely that this fluid interaction caused the isotopic composition of the LI to become more equilibrated to that of the host. As a result, the significant heavy isotopic composition of the LI that would be expected as a result of hydration and dehydration has been modified. Ultimately, this fluid must have been lost from the LI and the host rock, but our data do not constrain when this happened. There is no evidence of phyllosilicates in the LI, which could have formed by retrograde reactions, but they may be present in the host rock. This evidence suggests that most of the remaining fluid must have been lost prior to cooling of the asteroid.

5. Conclusion

The alteration history of NWA 2364 and its LI is complex. Before being emplaced and altered in situ with the host meteorite, the LI experienced extensive alteration in another location on the CV3 chondrite parent body.

- The LI low temperature aqueous alteration on the CV3 chondrite parent body. This alteration converted much of the rock into phyllosilicates indicated by the presence of the alteration veins in the chondrule olivine phenocrysts, which are very characteristic of replacement of olivine by serpentines. This alteration process mobilized Ca, K, Na, and S from original phases and redistributed them into the matrix. The Ca formed new Ca-rich pyroxene aggregates in the matrix, surrounding chondrules and chondrule pseudomorphs. The style and extent of alteration for LI was different and more extreme than observed in other dark inclusions, especially those in Allende.

- Following this aqueous alteration, there was a progressive increase in temperature that resulted in the dehydration of hydrous phases, ultimately shifting the alteration style to that of more like fluid-assisted metamorphism. The vein textures found within the LI chondrule are the first definitive evidence for hydration followed by dehydration for a dark inclusion. The dehydration of hydrous phases resulted in the formation of platy ferroan olivines in vein fractures. The fluid released from dehydration also promoted the growth of ferroan olivine overgrowths. Ultimately, this fluid was lost from the rock and resulted in the loss of the soluble, fluid-mobile elements, Na, K, and S. No back reaction occurred during cooling of the rock following peak metamorphic conditions. Additional work is required to fully characterize the physio-geochemical conditions of this complex alteration the LI endured.

- The LI was later emplaced into the host chondrite, likely via impact regolith processes, where interaction between the host and LI occurred, ultimately lithifying the two together.

- At the time of emplacement the host contained an aqueous fluid, while the LI was probably dry, thus creating the scenario where the two were out of geochemical equilibrium with one another. Due to this disequilibrium, the fluid in the host migrated into the LI, subsequently dissolving some of the Ca-rich pyroxene aggregates. Dissolved Ca moved through the fluid and precipitated along the interface between the LI and host, where the geochemical conditions were appropriate for the reprecipitation of new Ca-rich pyroxene.

- The host rock shows strong evidence (isotopic and elemental) evidence for fluid-rock interactions, which is not apparent in Allende. The fluid mobile elements, like S, are more depleted in the NWA 2364 bulk matrix than in the Allende bulk matrix. The abundance of Na-bearing phases and sulfides are significantly lower in NWA 2364 than in Allende. It is possible that the NWA 2364 host and the LI could have been a potential source of fluids that caused metasomatic enrichment of volatile elements, like Na and Cl in Allende or other CV_{OxA} chondrites. More work needs to be done to fully characterize the alteration history of the host and determine how its alteration fits into complex relationships between other CV3 chondrites and their interactions with aqueous fluids.

In the future, more work will be done on the host of NWA 2364 in order to fully characterize its alteration history. We are also waiting for LA-ICPMS results from chondritic components in the LI, which will tell us in more depth the fluid-rock interactions the LI experienced. Finally, I-Xe dating is also being carried out to understand the relative timing of alteration of the NWA 2364 host and lithic inclusion to put their alteration history into context with that of other CV3 chondrites.

References:

Allen, J.M, Davis, A.M., and Hutcheon, I.D., 1978, Mineralogy, textures, and mode of formation of a hibonite-bearing Allende inclusion: Lunar and Planetary Science Conference Proceedings, p. 1209–1233.

Anders, E., 1964, Origin, age, and composition of meteorites, *in* Space Science Reviews, p. 583–714.

Anders, E., and Goles, G.G., 1961, Theories on the origin of meteorites: J. Chem. Education, p. 58–66, doi:10.1021/ed038p58.

Bischoff, A., Palme, H., Spettel, B., Clayton, R.N., and Mayeda, T.K., 1988, The chemical composition of dark inclusions from the Allende meteorite, *in* Lunar and Planetary Science Conference, p. 88–89.

Bonal, L., Quirico, E., Bourot-Denise, M., and Montagnac, G., 2006, Determination of the petrologic type of CV3 chondrites by Raman spectroscopy of included organic matter: Geochimica et Cosmochimica Acta, v. 70, p. 1849–1863, doi:10.1016/j.gca.2005.12.004.

Boudier, F., Baronnet, A., and Mainprice, D., 2009, Serpentine mineral replacements of natural olivine and their seismic implications: Oceanic lizardite versus subduction-related antigorite: Journal of Petrology, v. 51, p. 495–512, doi:10.1093/petrology/egp049.

Brearley, A.J., 2014, Nebular Versus Parent Body Processing: Elsevier Ltd., v. 1, 309-334 p., doi:10.1016/B978-0-08-095975-7.00106-6.

Brearley, A.J., and Jones, R.H., 1998, Chapter 3. Chondritic Meteorites: Reviews in Mineralogy, vol. 36, Planetary Materials, p. 3-01-3–370.

Brearley, A.J., 1997, Disordered biopyriboles, amphibole, and talc in the Allende meteorite: Products of nebular or parent body aqueous alteration? Science, v. 276, p. 1103–1105, doi:10.1126/science.276.5315.1103.

Brearley, A.J., and Krot, A.N., 2013, Metasomatism in the early solar system: The record from chondritic meteorites, *in* Metasomatism and the Chemical Transformation of Rock, p. 659–789.

Buchanan, P.C., 1991, Petrography and mineral chemistry of dark inclusions from the meteorite Allende [Masters Thesis]: University of Houston, 67 p.

Buchanan, P.C., Zolensky, M.E., and Reid, A.M., 1997, Petrology of Allende dark inclusions: Geochimica et Cosmochimica Acta, v. 61, p. 1733–1743, doi:10.1016/S0016-7037(97)00019-7.

Bunch, T.E., and Chang, S., 1983, Allende dark inclusions; samples of primitive regoliths, *in* Abstracts of papers presented to the Fourteenth lunar and planetary science conference., v. 14, p. 75–76.

Burger, P.V., and Brearley, A.J., 2004, Chondrule Glass alteration in type IIA chondrules in the CR2 Chondrites EET87770 and EET92105: Insights into elemental exchange between chondrules and matrices, *in* Abstracts of papers presented to the Thirty-fifth Lunar and Planetary Science Conference., p. 285–287.

Burger, P.V., and Brearley, A.J., 2005, Localized chemical redistribution during aqueous alteration in CR2 carbonaceous chondrites EER87770 and EET92105, *in* Lunar and Planetary Science Conference, p. 2288.

Clayton, R.N., 1977, Distribution of the pre-solar component in Allende and other carbonaceous chondrites: Earth and Planetary Science Letters, v. 34, p. 209–224.

Clayton, R.N., and Mayeda, T.K., 1999, Oxygen isotope studies of carbonaceous chondrites: Geochimica et Cosmochimica Acta, v. 63, p. 2089–2104, doi:10.1016/S0016-7037(99)00090-3.

Elkins-Tanton, L.T., Weiss, B.P., and Zuber, M.T., 2011, Chondrites as samples of differentiated planetesimals: Earth and Planetary Science Letters, v. 305, p. 1–10, doi:10.1016/j.epsl.2011.03.010.

Grimm, R.E., and McSween, H.Y., 1989, Water and the thermal evolution of carbonaceous chondrite parent bodies: Icarus, v. 82, p. 244–280.

Grossman, L., 1980, Refractory Inclusions in the Allende Meteorite: Annual Review of Earth and Planetary Sciences, v. 8, p. 559–608, doi:10.1146/annurev.ea.08.050180.003015.

Grossman, L., 1972, Condensation in the primitive solar nebula: Geochimica et Cosmochimica Acta, v. 36, p. 597–619.

Hanowski, N.P., and Brearley, A.J., 2000, Iron-rich aureoles in the CM carbonaceous chondrites Murray, Murchison, and Allan Hills 81002: Evidence for in situ aqueous alteration: Meteoritics and Planetary Science, v. 35, p. 1291–1308, doi:10.1111/j.1945-5100.2000.tb01517.x.

Hanowski, N.P., and Brearley, A.J., 2001, Aqueous alternation of the chondrules in the CM carbonaceous chondrite, Alla Hills 81002: Implications for parent body alternation: Geochimica et Cosmochimica Acta, v. 65, p. 495–518, doi:10.1016/S0016-7037(00)00552-4.

Housley, R.M., and Cirlin, E.H., 1983, On the alteration of Allende chondrules and the formation of matrix: Chondrules and their origins: Lunar and Planetary Institute, p. 145–161.

Johnson, C.A., Prinz, M., Weisberg, M.K., Clayton, R.N., and Mayeda, T.K., 1990, Dark inclusions in Allende, Leoville, and Vigarano: Evidence for nebular oxidation of CV3 constituents: Geochimica et Cosmochimica Acta, v. 54, p. 819–830, doi:10.1016/0016-7037(90)90376-V.

Jones, R.H., 1996, FeO-rich, porphyritic pyroxene chondrules in unequilibrated ordinary chondrites: Geochimica et Cosmochimica Acta, v. 60, p. 3115–3138, doi:10.1016/0016-7037(96)00152-4.

Keller, L.P., Thomas, K.L., Clayton, R.N., Mayeda, T.K., DeHart, J.M., and McKay, D.S., 1994, Aqueous alteration of the Bali CV3 chondrite: Evidence from mineralogy, mineral chemistry, and oxygen isotopic compositions: Geochimica et Cosmochimica Acta, v. 58, p. 5589–5598, doi:10.1016/0016-7037(94)90252-6.

Kojima, T., Tomeoka, K., and Takeda, H., 1993, Unusual dark clasts in the Vigarano CV3 carbonaceous chondrite: record of parent body process: Meteoritics, v. 28, p. 649–658, doi:10.1111/j.1945-5100.1993.tb00636.x.

Kojima, Tomoko and Tomeoka, K., 1994, Evidence for aqueous alteration and thermal metamorphism in a dark clast found in Allende: Meteoritics, v. 29, p. 484.

Kojima, T., and Tomeoka, K., 1996, Indicators of aqueous alteration and thermal metamorphism on the CV parent body: Microtextures of a dark inclusion from Allende: Geochimica et Cosmochimica Acta, v. 60, p. 2651–2666, doi:10.1016/0016-7037(96)00116-0.

Kracher, A., Keil, K., Kallemeyn, G.W., Wasson, J.T., Clayton, R.N., and Huss, G.I., 1985, The Leoville (CV3) accretionary breccia, *in* Proceedings in the sixteenth Lunar and Planetary Science Conference, v. 90, p. 123–135.

Krot, A.N., Brearley, A.J., Ulyanov, A.A., Biryukov, V. V., Swindle, T.D., Keil, K., Mittlefield, D.W., Scott, E.R.D., Clayton, R.N., and Mayeda, T.K., 1999, Mineralogy, petrography, bulk chemical, iodine-xenon, and oxygen-isotopic compositions of dark inclusions in the reduced CV3 chondrite Efremovka: Meteoritics and Planetary Science, v. 34, p. 67–89, doi:10.1111/j.1945-5100.1999.tb01733.x.

Krot, A.N., Scott, E.R.D., and Zolensky, M.E., 1995, Mineralogical and chemical modification of components in CV3 chondrites: nebular or asteroidal processing? Meteoritics, v. 30, p. 748–775, doi:10.1111/j.1945-5100.1995.tb01173.x.

Krot, Alexander N., Keil, K., Scott, E.R.D., Goodrich, C.A., and Weisberg, M.K., 2014, Meteorites and Cosmochemical Processes, *in* Treatise on Geochemistry: Second Edition, p. 41–61.

Krot, N., Scott, R.D., and Zolensky, M.E., 1997, Origin of fayalitic olivine rims and plate-like matrix olivine in the CV3 chondrite Allende and its dark inclusions: Meteoritics & Planetary Science, v. 32, p. 31–49.

Krot, Petaev, and Bland, 2004, Multiple formation mechanisms of ferrous olivine in CV carbonaceous chondrites during fluid-assisted metamorphism: Antarctic Meteorite Research, v. 53, p. 1689–1699, doi:10.1017/CBO9781107415324.004.

Krot, Petaev, Meibom, and Keil, 2000, In situ growth of Ca-rich rims around Allende dark inclusions: Geochemistry International, v. 38, p. S351–S368.

Krot, Petaev, Zolensky, Keil, Scott, and Nakamura, 1998, Secondary calcium-iron-rich minerals in the Bali-like and Allende-like oxidized CV3 chondrites and Allende dark inclusions: Meteoritics & Planetary Science, v. 33, p. 623–645, doi:10.1111/j.1945-5100.1998.tb01668.x.

Kurat, G., Palme, H., Brandstatter, F., and Huth, J., 1989, Allende xenolith AF: Undisturbed record of condensation and aggregation of matter in the solar nebula: Zeitschrift fur Naturforschung, v. 44a, p. 988–1004, doi:10.1190/segam2013-0137.1.

Lee, M.R., and Lindgren, P., 2016, Aqueous alteration of chondrules from the Murchison CM carbonaceous chondrite: Replacement, pore filling, and the genesis of polyhedral serpentine: Meteoritics and Planetary Science, v. 51, p. 1003–1021, doi:10.1111/maps.12644.

Lodders, K., Palme, H., and Gail, H.P., 2009, Abundances of the elements in the solar system: Trümper JE (ed.) Landolt-Börstein, New Series, v.VI/4B, p. 560-598.

Lodders, K., and Fegley Jr., B., 1998, Meteorites, in The Planetary Scientist's Companion, v.1: Oxford University Press, Oxford-New York, p. 314-316.

MacPherson, Glenn J., and Grossman, L., 1984, "Fluffy" Type A Ca-, Al-rich inclusions in the Allende meteorite: Geochimica et Cosmochimica Acta, v. 48, p. 29–46.

McSween Jr., H.Y., 1977, Petrographic variations among carbonaceous chondrites of the Vigarano type: Geochimica et Cosmochimica Acta, v. 41, p. 1777–1790.

Palme, H., and Jones, A., 2003, Solar system abundances of the elements, *in* Treatise on Geochemistry: First edition, p. 41–61.

Palme, H., and Wark, D.A., 1988, CV chondrites: high temperature gas-solid equilibrium vs. parent body metamorphism, *in* Lunar and Planetary Science Conference, v. 19, p. 897.

Palme, H., Kurat, G., Spettel, B., and Burghele, A., 1989, Chemical composition of an unusual xenolith of the Allende meteorite: Zeitschrift fur Naturforschung, v. 44, p. 1005–1014.

Pecke, J.A., 1988, Primitive material surviving in chondrites: matrix, *in* Meteorites and the Early Solar System, p. 718–745.

Plümper, O., Røyne, A., Magrasó, A., and Jamtveit, B., 2012, The interface-scale mechanism of reaction-induced fracturing during serpentinization: Geology, v. 40, p. 1103–1106, doi:10.1130/G33390.1.

Ringwood, A.E., 1961, Chemical and genetic relationships among meteorites: Geochimica et Cosmochimica Acta, v. 24, p. 159–197.

Russell S S, Zolensky M E, Righter K, Folco L, Jones R, Connolly H C Jr, Grady M M, and Grossman J N, 2005, The Meteoritical Bulletin, No. 89, 2005 September: Meteoritics & Planetary Science, v. 40 (Suppl., p. A201–A263.

Sharp, Z.D., 1990, A laser-based microanalytical method for the in situ determination of oxygen isotope ratios of silicates and oxides: Geochimica et Cosmochimica Acta, v. 54, p. 1353–1357, doi:10.1016/0016-7037(90)90160-M.

Tomeoka, K., Kojima, H., and Yanai, K., 1989, Yamato-86720: A CM carbonaceous chondrite having experienced extensive aqueous alteration and thermal metamorphism: Proceedings in NIPR symposium. Antarctic Meteorites, v. 2, p. 55–74.

Velbel, M.A., 2009, Dissolution of olivine during natural weathering: Geochimica et Cosmochimica Acta, v. 73, p. 6098–6113, doi:10.1016/j.gca.2009.07.024.

Velbel, M.A., Tonui, E.K., and Zolensky, M.E., 2012, Replacement of olivine by serpentine in the carbonaceous chondrite Nogoya (CM2): Geochimica et Cosmochimica Acta, v. 87, p. 117–135, doi:10.1016/j.gca.2012.03.016.

Velbel, M.A., 2007, Chapter 4 Surface Textures and Dissolution Processes of Heavy Minerals in the Sedimentary Cycle: Examples from Pyroxenes and Amphiboles: Developments in Sedimentology, v. 58, p. 113–150, doi:10.1016/S0070-4571(07)58004-0.

Wasson, J.T., 1985, Meteorites: Their records of early solar system history: 267 p.

Weiss, B.P., and Elkins-Tanton, L.T., 2013, Differentiated planetesimals and the parent bodies of chondrites: Annual Review of Earth and Planetary Sciences, v. 41, p. 529–560.

Wood Jr., J.A., 1958, Silicate meteorite structures and the origin of the meteorites: Virginia Polytechnic Institute, 166 p.

Zolensky, M.E., Barrett R., and Browning, L., 1993, Mineralogy and composition of matrix and chondrule rims of carbonaceous chondrites: Geochimica et Cosmochimica Acta, v. 57, p. 3123–3148.